PHASE-FIELD MODELING OF THE EVOLUTION KINETICS OF POROUS METALS DURING DEALLOYING

LI JIE

PhD

The Hong Kong Polytechnic University

2021

The Hong Kong Polytechnic University

Department of Mechanical Engineering

Phase-field Modeling of the Evolution Kinetics of Porous Metals During Dealloying

Li Jie

A thesis submitted in partial fulfillment of the requirements for the degree of Doctor of Philosophy

July 2021

CERTIFICATE OF ORIGINALITY

I hereby declare that this thesis is my own work and that, to the best of my knowledge and belief, it reproduces no material previously published or written, nor material that has been accepted for the award of any other degree or diploma, except where due acknowledgement has been made in the text.

_____ (Signed)

Li Jie _____ (Name of Student)

ABSTRACT

Dealloying is the selective dissolution of one or more active elemental components of an alloy in corrosive solutions. It was initially studied as a key failure mechanism for engineering structures. Recently, it was found that dealloying can be used to create porous metals with pore sizes ranging from a few nanometers to a few tens of micrometers. This has attracted significant attention for applications in catalysis, supercapacitors, sensing and actuation, mass and heat transport, and battery electrodes. Therefore, it is essential to understand this process to prevent material failure and develop various porous metal structures. This work focuses on developing a comprehensive numerical model using a phase-field formulation for evolving nanoporous metal structures during corrosive dealloying.

Firstly, a multi-phase-field model of chemical dealloying kinetics in binary alloys is developed to study the topology shape change of porous structures in one-dimension (1-D), two-dimension (2-D) and three-dimension (3-D). By introducing three phase-field variables to represent the phase constitution at the solid-liquid interfaces, the free energy of the precursor-porous clusters-electrolyte system is expressed as a function of field variables and their gradients. The thermodynamic driving force is treated as a function of the difference between the generalized and equilibrium chemical potentials at the interfaces. We propose that the dissolution of the less noble (LN) element leads to interface instability and triggers the nucleation and growth of porous clusters, which are essential for evolving porous structures. The dealloying velocity and porous structure morphology of the model show good overall agreement with experimental

results by calibrating the activation energy of dissolution with the dealloying velocity. Moreover, the roles of some controllable dealloying parameters, including the chemical acid concentration, initial alloy composition, parting limit, and surface diffusion coefficient, are elaborated.

Secondly, a new comprehensive multi-phase-field (MPF) model is proposed to study topological porous patterns formed by spontaneously etching a bulk binary alloy that involves electrochemical reactions, bulk and surface diffusion, ion transport, applied electrode potential, and charge conservation. The governing equations for the alloy-porous cluster-electrolyte system account for a generalized Butler-Volmer electrochemical reaction and are in accordance with the classical nucleation theory. Based on a quantitative examination of the effects of electrode potential and precursor composition, the simulation results reproduce typical phenomena including passive surface dealloying, active porosity evolution, critical potential, and characteristic length scale in 2-D and 3-D.

Finally, the multi-phase-field model is extended to simulate the corrosive dealloying process of alloys with complex structures. Precursors with various phase constitutions and compositions are designed and applied with different activation energies associated with intrinsic electrochemical properties. Several examples are presented to simulate the formation of novel porous structures with unimodal pores by investigating the effect of defect and reinforcement phases in the precursor. The model can also simulate the dealloying of a dual-phase binary alloy comprising a solid solution and intermetallics, or two types of intermetallics and the formation of a nested porous network.

LIST OF PUBLICATIONS

Journal

1) **J. Li**, S. Hu, Y. Li, and S.-Q. Shi, " Evolution mechanisms and kinetics of porous structures during chemical dealloying of binary alloys," Microporous Mesoporous Mater npj Computational Materials, 320 (2021) 111092. https://doi.org/10.1016/j.micromeso.2021.111092

Conference Proceedings

1) **J. Li**, and S.-Q. Shi, "Phase-field modeling of the evolution kinetics of porous structure during dealloying of binary alloys," in TMS 2021 Annual Meeting, March 15-18, 2021, Orlando, Florida, USA.

ACKNOWLEDGEMENTS

Most importantly, I want to thank my supervisor, Professor S. Q. Shi, for his guidance and mentorship throughout my Ph.D. study and research at The Hong Kong Polytechnic University. He has helped me grow immensely as a researcher, speaker, and writer. His timely academic advice and meticulous scrutiny have helped me greatly in accomplishing this work. Furthermore, his patience, motivation, and immense knowledge have taught me to gain a solid theoretical foundation and rigorous research attitude and precisely express myself and my research, which will help me achieve further excellence in future academic or other fields. I could not have imagined having a better advisor and mentor for my Ph.D. study.

My sincere thanks also go to Dr. S. Y. Hu and Dr. Y. L. Li, from Pacific Northwest National Laboratory, USA, for all their help and advice during my Ph.D. research. Furthermore, I want to give special thanks to The Hong Kong Polytechnic University for offering the required resources and all the technical and financial support to conduct my research. My Ph.D. study at The Hong Kong Polytechnic University offered me an excellent and unforgettable experience. Furthermore, I want to express my gratitude to all my other colleagues in Prof. Shi's group: Dr. Lin Chen, Dr. Zhu Jiaming, Dr. Ansari Talha Qasim, and Dr. Xiong Jie, who offered necessary suggestions or encouragement, even though they were not directly involved in this research.

Last but not least, I am thankful for my parents and brother, who have been a source of encouragement throughout my entire education.

TABLE OF CONTENTS

LIST OF FIGURES

LIST OF TABLES

Chapter 1

INTRODUCTION

1.1 BACKGROUND

Nanoporous metals (NPMs) are bulk samples with a network structure where bicontinuous solid ligaments and complementary pores interpenetrate at the nanoscale. These metals exhibit metallic features, such as high strength, heat and electrical conductivity, and optimized and functionalized properties entailed by their porous structure, which have attracted attention from the scientific community and industry. Evidence has shown an increasingly wide range of applications of NPMs. The prospect of NPMs in actuators rests on their superior mechanical properties, which are easily tuned and accessible to electrical signals [1]–[3]. Another typical application branch is catalysis, where the extraordinary activity of NPMs enables them to function as effective catalysts in hydrogen fuel cells and exhaust treatment [4]–[7]. As novel functional materials, NPMs are especially attractive for use as high-performance sensors and electrodes due to their optimized sensitivity, charge storage, and ion diffusion provided by their hierarchical porosity [3], [8]–[10].

The desire to use porous metallic materials in versatile applications requires developing fabrication methods. Primary techniques include sintering, additive manufacturing, templates, and dealloying, which are commonly used to synthesize various porous structures [8]. Among these methods, dealloying is the only viable approach to realizing nanometer to micron-sized

pores and diverse porous samples, including film, rod, and ribbon, which are sufficient for specific industrial applications. Dealloying is a common process in which one or more metal elements are selectively removed from a precursor based on the physical or chemical differences between metal elements, leaving a porous residue. In the context of corrosion, it has been well known as a materials failure mode to be avoided. The most common example is the dezincification of brass used in seawater condenser tubes [11], [12]. With the advent of focus on porous materials, dealloying has become a platform for materials processing to fabricate porous materials with pore sizes ranging from nanometers and micrometers.

The dealloying technique can be divided into corrosion-controlled dealloying method and physical controlled dealloying method. The most common method in industrial applications is the chemical dealloying technique that involves the free corrosion of alloy components in aqueous acid or alkaline used to fabricate porous Au, Cu, Pt, and other metal structure networks [4], [13]–[15]. Electrochemical dealloying utilizes the standard electrode potential difference between metal elements to selectively dissolve the LN element from the parent alloy in a corrosion environment with applied electrode potential. Physical method includes vapor dealloying and liquid metal dealloying, which are new and environmentally friendly approaches to fabricate nanoporous materials by utilizing the vapor pressure or melting point difference between constituent elements in an alloy [16]–[20].

Well-designed experiments could characterize the microstructure and properties and investigate the controllable parameters affecting the dealloying velocity, morphology, and composition of the dealloyed samples. During the last two decades, significant experimental findings on the key dealloying mechanisms are, in contrast to the mechanical and functional properties, limited [4], [8], [21]–[24]. Furthermore, minimal information is available on theoretical modeling and computational research, which could explain the underlying physical mechanisms and clarify some controversial phenomena. For example, direct observation of the development of random and porous patterns is not possible with current experimental technology, especially during the early stages of dealloying. Researchers once used the kinetic Monte Carlo model [25] to reproduce many characteristics of dealloying, especially the pore formation. However, it has some weaknesses (this work will be discussed later). Conventionally, the critical potential marks the onset of continuous porosity evolution. However, the experimentally determined value has a large range due to different sweep rates in electrochemical experiments and the blurry transition zone of the polarization curve. Content threshold defines the ratio of the more noble (MN) element in precursor alloy, above which, a passivation layer composed of the MN element will form at the alloy-electrolyte interface. However, there has been no microscopic evidence in the experiments. Computer simulation can provide a viable method to investigate what occurs at the propagating dealloying front and determine the original porous patterns.

Additionally, some theoretical studies assume an idealized porous geometry, whereas the simulations could create a more realistic asymmetric and stochastic porous structure.

Two key issues must be addressed. The thermodynamics of the dealloying determines whether porous structure evolution occurs in a dealloying system; this specifically involves determining the critical potential, parting limit, and other dealloying parameters. The kinetics of the dealloying determines how the topological solid-liquid interface and porous structures form and how fast the porous structure evolves, which are dependent on extensive system parameters, such as the precursor composition, electropotential, and electrolyte composition. This work aimed to develop a comprehensive theoretical framework for the microstructure evolution of self-organized nanoporous structures during the dealloying process using the phase-field (PF) method. Although the PF model has been extended to address multiple components or phases, limited progress has been achieved on models addressing the details of the solid-electrolyte interface and incorporating the electrochemical effects. The multi-phase-field (MPF) formulations, described in detail throughout the rest of this work, are perhaps the best available tool for understanding the complexity of solid-electrolyte interfaces. The developed MPF models can capture fundamental kinetic processes and examine the effects of extrinsic and intrinsic factors. The work creates opportunities for various interesting kinetic studies on phase transitions and the morphology evolution of other electrochemical processes.

1.2 RESEARCH OBJECTIVES

The primary goal of this work was to develop a comprehensive theoretical and computational framework for the corrosion dealloying process that considers the surface diffusion, interface charge transfer, chemical and electrochemical reactions at the interfaces, mass and ion transport in the alloy and electrolyte, and precursor and electrolyte compositions. We began with simple and well-studied cases such as silver-gold (Ag-Au binary alloys and progressed to more complex systems. At each step, we verified our models against experimental data in the literature.

The specific objectives were as follows:

1. Develop a MPF model for the chemical dealloying of a model binary alloy (such as Ag-Au) in an acid electrolyte (such as HNO_3) in one-, two-, and three-dimensional geometries to reproduce the evolution of complex interface patterns. This model was also developed to reveal the underlying physical mechanism and investigate the effect of alloy composition, bulk and surface diffusion, and electrolyte composition.

2. Develop a MPF model for porous evolution in Ag-Au during electrochemical dealloying to investigate the effect of applied potential and determine the critical potential. The model accounts for the Butler-Volmer electrochemical kinetics and the nucleation-growth mechanism.

3. Apply the proposed MPF models to simulate the formation of various porous patterns based on alloys with complex structures and generate new insight into the design of porous structures with specific compositions and pore sizes. Understanding morphological

evolution during the dealloying of multi-phase and multicomponent systems is important for industrial applications and interesting from an academic perspective.

1.3 THESIS OUTLINE

The remainder of the thesis is organized as follows:

1. Chapter 2 encapsulates a comprehensive literature review on dealloying mechanisms, multiscale modeling techniques, and PF methods.
2. Chapter 3 derives a MPF model for a three-phase (alloy-porous clusters-electrolyte) system to reproduce the porous evolution during chemical dealloying. This chapter details the dealloying kinetics and examines the roles of alloy composition, electrolyte content, surface diffusion, and dimensionality. The model is one of the first to simulate multidimensional topological porous geometries generated by chemical dealloying.
3. Chapter 4 presents the development of a MPF model that can explicitly capture the key physical process in the presence of an externally applied potential. This model probes the current-potential behavior and dealloying critical potential. This chapter is the first report of a PF simulation that correctly captures the electrochemical and physical processes governing the phase transformation from metallic solid to porous metals and electrolyte.
4. Chapter 5 is dedicated to extending the MPF models to simulate and predict various porous patterns formed from the dealloying process of alloys with complex structures.

The MPF model is ideally suited to modeling the dealloying of alloys with complex structures. Simulations of the dealloying of precursors with different phases and components are presented to illustrate how the model could improve understanding and predict the formation of porous metals with multimodal pore sizes and hierarchical structures.

5. Chapter 6 contains concluding remarks and future recommendations and is followed by appendices, nomenclature, and references.

Chapter 2

LITERATURE REVIEW

2.1 DEALLOYING MECHANISMS

Dealloying is a complex phenomenon requiring multidisciplinary knowledge, especially of thermodynamics, electrochemistry, surface science, and solid mechanics. It is generally recognized that some conditions must be satisfied for selective dissolution of alloy to occur. First, a sufficient voltage difference of the metal electrode-electrolyte equilibrium potential is required between the alloying elements. For example, the electrochemical potential differences for Ag-Au and Mg-Cu alloys are 0.8 and 1.4 V, respectively. Secondly, dealloying occurs only when the initial content of the LN element in the precursor exceeds a threshold value, or parting limit, ranging from 40% to 60% of the parent alloy. Thirdly, the mass transport occurring at the metal-electrolyte surface is several orders of magnitude faster than in the metal-vacuum surface [26]–[29]. An important and controversial issue regarding dealloying is the theoretical fundamentals of how the alloy etching is maintained and the topological porous microstructure evolves during dealloying. The following is a review of possible mechanisms proposed to explain the porosity evolution.

The dissolution-redeposition mechanism was first proposed to explain the dezincification of brass. It was assumed that MN and LN elements dissolve simultaneously at the alloy-liquid interface. LN atoms convert into ions, flowing into solution. MN then atoms precipitate near

the interface and redeposit in the base alloy via a film or the saturation of ions in solution. Although the curvature effects allow leaching of the MN element when the applied electropotential is lower than the equilibrium electrode potential, this mechanism cannot explain the scenario where the MN element cannot be dissolved at an electrode potential far below its dissolution potential.

Pickering et al. [30] determined that the ionization of the LN element and reorganization of the MN element are driven by volume diffusion. The dissolution of LN atoms located at the original sites creates surface vacancies and divacancies. The injection of these into the bulk precursor allows the interior metal atoms to move toward the interface by vacancy diffusion. The new LN atoms are dissolved, leading to a continuous increase in surface geometric instability. However, this model made some extreme assumptions. The molar fractions of vacancies and divacancies are larger than the equilibrium concentrations of those in real metals. Additionally, the volume diffusion rate at room temperature is not yet sufficiently fast to achieve the dealloying current density observed in the experiments.

Forty et al. [31] did not consider the effect of volume diffusion. They proposed a surface diffusion model, which explained how the interface atoms undergo a transition from a disordered state caused by the ionization of LN elements to an ordered state due to the surface diffusion of MN elements. The solvation and enhanced diffusion of MN elements at the surface account for the aggregation of these atoms into islands via a nucleation process occurring at some preferable sites. These islands then grow further via the continuous release and diffusion

of MN atoms, creating channels surrounded by islands and allowing further exposure and dissolution of LN atoms uncovered by these islands. Although this model successfully explained the aggregation of MN atoms, it predicted the gradual shrinkage of channels, which is inconsistent with the sustainable increase in current density and pore size during the late stage of dealloying shown in experimental results.

Sieradzki et al. [32]–[34] presented a percolation model to explain the macroscopic critical electropotential phenomenon. They found that the curvature-dependent surface process dominates surface morphology, and surface geometric instability results from the competition between the surface-roughening process driven by the dissolution of the LN atoms and the surface-smoothing process driven by the surface diffusion of MN elements. The model provided an expression of critical potential to mark the transition from alloy passivity (planar stability) to rapid dealloying (porosity formation), suggesting that inherent percolation clusters comprising LN elements determine the surface morphology. The alloy content defines the threshold potential, above which sustainable porous evolution is maintained; otherwise, the surface diffusion of the MN element dominates the interface process, leading to surface passivation and extinction of the dealloying process. However, channel diameters in NPMs are wider than the average spacing between atoms in the original alloy. Furthermore, this model cannot clearly explain the topological porous structure evolution.

Jonah Erlebacher et al. [13], [25], [35], [36] proposed a phase separation working model in which the decisive physical and chemical processes are limited in the solid-liquid interface. The

aggregation into clusters of MN atoms is a phase separation or spinodal decomposition process based on the released MN atoms and electrolyte as a two-component solution. Fig. 2.1 illustrates the kinetic working model. LN atoms are first removed from low-coordination sites, as shown in Fig. 2.1(a). Released Au atoms tend to transport into high-coordination sites by interfacial uphill diffusion (associated with spinodal decomposition) rather than be left as thermodynamically unfavorable adatoms. More parent alloys are then attacked by the electrolyte, and more Au atoms diffuse into these protruding ligaments. If the diffusion distance is too far for MN atoms to passivate the bases of ligaments, these growing ligaments are undercut. The growth and undercut process bifurcates the pores, creating the initial porous structure comprising surface-passivated Au-rich clusters trapping original alloy, as shown in Fig. 2.1(e). Finally, coarsening of these intertwined ligaments leads to the expansion of pores, shown in Fig. 2.1(f).

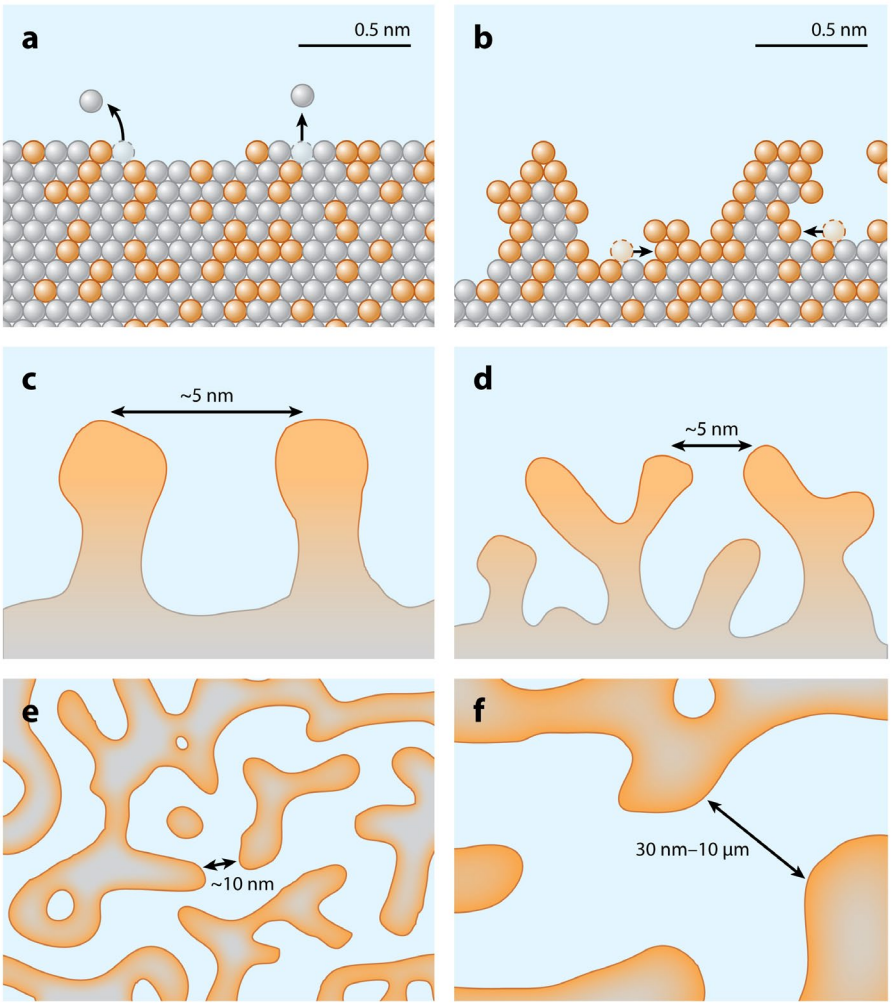

Figure 2.1 Phase separation working model for the chemical dealloying of Ag-Au alloy system (Ag, gray; Au, orange). (a) Dissolution of Ag; (b) aggregation of Au clusters; (c,d) growth and undercutting of ligaments; (e) initial porous structure; (f) coarsening of ligaments [4].

It should be noted that all the above-mentioned models aimed to explain the interface evolution occurring at the dealloying front. However, dealloying comprises two successive processes, a primary dealloying process where the LN elements are selectively dissolved from the bulk precursor, and a secondary dealloying process where the LN elements are dissolved from dealloyed ligaments. The secondary dealloying process defines the morphology and

composition of the NPMs, which are critical to the catalytic, optical, and mechanical properties of NPMs. However, the specific mechanism is unclear. Moreover, the interplay of physical, electrical, and chemical parameters in the alloy etching and self-organized nucleation and growth of nanostructures remain largely unexplained. No comprehensive theoretical and computational model is available in the literature that provides satisfactory, quantitative, and experimental predictions.

2.2 MULTISCALE MODELING METHODS

Theoretical modeling of the structural evolution of metals is classified into three levels in terms of the length scale: macroscale theories predicting the behavior of systems over millimeter or larger lengths—a scale inapplicable to pore formation and evolution during dealloying; mesoscale models predicting the evolution of local microstructures on a length scale from submicrometer to millimeter; and atomistic models that track interactions and motion of individual atoms or study the energy and mechanisms of bonding and charge transfer at the interfaces.

To the best of our knowledge, most theoretical modeling studies on porous metals to date are at the atomistic scale, or at best, at the lower bound of the mesoscale (~100 nm). The kinetic Monte Carlo (KMC) method has been employed to simulate random microstructure evolution during dealloying. It is an effective tool to reproduce pore formation directly, and the parting limit, critical potential, and current-potential behavior are similar to those obtained from

experimental observation [25], [36]–[39]. However, KMC simulations have several weaknesses: (1) the agreement of KMC with experiments depends heavily on knowledge of specific phenomenological parameters in the probability density function, which are often unavailable; (2) some essential rate-limiting physical processes, such as ion diffusion in the etching solution and the systematic investigation of environmental and material factors, are not considered in KMC simulations; and (3) the largest size of metals that KMC can handle is in the order of 100 nm, which is still small when studying the porous coarsening kinetics at the micron or even larger length scales. Due to the limits of spatial and temporal scales, molecular dynamics (MD) studies of porous metals often focused on investigations of mechanical properties (surface stress and deformation [40], [41]; thermal performance [42]; and magnetic properties [43]). The classical simulation technique, finite element modeling (FEM), is also a powerful tool to estimate and understand stress-strain behavior, cracking propagation, and other mechanical properties [44], [45]. Although MD, FEM, and their combination can accurately predict the physical and chemical properties of porous metals, these methods cannot handle the complex evolution of the metal-solution interface during the preparation. Additionally, real spatial and temporal scales of massive dealloying and coarsening cannot be reflected. The level set method assumes a sharp interface [46], [47], requiring the interface dynamics to be understood *a priori*, making it difficult to extend to complex systems with multiple components.

2.3 PHASE-FIELD METHOD

Phase transformations, chemical reactions, and microstructure evolution are thermodynamically driven by the free energy minimization of the system. The PF method fully uses thermodynamic and kinetic principles, deriving governing equations coupled with the relevant transport equations of the system to predict its microstructure evolution. It describes the microstructures of a system (including compositional and structural domains) using a set of conserved and non-conserved field variables that are continuous across the interfacial regions (i.e., a diffusive rather than a sharp interface). The temporal evolutions of the conserved and non-conserved field variables are governed by the Cahn-Hilliard diffusion and Allen-Cahn relaxation equations, which underlie the basic physics of microstructure evolution. The PF method can predict the evolution of arbitrary morphologies and complex microstructures without explicitly tracking the positions of interfaces using fundamental thermodynamic and kinetic information as the input. The PF method has rapidly advanced as a mesoscale modeling method over the last two decades. It has been used to predict many material processes, such as solidification, dendrite evolution, solute diffusion and segregation, phase transformation, electrochemical deposition, dislocation dynamics, crack propagation, and void evolution in materials [48]–[51]. Surprisingly minimal progress has been made on the mesoscale modeling of metal porosity kinetics in aqueous solutions during dealloying using the PF method.

It is generally recognized that dealloying-produced bicontinuous nanoporous structures are similar to spinodal decomposed two-phase structures. Therefore, the PF method was commonly used to create nanoporous microstructures for simulation studies on the geometric relaxation

and mechanical properties of NPMs [52], [53]. Erlebacher [25] applied the Cahn-Hilliard equation to describe the diffusion of gold in an Ag-Au alloy during dealloying but provided few concrete modeling results for porosity development. Instead, the results of porous morphology evolution from KMC simulations are presented. It is unclear whether the numerical solution of the Cahn-Hilliard equation in this work was one-dimensional. Geslin et al. [20] used a ternary alloy solidification PF model to predict the nanoporous structure evolution during the liquid metal dealloying of Ti-Ta alloy from a Cu melt. By comparing with the experimental results, they demonstrated that pattern formation is driven by the interplay of interfacial spinodal decomposition and diffusion-coupled growth. However, no PF model for the corrosion-controlled dealloying process is available due to the difficulty in capturing the corrosion reaction kinetics at the metal-electrolyte interface.

Mai et al. [54] first studied the pitting corrosion of metal using the Kim-Kim-Suzuki (KKS) model and reproduced the activation- and diffusion-controlled corrosion kinetics. Based on this model, Ansari et al. [55] further considered the chemical reactions, transport of ions, and distribution of the electric potential in the electrolyte during the pitting corrosion. Chen et al. [56] developed a nonlinear PF model for the dendritic growth during the Li-electrodeposition process, which accounts for the Butler-Volmer nonlinear electrochemical kinetics. Later, this model was extended and used to study and predict the metal corrosion process. For example, Lin et al. [57], [58] simulated the pitting corrosion in a stressed metal by incorporating the effect of mechano-electrochemical coupling and insoluble deposition. Ansari et al. [59], [60]

proposed a MPF model to describe the effect of insoluble corrosion products and intergranular corrosion kinetics. All these models assumed the dissolution of a pure metal (the nature of the metal was not specified) from an existing pit without considering the effect of the noble component in the metal. However, many experimental studies have demonstrated that the noble component in the metal could affect the corrosion morphology and kinetics of metals.

Chapter 3

MPF MODEL OF EVOLUTION KINETICS OF POROUS STRUCTURES DURING CHEMICAL DEALLOYING

3.1 INTRODUCTION

Porous metals made from the chemical dealloying method account for more than 80% of products synthesized by all dealloying methods [17]. It is easy to operate, and no cost and complex equipment is required, which is suitable for mass and low-cost production. Thus, understanding the underlying pattern formation mechanisms during chemical dealloying and developing a comprehensive theoretical framework that can quantitatively predict the morphology of porous evolution is very important for better control and design of porous structures.

Mai et al. [54] employed the KKS model to simulate the pitting corrosion of metals and calibrated the kinetic mobility with the exchange current density in experiments. This is the first model that successfully reproduces the 2-D corrosion phenomena. In this model, an order parameter was introduced to describe the physical state of local phase. The local material point is evaluated as the weighted sum of the solid and liquid phases with different compositions and equal chemical potentials. The deviation of local concentration from the equilibrium concentration accounts for the driving force of the movement of the corrosion front. On this basis, we first assume the equilibrium state of the dealloying system, and the interface corrosion

of LN element drives the system to evolve towards the equilibrium state. However, the model for pitting corrosion can only capture the evolution of a pairwise metal-liquid interface and not handle the formation of a new phase and evolutions of other pairwise interfaces. Hence, we need to develop a MPF model to deal with the complex multiphase problem of dealloying system. Researchers once proposed that the released MN elements aggregate via a spinodal decomposition process after the LN atoms are dissolved. It can not explain the dealloying of intermetallic compounds, where the nucleation of new crystallites is required. According to the classical nucleation theory, we adapt a noise term to generate spontaneous heterogeneous nucleation of porous clusters at the alloy-electrolyte interface.

In this study, we develop a thermodynamically consistent theoretical and computational MPF model to investigate the chemical dealloying behavior of Au–Ag alloy. The remainder of this paper is organized as follows. In the methods section, the formulation of a MPF model for the alloy–Au clusters–electrolyte system is detailed. The system's Gibbs free energy comprises the chemical and interfacial free energy. The generalized Allen–Cahn equations and modified Cahn–Hilliard equations are constructed to govern the topological interface and metal concentration evolutions. In the results section, the fundamental dealloying behavior and evolution mechanism are analyzed based on 1-D, 2-D, and 3-D simulation cases. Next, simulations are conducted for a set of samples with different dealloying conditions to shed light on the morphological differences dependent on the corrosion agent, initial alloy composition, dimensionality, surface diffusion coefficients and also compared with the experimental results.

3.2 METHOD

3.2.1 Investigated system

The model system we studied here consists of $Ag_{1-c_0}Au_{c_0}$ binary alloy immersed in nitric acid solutions shown in Fig. 3.1. The etching of alloy starts from the free corrosion of Ag via the following reaction [61]:

$$Ag + 2HNO_3 \rightarrow AgNO_3 + NO_2 + H_2O, \tag{3.1}$$

The corrosion rate is governed by the Arrhenius Law:

$$R_1 = k_0 c_{Ag} \exp\left(\frac{-G}{RT}\right) \tag{3.2}$$

Here, k_0 is the reaction constant, c_{Ag} is the molar fraction of silver, R is the gas constant, T is the absolute temperature, and G is the reaction activation energy dependent on the acid concentration in the electrolyte phase and initial composition of the alloy. Then undissolved Au atoms do not reside in original sites but aggregate into nanoscale clusters in the solid–liquid interface. In addition to bulk diffusion and two interface processes described above, an overall chemical dealloying process also involves long–range mass transport processes (inflow of corrosive electrolyte into the porous structure and outflow of dissolved ions through the electrolyte). Many experimental studies, based on a constant current response measured when an electrical potential is applied, have testified that the dealloying velocity is approximately constant, indicating that long–range mass transport processes are very fast, and thus, do not

control the porous structure evolution during the chemical dealloying of Ag-Au [21], [44], [62]. Therefore, in this study, we assume that the formation and evolution of a porous structure are dominated by the two interface processes, and that the long-range mass-transport processes can be ignored.

To test the agreement between the experimental observations and simulation results, we choose a set of alloys with different initial Au compositions (c_0 = 0.2, 0.25, 0.3, and 0.35) for the numerical tests. The nitric acid solutions are set with four different concentrations (c_a = 9.1, 10.9, 12.7, and 14.6 mol/L). We assign the value obtained from reference [63] to the reaction activation barrier (G) in the dealloying process of $Ag_{0.7}Au_{0.3}$ alloy immersed in nitric acid solution with a concentration of c_a = 10.9 mol/L and calibrate the reaction constant k_0 by approximating the simulated dealloying velocity to the experimental value [44]

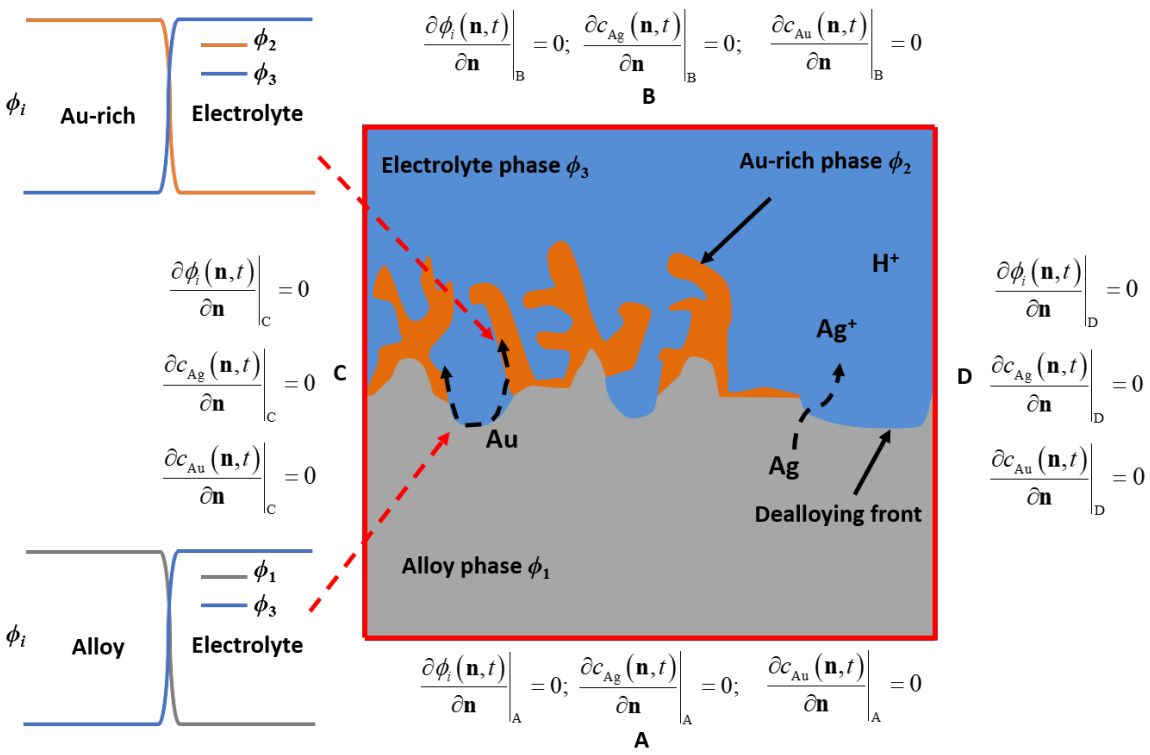

Figure 3.1 Schematics of the chemical dealloying process of Ag–Au alloy and boundary conditions

The results obtained from the extensive body of experiments show that the solid-liquid interface comprises passivated porous clusters linked by pits, where the alloy is attacked by the electrolyte. In the Au–Ag system, the aggregation of Au clusters is essential for the topological interface morphology. Erlebacher et al. presented an interfacial spinodal decomposition mechanism to explain the coalescence of Au clusters [25]. In this mechanism, Ag is dissolved from the solid-liquid interface due to the corrosion process, while the undissolved Au atoms are released into the interface layer. The Au atoms and electrolyte in this interface layer are considered as two conserved variables in a regular solution. As the concentration of Au in this interface layer is much above its solubility in the electrolyte, Au clusters are formed within the

spinodal decomposition region. There is, however, another possible mechanism, Au cluster nucleation, and growth, where the interface layer lies in the metastable region. The aggregation of nearly pure Au clusters is a thermally activated process, which means that the nucleation of Au clusters in the interface layer requires overcoming an energy barrier.

3.2.2 Multi-phase-field model

Based on this Au nucleation and growth mechanism, we use three order parameters ϕ_i (i = 1, 2, 3) and two concentration parameters (c_{Ag} and c_{Au}) to describe the microstructures in the system with three coexisting phases at the interface: Ag–Au alloy phase (ϕ_1, c_{Ag}, c_{Au}), Au-rich phase (ϕ_2, c_{Ag}, c_{Au}), and electrolyte phase (ϕ_3, c_{Ag}, c_{Au}). Note that $c_{Ag} \approx 0$ in the Au-rich phase and $c_{Au} \approx 0$ in the electrolyte phase. ϕ_i is used to spatially differentiate the three coexisting phases and satisfy the normalization condition of $\sum_{i=1}^{3} \phi_i = 1$. Within the individual phases, ϕ_i has a constant value of 1 inside phase i and 0 outside phase i, and smoothly varies from 1 to 0 across the phase interface.

PF method describes the microstructure evolution of heterogeneous materials toward the reduction in the thermodynamic energy functional of the system, which comprises free energy of the bulk phases and interfaces. Here, to avoid an unexpected formation of the third phase (the electrolyte) in a pairwise interface, following reference [64], the total free-energy functional of the system is expressed as

$$F = \int \left(\frac{\varepsilon}{2} \sum_i \left(\nabla \phi_i \right)^2 + W \sum_i \phi_i^2 \left(1 - \phi_i \right)^2 + f_{\text{chem}} \left(\phi_i, c_{\text{Ag}}, c_{\text{Au}} \right) \right) dV , \tag{3.3}$$

where the first term corresponds to the gradient energy density at the interfaces, the second term indicates the potential barrier between the bulk phases, and the last term describes their chemical free-energy density. Furthermore, the gradient energy coefficient, ε, and potential well height, W, are defined as $\varepsilon = \frac{\sigma l}{4\sqrt{2}a}$ and $W = \frac{a\sqrt{2}}{4}\sigma / l$, where a is a numerical constant, l is the interface thickness, and σ is the interface energy [54]. We assume the same interface property for different interfaces in the system. Although we aim to match the experimental observations as much as possible, we also aim to develop a model for the general behavior of interface topology evolution of porous structures using the minimum number of parameters to elucidate the essential processes during the dealloying.

As shown in Eq. (3.4), the chemical free energy is developed using a mixture rule, which assumes that the interfacial region is occupied by a mixture of three phases, with the fraction of h_i for the i phase. The interpolation function h_i can be formulated as $h_i = \phi_i^2 \big/ \sum_j \phi_j^{\,2}$ to fulfill the thermodynamic consistency requirement, which meets $\sum_j h_j = 1$ and $dh_j / d\phi_i = 0 (\phi_i = 0,1)$. We define the free-energy density of phase i, f_{chem}^i, as a parabolic form in terms of c_{Ag}^i and c_{Au}^i, which are the compositions of Ag and Au in ϕi using Eq. (3.5). c_{Ag}^i and c_{Au}^i are not independent of each other, but constrained by the conditions of Eqs. (3.6) and (3.7). These conditions enforce that the interfacial region be composed of coexisting phases with different compositions but equal chemical potential for all components. $c_{\text{Ag,e}}^i$ and $c_{\text{Au,e}}^i$ are the normalized equilibrium concentrations of Ag and Au elements for the three phases

shown in Table 3-1, and c_0 is the initial alloy composition of the alloy phase (alloy precursor). Note that the initial alloy can be considered to be in a quasi-equilibrium state, although the values of the equilibrium concentrations in the alloy phase used in the simulations are different from the concentrations corresponding to the minimum values of free energy. *A* and *B* in Eq. (3.5) are the thermodynamic factors, which are assumed to be equal for the three phases, for simplicity. Because the parabolic form of chemical free-energy density in Eq. (3.5) is an approximation of the real chemical free-energy functional, we suggest to select the thermodynamic factors based on the nucleation energy of the porous Au-rich phase.

$$f_{\text{chem}} = \sum_{i=1}^{3} h_i f_{\text{chem}}^{i}(c_{\text{Ag}}^{i}, c_{\text{Au}}^{i}) \tag{3.4}$$

$$f_{\text{chem}}^{i} = A\left(c_{\text{Ag}}^{i} - c_{\text{Ag,e}}^{i}\right)^2 + B\left(c_{\text{Au}}^{i} - c_{\text{Au,e}}^{i}\right)^2 \tag{3.5}$$

$$c_{\text{Ag}} = \sum_{i=1}^{3} h_i c_{\text{Ag}}^{i}, \frac{\partial f_{\text{chem}}^{1}}{\partial c_{\text{Ag}}^{1}} = \frac{\partial f_{\text{chem}}^{2}}{\partial c_{\text{Ag}}^{2}} = \frac{\partial f_{\text{chem}}^{3}}{\partial c_{\text{Ag}}^{3}} = \mu_{\text{Ag}} \tag{3.6}$$

$$c_{\text{Au}} = \sum_{i=1}^{3} h_i c_{\text{Au}}^{i}, \frac{\partial f_{\text{chem}}^{1}}{\partial c_{\text{Au}}^{1}} = \frac{\partial f_{\text{chem}}^{2}}{\partial c_{\text{Au}}^{2}} = \frac{\partial f_{\text{chem}}^{3}}{\partial c_{\text{Au}}^{3}} = \mu_{\text{Au}} \tag{3.7}$$

$$\frac{\partial \phi_i}{\partial t} = -\frac{1}{3}\sum_{j \neq i} L\left(\frac{\delta F}{\delta \phi_i} - \frac{\delta F}{\delta \phi_j}\right) + \xi_{\phi_2} \tag{3.8}$$

$$\frac{\delta F}{\delta \phi_i} = -\frac{\varepsilon}{2}\nabla^2 \phi_i + W\phi_i\left(1-\phi_i\right)\left(1-2\phi_i\right) + \Omega_i \tag{3.9}$$

$$\Omega_i = \sum_j \frac{\partial h_j}{\partial \phi_i}\left(f_{\text{chem}}^{j}\left(c_{\text{Ag}}^{j}, c_{\text{Au}}^{j}\right) - \mu_{\text{Ag}} c_{\text{Ag}}^{j} - \mu_{\text{Au}} c_{\text{Au}}^{j}\right) \tag{3.10}$$

$$\xi_{\phi_2} = \xi_0 r 16 \phi_1^2 \left(1-\phi_1\right)^2 I_0 k_B T \, \Delta\Omega_{23}^2 / \sigma^3 \tag{3.11}$$

Table 3-1 Equilibrium compositions of Ag and Au in three phases

Phases / Components	Alloy phase (ϕ_1)	Au phase (ϕ_2)	Electrolyte phase (ϕ_3)
Ag	1-c_0	0	0
Au	c_0	1	0

Then, the kinetic equations for the spatial and temporal evolutions of ϕ_i can be expressed as Eqs. (3.8) and (3.9), where L indicates the phase-field kinetic mobility and Ω_i indicates the grand potential of phase ϕ_i. In Eq. (3.8), the nucleation of the Au phase at the solid-liquid interface is attributable to the thermal fluctuations in the interfacial layer, which is incorporated into the model through a noise term, ξ_{ϕ_2}, expressed as Eq. (3.11). In this equation, $r \in (-1,1)$ is a random number assigned to the alloy interface in each time and space step, and ξ_0 is the strength of the fluctuations. The heterogeneous nucleation is explicitly incorporated into the system by assuming a nucleation rate that follows $I = I_0 \exp\left(-G^* / \left(k_B T\right)\right) \approx I_0 \, k_B T / G^*$. According to the classical nucleation theory, I_0 is the nucleation prefactor, k_B is the Boltzmann constant, and G^* is the critical nucleation energy, expressed as $G^* = \sigma^3 / \Delta\Omega_{23}^2$. Thus, this term introduces the fluctuations in ϕ_2 at the ϕ_1/ϕ_3 interface with an amplitude that is proportional to the chemical driving force $\Delta\Omega_{23} = \Omega_2 - \Omega_3$ and inversely proportional to the interface energy.

Then, for conserved concentration fields, the governing equations using the modified Cahn–Hilliard equation can be expressed as follows:

$$\frac{\partial c_{\mathrm{Ag}}}{\partial t} = \nabla M_{\mathrm{Ag}} \nabla \frac{\delta F}{\delta c_{\mathrm{Ag}}} + \lambda_1 R_1 = \nabla D_{\mathrm{Ag}} \sum_i h_i \nabla c_{\mathrm{Ag}}^i + \lambda_1 R_1 \tag{3.12}$$

$$\frac{\partial c_{\mathrm{Au}}}{\partial t} = \nabla M_{\mathrm{Au}} \nabla \frac{\delta F}{\delta c_{\mathrm{Au}}} = \nabla D_{\mathrm{Au}} \sum_i h_i \nabla c_{\mathrm{Au}}^i \tag{3.13}$$

$$D_{\mathrm{Ag}} = \sum_{i=1}^{3} h_i D_{\mathrm{Ag}}^i + \lambda_1 D_{\mathrm{Ag}}^{\mathrm{s}}, \quad D_{\mathrm{Au}} = \sum_{i=1}^{3} h_i D_{\mathrm{Au}}^i + \lambda_2 D_{\mathrm{Au}}^{\mathrm{s}} \tag{3.14}$$

The first terms of Eqs. (3.12) and (3.13) describe the diffusion of Ag and Au in the solid. As expressed in Eq. (3.14), the diffusion of all metal atoms involves the bulk diffusion in *i* phase with respective diffusivities of D_{Ag}^i and D_{Au}^i and interface diffusion with diffusivities of $D_{\mathrm{Ag}}^{\mathrm{s}}$ and $D_{\mathrm{Au}}^{\mathrm{s}}$. The last term of Eq. (3.12) represents the corrosion rate of Ag at the metal–electrolyte interface. λ_1 and λ_2 in Eqs. (3.12) and (3.14) are expressed as $\lambda_1 = 4h_1h_3$ and $\lambda_2 = 4(h_1h_3 + h_2h_3)$, indicating that the interface behavior of the LN elements is appreciable only in the vicinity of the alloy–electrolyte interface and that the surface diffusion of MN elements occurs at pairwise interfaces (including alloy–electrolyte and Au–electrolyte interfaces). The diffusion path of the MN element or the binary interfaces involved in this process is described in Fig. 3.1. The values of all parameters used in the simulations are listed in Table 3-2.

3.3 NUMERICAL IMPLEMENTATION

In two dimensions, the system has a size of 90 × 100 nm^2, and the liquid domain is set with an initial depth of 10 nm. The boundary conditions are given in Fig. 3.1. The boundary conditions in 1-D and 3-D cases are the same as those in 2-D cases. The zero-flux boundary conditions are applied on all sides or surfaces of the system. Uniform square-mesh elements are chosen to discretize the space with $\Delta x = l/10$ and $\Delta x = l/4$ for 1-D and 2-D systems (l is the interface thickness), respectively. The size of alloy domain in 3-D geometry is 40 × 30 ×20 nm^3.

Tetrahedral mesh elements are used to discretize 3-D systems by using COMSOL Multiphysics. The Galerkin method is used as the finite element discretization method [65]. The backward differentiation formula is used for the time integration of the governing equations [66].

Table 3-2 Parameters used in chapter 3

	Parameter	Value
Interfacial energy density	σ (J/ m^2)	1
Interface thickness	l (nm)	2
Kinetic interface parameter	L (m^3/J/s)	1.5×10^{-6}
Bulk diffusion coefficient of Ag in the alloy phase	D^1_{Ag} (m^2/s)	10^{-20}
Bulk diffusion coefficient of Au in the alloy phase	D^1_{Au} (m^2/s)	10^{-20}
Bulk diffusion coefficient of Ag in the Au-rich phase	D^2_{Ag} (m^2/s)	10^{-20}

Bulk diffusion coefficient of Au in the Au-rich phase	D^{2}_{Au} (m^2/s)	10^{-20}
Surface diffusion coefficient of Ag	D^{s}_{Ag} (m^2/s)	10^{-16}~ 10^{-13}
Surface diffusion coefficient of Au	D^{s}_{Au} (m^2/s)	10^{-16}~ 10^{-13}
Free-energy density curvature	A (J/m^3)	3×10^9
Free-energy density curvature	B (J/m^3)	15×10^9
Ideal gas constant	R (J/mol/K)	8.314
Absolute temperature	T (K)	300
Numerical constant	a	2.94
Nucleation prefactor	I_0	10^5
Reaction constant	k_0	1.87×10^{19}

3.4 RESULTS AND DISCUSSION

3.4.1 One-dimensional PF model results

A 1-D model is first implemented to simulate the evolution of the planar dealloying frontier shown in Fig. 3.2; in this case, a binary alloy $Ag_{0.7}Au_{0.3}$ immersed in 10.9 mol/L nitric acid is used. After dealloying for 10 s, the dealloying frontier is observed to be occupied by a mixture of three phases. At the dealloying frontier, most of the Ag element is dissolved, while the Au element, as shown in Fig. 3.2(a), is confined to the surface layer, leading to a buildup of Au and the formation of ϕ_2. The gradual accumulation of the Au element, driven by surface diffusion, blocks the corrosion of Ag, leading to a decrease in the Ag dissolution flux and a noticeable retardation of the dealloying front propagation, as shown in Fig. 3.2(b). Therefore, in a 1-D system, the corrosion of Ag is reduced by Au accumulation at the solid-liquid interface. In addition, extracting the peak concentration of the Au element (c_{Au}^{P}) from the interface layer, we find that the dealloying velocity (v) decreases exponentially with c_{Au}^{P}, which is consistent with the 1-D simulation results of the liquid-metal dealloying in reference [20], where the unmelted element accumulated at the solid-liquid interface.

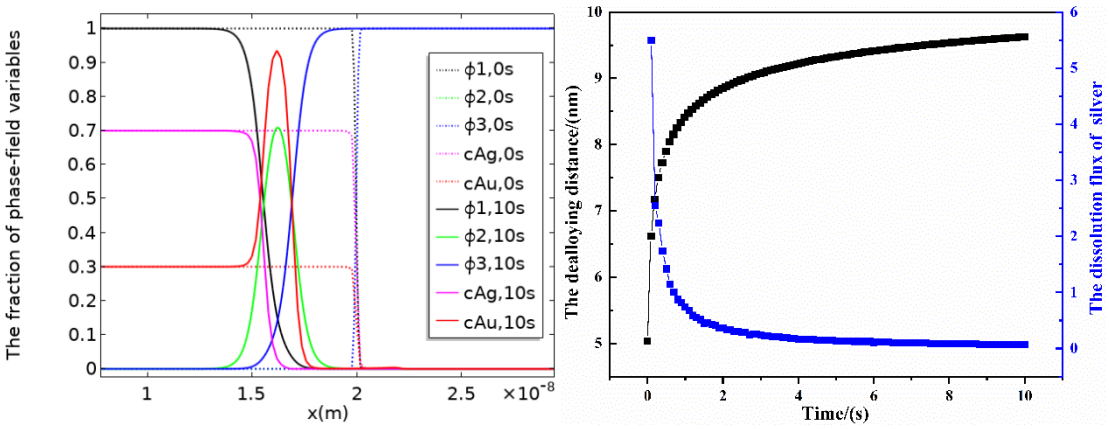

(a) (b)

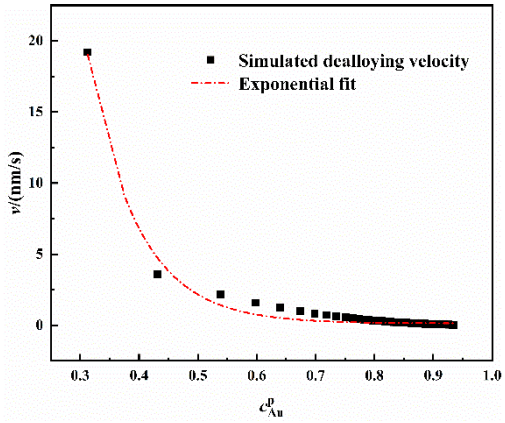

(c)

Figure 3.2 One-dimensional simulation result for $Ag_{0.7}Au_{0.3}$ immersed in 10.9 mol/L nitric acid at t = 10 s: (a) evolution of phase-field variables, (b) dealloying front position and dissolution flux of Ag as functions of time, and (c) dealloying velocity as a function of the peak concentration of Au in the solid-liquid interface layer.

3.4.2 Two-dimensional PF model results

Unlike the 1-D case where the Au accumulation hinders the dealloying frontier advancement, the Au buildup can cause the lateral formation of Au-rich phases along the alloy–electrolyte interface in 2-D. Fig. 3.3 shows the periodic distribution of the Au-rich phase at an early stage of dealloying with different noise amplitudes, where ϕ_1 is presented in blue, ϕ_2 in yellow, and ϕ_3 in red. The figure shows that the nucleation of ϕ_2 perturbs the stability of the planar dealloying front. Moreover, it shows that a stronger magnitude of ξ_0 can shorten the nucleation incubation period and increase the nucleation density, while not affecting the thermodynamic characteristics substantially [67]. It is challenging to observe the initial density of the ligaments

experimentally, making it difficult to calibrate the amplitude of the noise term according to the experimental results. Here, to improve the computation stability, we choose a smaller amplitude in the following simulations.

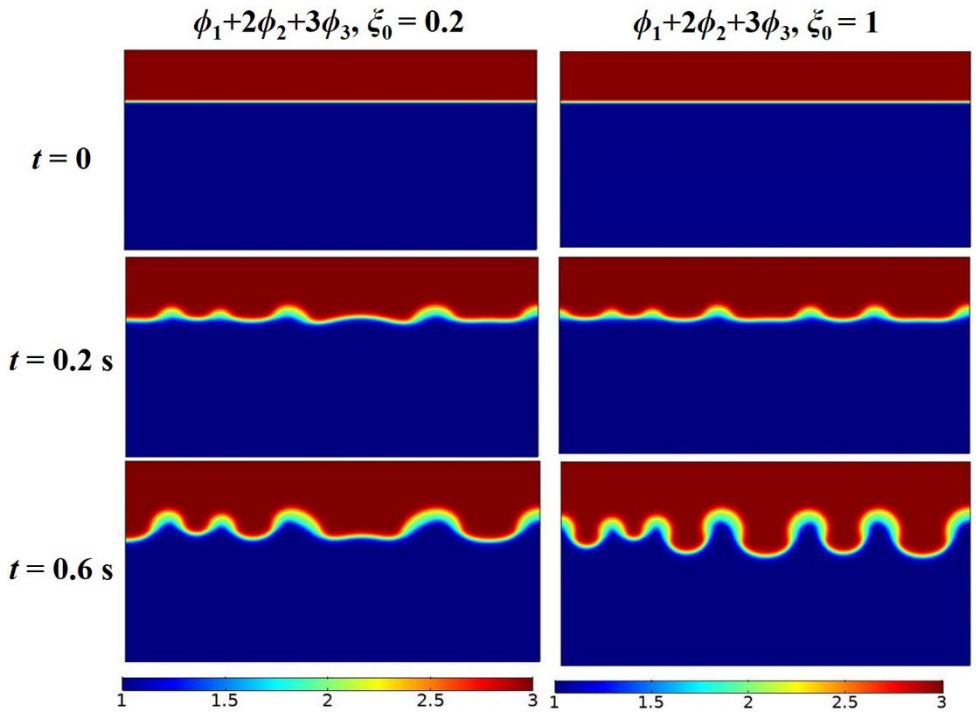

Figure 3.3 Two-dimensional simulation results for the nucleation events in $Ag_{0.7}Au_{0.3}$ dealloyed in nitric acid solution with a concentration of c_a = 10.9 mol/L, showing the formation of Au-rich clusters and initial growth at the solid-liquid interface (left column: $\xi_0 = 0.2$; right column: $\xi_0 = 1$).

To clarify the subsequent evolution of the phases and structure during the dealloying process, snapshots of the microstructures for alloy $Ag_{0.7}Au_{0.3}$ at different times, as well as the metal concentrations, are shown in Fig. 3.4. The nucleation stage leaves etched pits between the Au-rich clusters. These pits become vulnerable sites where the Ag atoms are exposed to the

electrolyte and more Ag atoms are corroded out of the alloy, releasing more Au atoms into the interface layer. Owing to the fast surface diffusion of Au atoms, the Au clusters grow in size, and sometimes, smaller clusters are absorbed by the larger clusters. Such coarsening is fundamentally driven by the reduction in free energy, which is naturally incorporated in PF model. With the continual invasion of the acid solution, some of these Au ligaments finally detach from the alloy, as their basements have a composition equal to that of the virgin alloy. Moreover, certain self-assembled core/shell ligaments with a pure Au surface and alloy interior can be observed. At this point, we can define a characteristic spacing distance λ separating these ligaments, which is on the order of 10 nm in length. Note that unlike the connected porous structure observed through in-plane scanning electron microscopy [68], [69], here, the simulated 2-D structure corresponds to the cross-sectional view of the dealloyed sample.

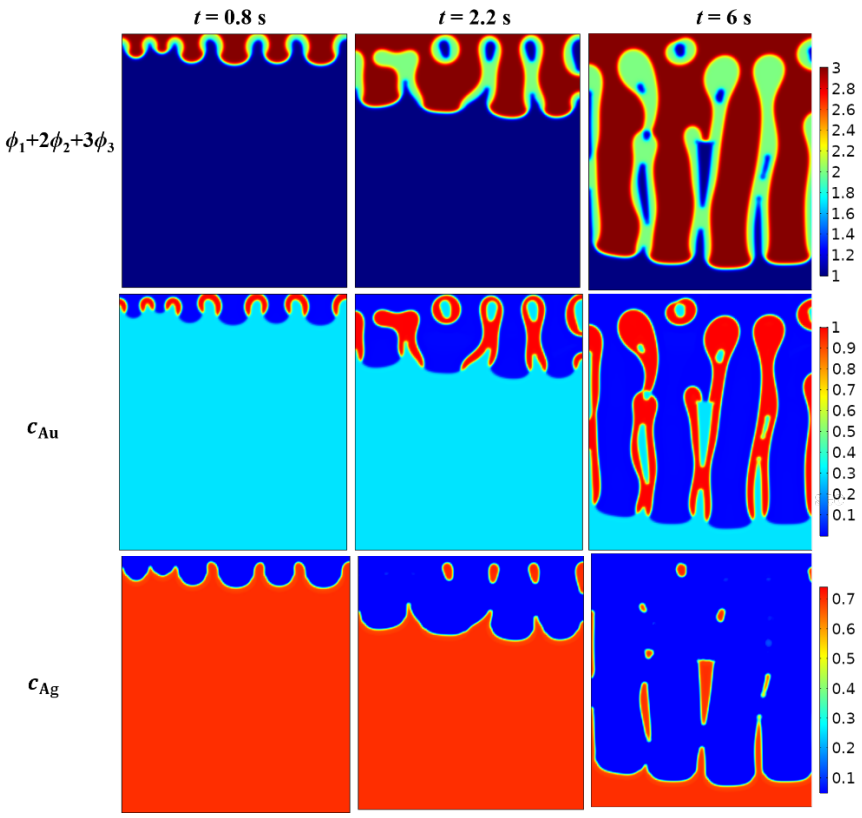

Figure 3.4 Snapshots of 2-D porous morphology evolution for $Ag_{0.7}Au_{0.3}$ immersed in nitric acid solution with a concentration of c_a = 10.9 mol/L.

3.4.3 Effect of chemical content of the electrolyte

Two interface-relevant processes(corrosion and interface diffusion) are found to be decisive for the length scale of porosity, which implies that any dealloying condition that affects the interface behaviors can be treated as a controllable parameter for tailoring the porous structure with desirable morphology and composition. In this section, we focus on the parameters that affect the dissolution rate of LN elements. Experimentally, a marked boundary separating the porous structure from the virgin alloy, known as the dealloying front, is observed. By tracking the dealloying front as a function of time, we can quantitatively evaluate the dealloying kinetics.

We assume that the effect of the nitric acid concentration on the reaction activation energy follows the below linear relation:

$$G = G_0 + k_1 c_a , \tag{3.15}$$

where the characteristic parameters can be calibrated as G_0 = 1.154 eV and k_1 = −0.0099 for $Ag_{0.7}Au_{0.3}$ dealloyed at c_a = 9.1 and 10.9 mol/L by approximating the simulated dealloying rate to the experimental value [44]. Using these calibrated values, we perform simulations with different acid concentrations (c_a = 9.1, 10.9, 12.7, and 14.6 mol/L). In each case, three simulations with the same noise amplitude but different random seed numbers are conducted. Fig. 3.5(a) plots a graph of the dealloying depth vs. the dealloying time by tracking the position of the contour line of ϕ_1 = 0.5 at the ligament roots near the dealloying front. The dealloying fronts in all cases travel the same maximum distance. The relation between the dealloying front position and time can be approximated by linear functions, where the slopes provide the dealloying front propagation rate. Fig. 3.5(b) indicates that the dealloying front velocity increases exponentially with the concentration of nitric acid, which agrees well with the experimental data.

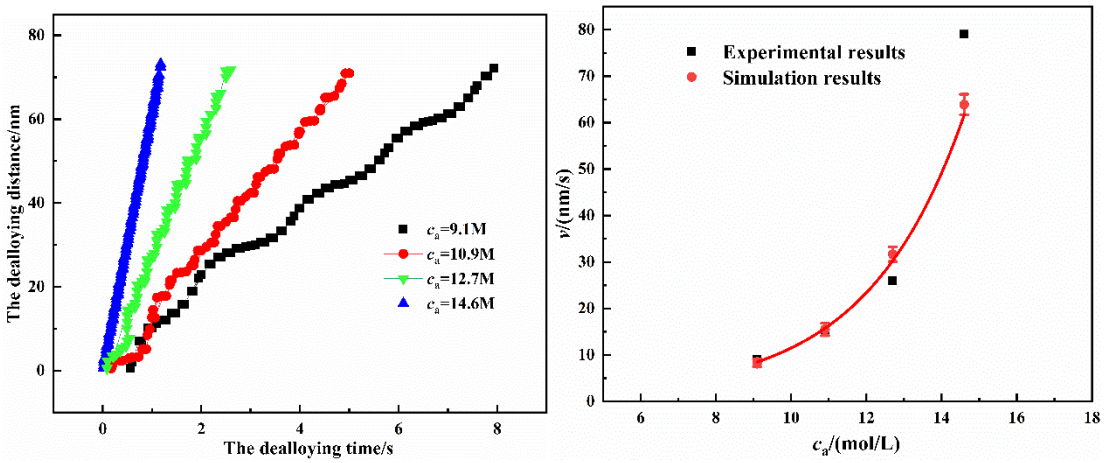

(a) (b)

Figure 3.5 Two-dimensional simulation results for the evolution of dealloying front in $Ag_{0.7}Au_{0.3}$ immersed in electrolytes with different acid concentrations: (a) predicted dealloying distance vs. time ; (b) comparison with experimental results [44].

The simulated microstructure morphologies of $Ag_{0.7}Au_{0.3}$ in different acid solutions when the dealloying fronts travel to the same depths are shown in Fig. 3.6. The ligaments with thickness ranging from 3 to 25 nm penetrate the entire dealloyed area. When the alloy is exposed to an electrolyte with a high acid concentration, the dealloying front advances too quickly to enable the MN elements to passivate the alloy, resulting in a higher density of pure Au ligaments with smaller thickness, and is more likely to detach from the dense alloy. In contrast, in a low-concentration acid, the Ag dissolution rate is low, and thus, Au atoms have more opportunity to passivate the original alloy, resulting in much thicker ligaments with core/shell structures. In the following, these alloy trapped inside the core of ligaments will be further exposed into the electrolyte by a diffusive restructuring of these formed ligaments, while the dealloying front

continually proceeds into the master alloy. Many experiments have shown that the fraction of residual Ag in the dealloyed structure decreases concurrently with the coarsening of ligaments during chemical dealloying, which indicates that structure coarsening contributes to the further etching of alloy [39], [70]. The etching of dealloyed ligaments is similar to the dealloying of nanoparticles. However, the latter operates by a vacancy diffusion mechanism by which Ag diffuses into the surface layer via a Kirkendall effect, causing a hollow core-shell structure, which has not happened [71], [72]. The simulation here also found that the change of bulk diffusion coefficient has no effect on the nanoporosity evolution. This verifies that the coarsening of ligaments mainly arises from the surface diffusion of Au atoms, leading to the collapse of some ligaments onto adjacent ones and further dissolution of the alloy during this secondary dealloying step. Besides the ligament size, the ligament spacing also scales with the acid concentration, as illustrated in Fig. 3.6; the higher is the acid concentration, the smaller is the ligament spacing.

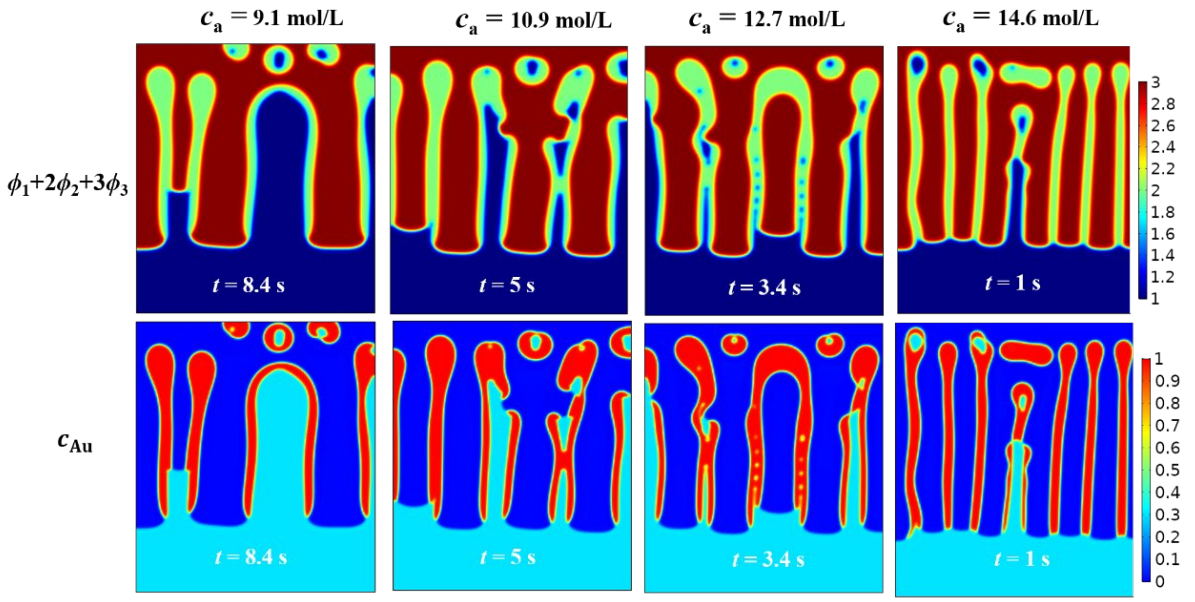

Figure 3.6 Effect of acid concentration on microstructure evolution for $Ag_{0.7}Au_{0.3}$ in 2-D geometry.

3.4.4 Effect of precursor alloy composition

We also establish a similar function as Eq. (3.15) to incorporate the effect of the precursor alloy composition, because a linear correlation between the precursor alloy composition and reaction activation energy is found in the experiments reported in reference [63]. For the numerical tests, we choose a set of alloys with different initial Au compositions (c_0 = 0.2, 0.25, 0.3, and 0.35). In each alloy, three simulations with the same noise amplitude but different random seeds are also conducted. A series of constant dealloying-front evolution processes dependent on the initial alloy composition is observed in Fig. 3.7(a). These results are in good agreement with those obtained for the in situ imaging measurements, which implies that the present PF model correctly reproduces the dealloying kinetics. Note that due to the lack of experimental

measurement, the combined effect of alloy composition and acid concentration is difficult to calibrate, and thus, beyond the scope of this paper.

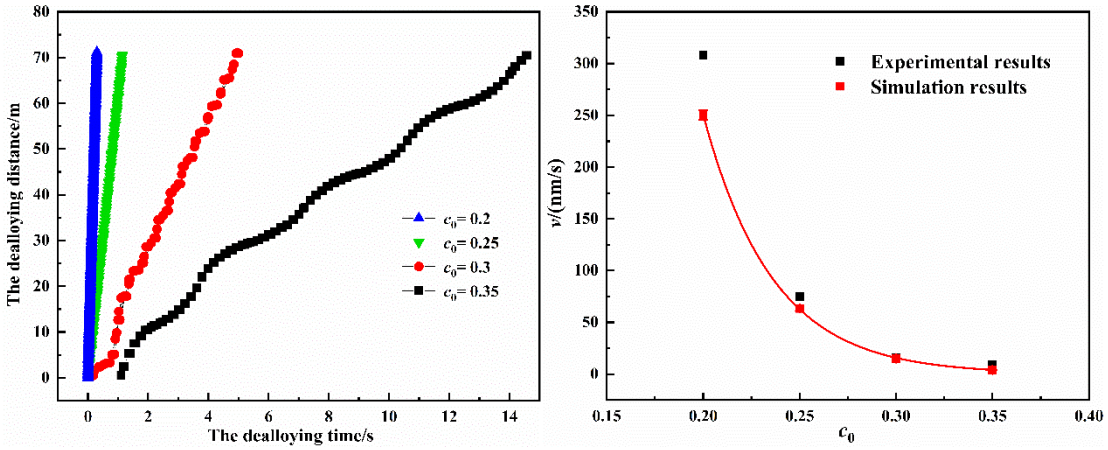

(a) (b)

Figure 3.7 Two-dimensional simulation results for the evolution of dealloying front in $Ag_{1-c_0}Au_{c_0}$ immersed in the electrolyte with c_a = 10.9 mol/L: (a) predicted dealloying distance vs. time; (b) comparison with experimental results [44].

Fig. 3.8 presents the simulated microstructure when the dealloying fronts travel the same depths of different initial alloys in the same acid solution. It can be seen that the lower is the Au content, the smaller are the ligament thickness and ligament spacing. The content threshold (or parting limit) of the initial alloy originally defines the ratio of MN elements, above which the electrochemical dealloying is hindered by a passive layer of MN elements irrespective of applied potential [12]. The content threshold for fcc binary alloy is usually found to be 40 ~ 50 at% according to the percolation model, KMC simulation, and experimental observations [44], [73]. In situ imaging [44] found that $Ag_{0.6}Au_{0.4}$ achieved a shallow dealloying depth before the

dealloying front stopped. An experiment in Ref [22] reported that the chemical dealloying of Ag-Au is weakened when c_0 is greater than 0.4, manifested in a slight increase of Au content after dealloying. However, there has been no microscopic evidence of passivation, making it difficult to determine the content threshold. Fig. 3.8 shows that $Ag_{0.55}Au_{0.45}$ presents a surface shallow dealloying. This is because the dissolution of Ag is slow, and more Au atoms spread on the surface, preventing the development of porosity evolution. In contrast, for the leanest alloy (c_0 = 0.2), the ligaments fall apart into small nanoscaled blobs due to the fast corrosion rate and insufficient Au content in the initial alloy. Hence, this model provides a convenient tool to determine the parting limits (or content thresholds) for porous formation during chemical dealloying.

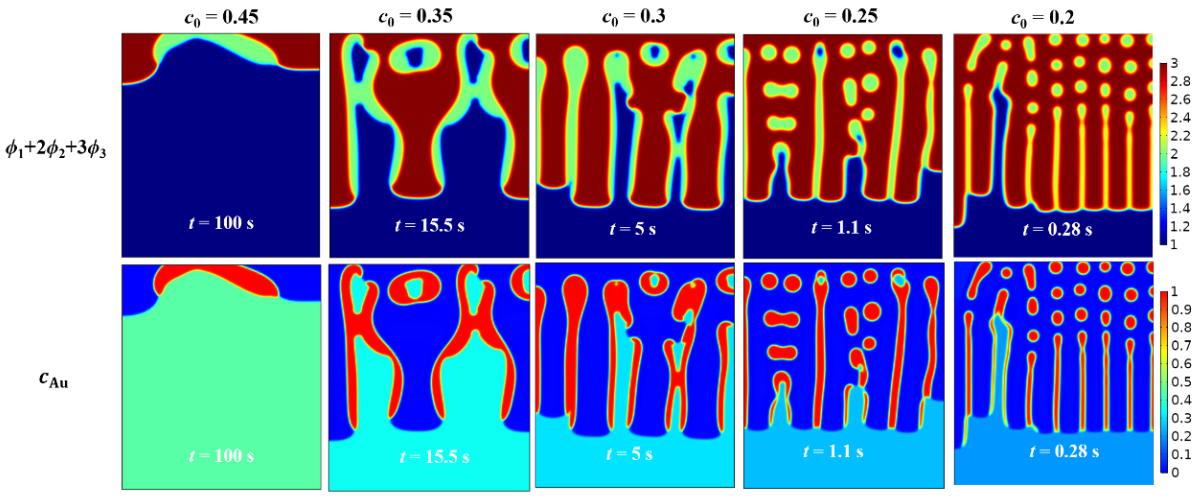

Figure 3.8 Microstructure evolution for a set of alloys with different initial compositions dealloyed in an electrolyte of c_a = 10.9 mol/L in 2-D geometry.

3.4.5 Effect of dimensionality

To study the morphology differences dependent on the dimensionality in detail, 3-D microstructures of the precursors with different initial composition are shown in Fig. 3.9. The first column shows the structure evolution of three phases (ϕ_1, grey; ϕ_2, red; ϕ_3, blue) in a transparent mode in each case. The hidden of the liquid phase in the second column can better present the dealloyed structure. In order to observe the alloy remained in the ligaments, the iso-value surface of $\phi_1 = 0.5$ and iso-concentration surface of $c_{Au} = 0.5$ are shown in the third column of Fig. 3.9. Similar to the 2-D results described above, the dealloying velocity increases with the decrease of c_0. The size of the ligaments increases with c_0, and more alloy relics are wrapped in the ligaments when the dealloying fronts pass over the distance. However, the 3-D ligaments appear as nanoscale entanglements with a random network arrangement and present better connectivity than in 2-D geometries because there is more topological genus associated with interface instabilities and bifurcation in a 3-D geometry. Animations of the cases in Fig. 3.9, S_1, S_2, S_3, and S_4, are also available in Supplementary Material to better visualize the dealloying process.

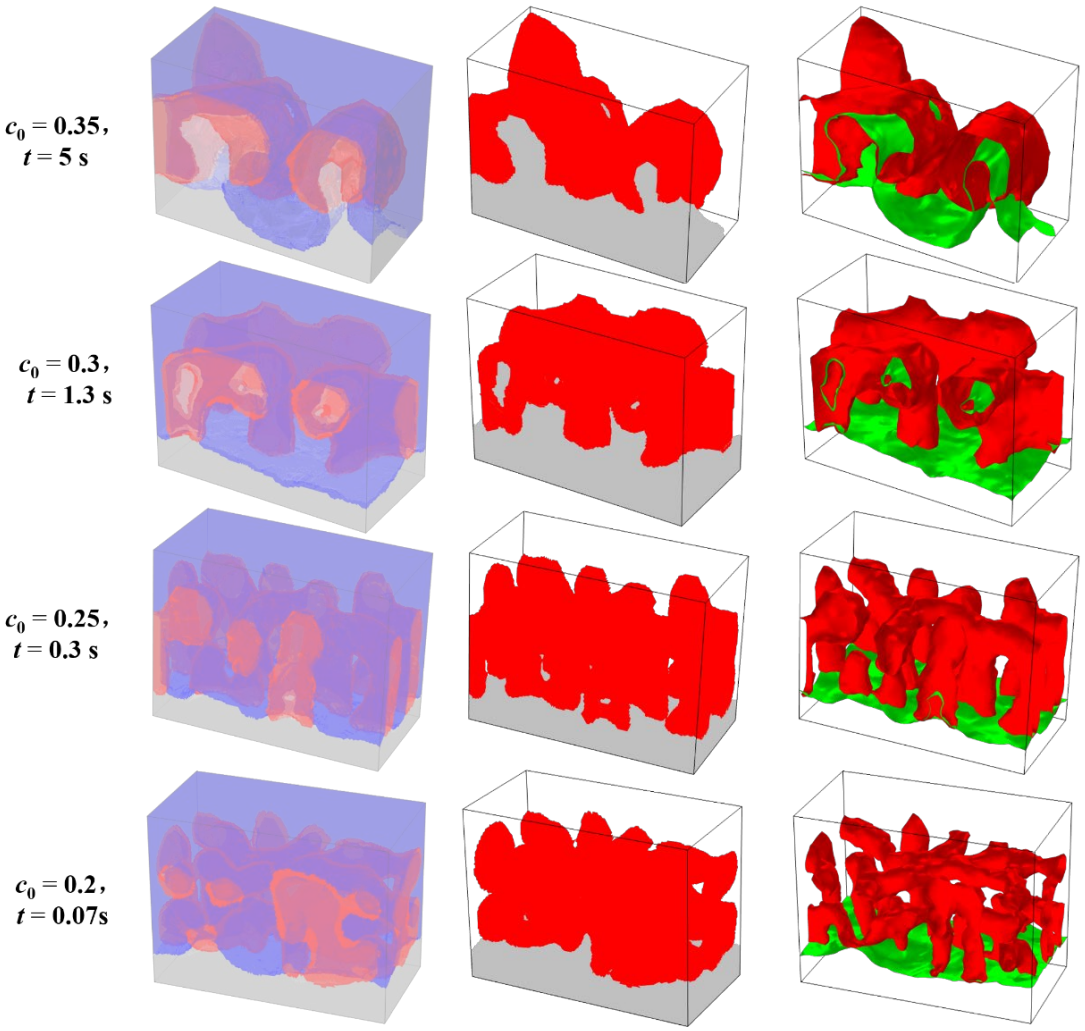

Figure 3.9 3-D microstructure evolution for $Ag_{1-c_0}Au_{c_0}$ dealloyed in the electrolyte of c_a = 10.9 mol/L: the first column shows all phases during porous formation (alloy phase: gray; Au-rich phase: red; electrolyte phase: blue); the second column shows the evolution of the Au-rich phase (red) and electrolyte phase (blue); in the third column, the green surface represents an iso-value surface of ϕ_1 = 0.5, demarcating the dealloying front, and the red surface represents an iso-concentration surface of c_{Au} = 0.5, demarcating the Au-rich phase.

Owing to the limitation of the simulated areas, it is difficult to extract reliable quantitative and statistically meaningful information on the characteristic length scale of the porous structure from the above 2-D simulations. However, the apparent distinction in morphology, associated

with a set of samples dealloyed under different conditions, yields a qualitative comparison analysis by extracting the characteristic size of ligament spacing. Fig. 3.10 confirms a decrease in the ligament spacing with an increase in the acid concentration and Ag content. The average ligament spacing in each case can be calculated by sampling the distances between the centerline of the ligaments in all simulations with different random seeds. As there is no related quantitative research on the evolution of ligament spacing in 2-D cross-section morphology, we try to ensure consistency in the magnitude with the previous experiments[68], [69]. Note that due to the limited connectivity in 2-D geometry and simulation time, the ligament coarsening of the ligaments cannot be adequately observed; thereby, the potential variation in ligament spacing along the dealloying depth is ignored. The data presented in Fig. 3.10 indicate the ligament spacing at the dealloying front. Such predictions are consistent with the experimental observations as well as the KMC simulations, which show that the ligament spacing decreases with increasing electropotential[25], [36], [68].

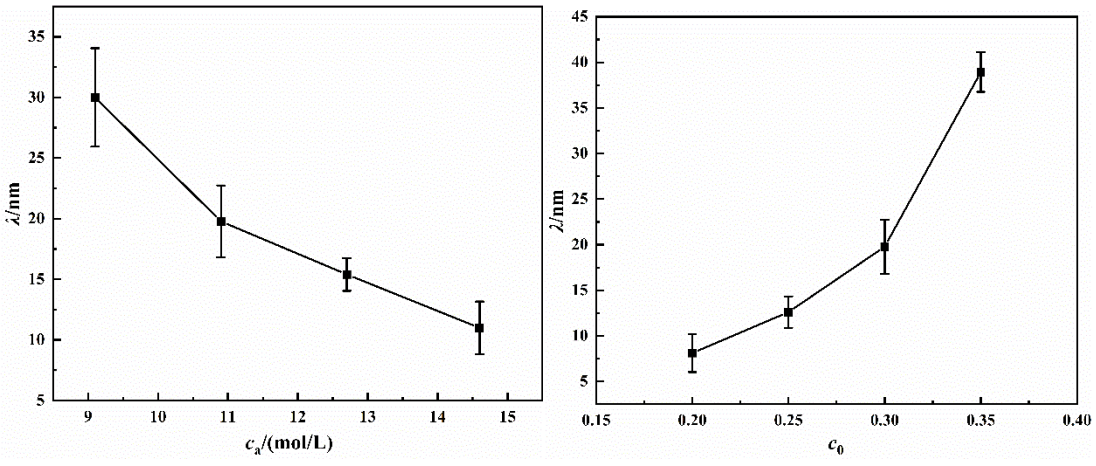

(a) (b)

Figure 3.10 Effects of acid and alloy concentrations on ligament spacing in 2-D geometry.

3.4.6 Effect of surface diffusion coefficient

Many studies have shown that the addition of halides to the electrolyte can increase the ligament spacing, and estimated that the surface diffusivity of Au is three orders of magnitude higher with the addition of KI halide than that without it [74]. In addition, it has been found that a low dealloying temperature results in an ultrafine nanoporous structure [75]. Hence, we investigate the role of diffusion of MN elements in the dealloying process by varying the value of the surface diffusion coefficient. The resultant structures are shown in Fig. 3.11. Many previous studies have focused on the measurement of the surface diffusion coefficient of Au element in electrolyte solutions, but have obtained considerably different results [12], [32], [74], [76]. The measurement results are substantially dependent on the electrochemical surface reaction system, absorbates of the electrolyte solutions, and surface geometry. Moreover, compared with the coarsening stage, Au atoms can aggregate into clusters more quickly when they are just released by Ag corrosion. Here, we assign the same value to the surface diffusivity of Ag and Au as that obtained from reference [32], after making a curvature correction. As shown in Fig. 10, when the diffusion coefficient is 2×10^{-15} m^2/s, the surface diffusion of the MN elements is too slow, and thus, the Au atoms can neither form clusters nor provide liquid paths for Ag corrosion to proceed, thus leaving a Au passivation layer on the alloy surface. This result is similar to that

obtained by Hakamada et al.[77], who reported that during the electrical dealloying of $Pd_{0.2}Co_{0.8}$, the Pd aggregation appeared to be inhibited, resulting in passivity, even after the application of sufficient electrode potential. Upon increasing the value of the surface diffusion coefficient, the aggregation of MN elements forms Au clusters and the corrosion process continues through the creation of a contact area with the electrolyte. Therefore, the rapid surface diffusion of MN elements is essential for the formation and evolution of a porous structure. Furthermore, the dealloyed structure exhibits an inverse relation with the surface diffusion coefficient: the higher is the surface diffusion coefficient, the thicker are the ligaments and the larger is their spacing.

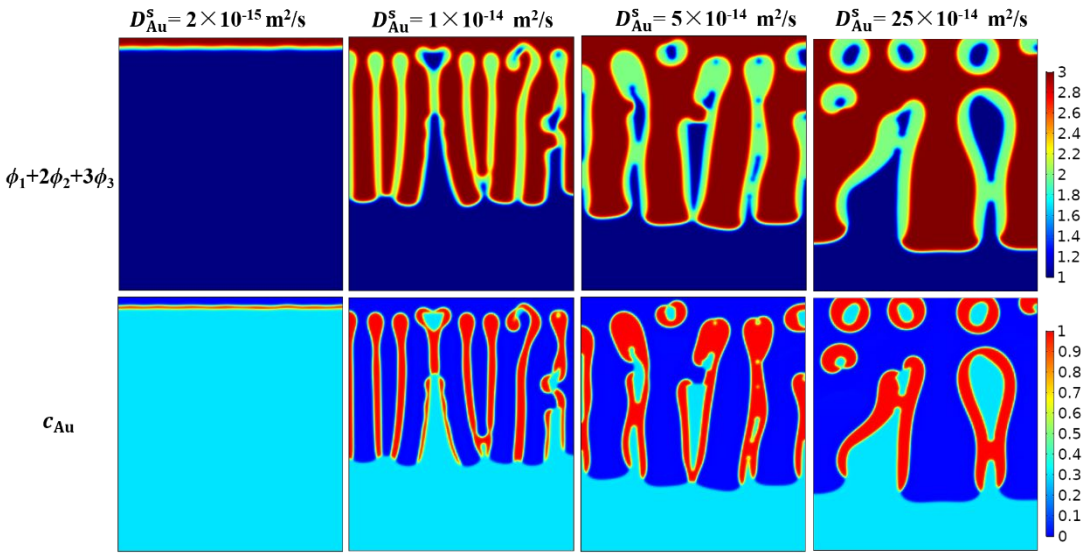

Figure 3.11 Effect of surface diffusivity of Au and Ag on microstructure morphology in $Ag_{0.7}Au_{0.3}$ dealloyed in the electrolyte of c_a = 10.9 mol/L at t = 5 s.

Although the size, spacing, and composition of the ligaments vary with the dealloying conditions, in each case of a different characteristic length, the morphology presents a eutectic structure evolution process. The changes in the dealloyed structure with respect to the precursor

alloy and acid concentration can be quantitatively assessed by the interface diffusion behavior of MN elements. Based on the theoretical study in reference [20], the characteristic ligament spacing of the nanoporous structure in liquid-metal dealloying is predicted as $\lambda \propto \sqrt{D_{\mathrm{Au}}^{\mathrm{s}}/(vc_0)}$, which is also observed in our simulations. Although liquid-metal dealloying is controlled by the diffusion of the miscible element in liquid, the ligament spacing is controlled by diffusion and the mass conservation law both in the liquid-metal dealloying and chemical dealloying, as shown in Fig. 3.12. As an example of $Ag_{0.7}Au_{0.3}$ dealloyed at c_a = 9.1, 10.9, 12.7, and 14.6 mol/L, Fig. 3.12(a) indicates that λ is proportional to $1/\sqrt{v}$. Fig. 3.12(b) validates the scaling law through the linear fit between λ and $1/\sqrt{(vc_0)}$ for $\mathrm{Ag}_{1-c_0}\mathrm{Au}_{c_0}$ (c_0 = 0.2, 0.25, 0.3, 0.35) dealloyed at c_a = 10.9 mol/L. Fig. 3.12(c) provides a linear fit between λ and $\sqrt{D_{\mathrm{Au}}^{\mathrm{s}}/v}$ in the case of $Ag_{0.7}Au_{0.3}$ dealloyed at c_a = 10.9 mol/L with different surface diffusivities for Au ($D_{\mathrm{Au}}^{\mathrm{s}}$ = 1 × 10^{-14} m^2/s, 5 × 10^{-14} m^2/s, 25 × 10^{-14} m^2/s).

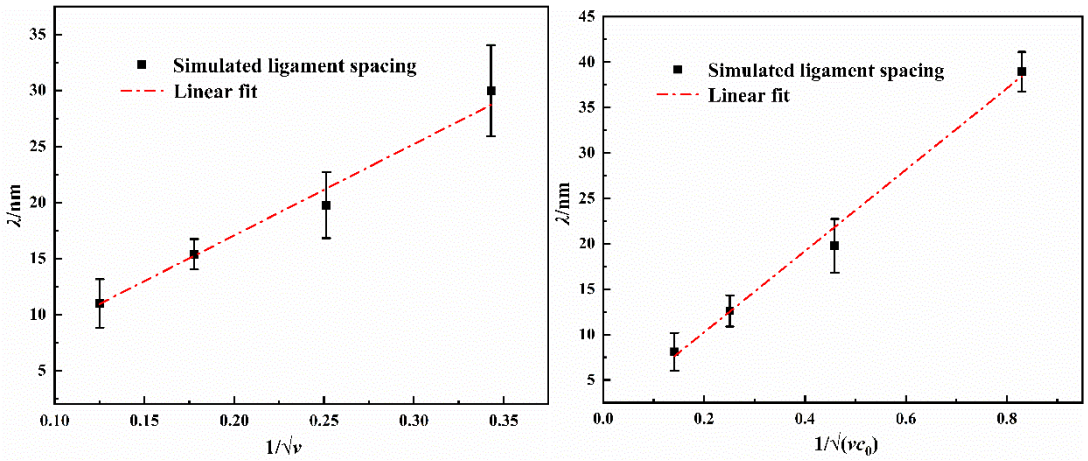

(a) (b)

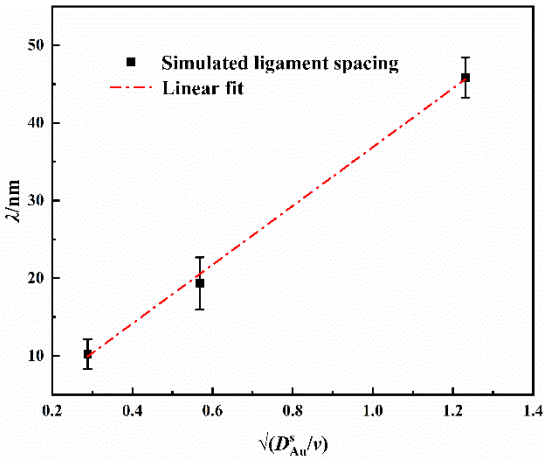

(c)

Figure 3.12 Validation of ligament spacing law. (a) Effect of acid concentration on ligament spacing for $Ag_{0.7}Au_{0.3}$, $\lambda \propto 1/\sqrt{v}$; (b) effect of alloy composition on ligament spacing, $\lambda \propto 1/\sqrt{vc_0}$, for $Ag_{1-c_0}Au_{c_0}$ in acid of concentration 10.9 mol/L; and (c) the effect of surface diffusion coefficient on ligament spacing, $\lambda \propto \sqrt{D_{Au}^{s}/v}$, for $Ag_{0.7}Au_{0.3}$ in the acid of concentration 10.9 mol/L; the red dashed lines indicate linear fits.

Chapter 4 MPF MODEL OF THE EVOLUTION KINETICS OF POROUS STRUCTURES DURING ELECTROCHEMICAL DEALLOYING

4.1 INTRODUCTION

Electrochemical dealloying refers to a process that the more active species are electrochemically selectively removed from the alloy by virtue of the difference of standard electrode potentials of alloy components, resulting in a porous residue. The electrochemical tests are carried out in an electrochemical cell that includes a counter electrode, reference electrode, and working electrode (precursor) [78], [79]. Experiments have demonstrated that applied electropotential could decrease the activation energy of corrosion reaction and increase the surface diffusion coefficient of metal elements [80]. Hence, compared to chemical dealloying, electrochemical dealloying has the advantage of precise control over the dealloying velocity, morphology, and composition of porous metals by adjusting the applied potential or current [81]–[83]. In addition, potential control allows that dealloying can be carried out in neutral salt solutions such as $AgNO_3$ and NaCl solution, which are easy-handled and relatively economical [80], [84]–[86]. Therefore, the well-tuned current or potential, electrolyte solutions, and accurate adjustment of pore size offered by electrochemical dealloying trigger extensive research about the electrochemical dealloying method. Current efforts in research focus on the experimental investigation of the effect of potential on microstructure. However, it is essential to capture the electrochemical driving force and understand how different dealloying

parameters affect the morphology evolution. Therefore, understanding the underlying physical mechanism and subsequently modeling and simulating the microstructural evolution during electrochemical dealloying are crucial. This will help inform the development of new dealloyed porous structures of common alloy families by explicitly considering their key electrochemical reactions and physical processes.

In this chapter, we aim to formulate a thermodynamically consistent MPF model to describe the evolution kinetics of NPMs and to examine the influence of controllable parameters during the electrochemical dealloying of a binary alloy. In the MPF model for chemical dealloying, any point in the system is a mixture of three coexisting phases with different phase compositions but equal chemical potential. The first step is to solve the distribution of phase compositions of all components; then, the driving force is calculated. However, when the electrostatic energy is incorporated into the system's free energy, the quasi-equilibrium equation at the interface will become complicated, making it difficult to extend this model to electrochemical dealloying. In another example, a non-linear PF model deduced from the Butler–Volmer reaction rate theory was used to investigate the lithium electrodeposition [56]. This model is a unification of classical chemical reaction theory and the Allen-Cahn equation, which naturally incorporates the electrochemical driving force. More recently, our group has extended these two models by considering the effects of mechanical stress, passivation films, chemical reactions, and ion transport in corrosion and stress corrosion cracking [55], [57]–[60]. Therefore, based on this model, we presented a formulation of the MPF model that can account for the electrochemical

corrosion of alloy. We have demonstrated that a nucleation growth mechanism could successfully reproduce the aggregation of Au clusters and explain the porosity formation. Following the previous work about chemical dealloying, we use classical nucleation theory to describe the aggregation of au atoms and incorporate the free energy of Au atoms using parabolic functions.

This chapter is organized as follows. We first describe the formulation of a MPF model based on the electrochemical reaction kinetics and the classical nucleation theory. In this MPF model, the non-linear evolution of a precursor–electrolyte interface is used to account for Butler–Volmer-type current–potential behavior, while the classical nucleation–growth theory is used to account for the formation and growth of porous clusters. We then discuss in detail the dominant mechanism that accounts for dealloying kinetics and how these are influenced by electropotential characteristics and by precursor compositions.

4.2 METHOD

4.2.1 Investigated system

Ag–Au alloy is taken as the model system to describe the PF model of electrochemical dealloying. First, the Ag–Au alloy is immersed in 0.1 M perchloric acid ($HClO_4$), and the Ag atoms ionize under an applied electrochemical potential, as follows (Eq. 4.1):

$$Ag \rightarrow Ag^{+} + e^{-} \tag{4.1}$$

The released electrons then flow to the cathode surface and trigger the cathodic reaction, which is not considered here. If the cathodic reaction becomes the rate-determining step, it will be easy to incorporate it into the current model (as detailed in Appendix C in our published work [57]). It has been suggested that the rearrangement of Au atoms at the precursor–electrolyte interface during the dealloying of Ag–Au alloy is a phase-separation mechanism and does not require the nucleation of new crystallites [25]. However, it is doubtful that this mechanism can explain the dealloying of some binary intermetallic compounds, given the disparity between the crystal lattice structures of their precursor and porous metal phases. For example, it is obvious that the nucleation and growth processes are required for the LN elements in AlAu precursor (monoclinic) and Al_2Cu precursor (body-centered tetragonal) to reconstruct NPG (f.c.c) and nanoporous copper (f.c.c.), respectively [26], [78]. Hence, following previous work on chemical dealloying [87], we develop a MPF model based on a nucleation–growth mechanism to reveal the physical processes underlying the electrochemical dealloying of binary alloys.

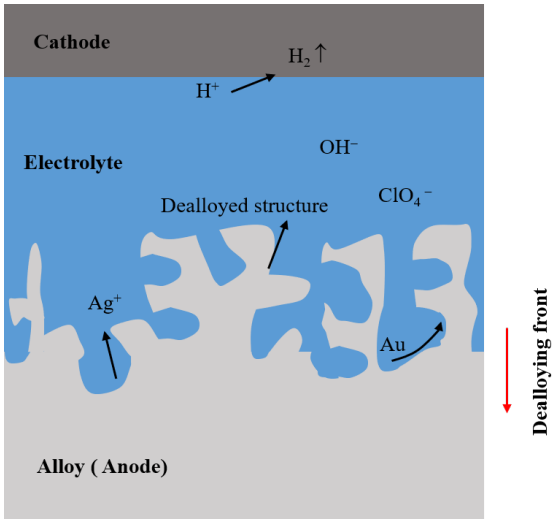

Figure 4.1 Schematic diagram illustrating the electrochemical dealloying of Ag–Au alloy

4.2.2 Multi-phase-field model

Gibbs free energy of the system

The Gibbs free energy of the system is expressed as

$$G = \int_V f_{\text{chem}}(\phi_i, c_k) + f_{\text{grad}}(\nabla \phi_i) + f_{\text{elec}}(\varphi) dV \quad , \tag{4.2}$$

where ϕ_i (i = 1, 2, or 3) are the set of order parameters describing local phase fractions of three coexisting phases, i.e., the alloy phase (ϕ_1 = 1, and $\phi_2 = \phi_3 = 0$), the Au phase (ϕ_2 = 1, and $\phi_1 = \phi_3 = 0$), and the electrolyte phase (ϕ_3 = 1, and $\phi_1 = \phi_2 = 0$); ϕ_3 is a dependent variable, and thus $\phi_3 = 1 - \phi_1 - \phi_2$; c_k (where k = Ag, Au, Ag^+, and e^-) denotes the dimensionless concentration of component k, which is defined as $c_k = C_k/C_{\text{ref}}$, where C_k is the molar concentration of component k, and C_{ref} is the reference concentration defined by the molar concentration of alloy ($C_{\text{ref}} = 9.7 \times 10^4$ mol/m^3); φ is the electrostatic potential; and f_{grad} is the gradient term associated with the interfacial energy and is expressed as $\varepsilon/2\sum_i(\nabla\phi_i)^2$, where ε is the gradient energy coefficient and is defined as $\varepsilon = \frac{\sigma l}{4\sqrt{2}a}$ (σ is the interfacial energy; l is the interfacial thickness; and a is a numerical constant) [54]. For simplicity, all interfaces are assumed to have the same properties. The electrostatic energy density f_{elec} is given as $f_{\text{elec}} = \sum_k C_k n_k F \varphi$, where n_k is the charge number of component k, and F is Faraday's constant.

The starting point for this work is a nonlinear PF model introduced by Chen et al. [56] that incorporates the interfacial energy and electropotential energy, accounts for Butler–Volmer electrochemical reaction kinetics, and is applied to an electrodeposition system. Chen et al. used an order parameter to represent the local physical state of a metal in a metal–electrolyte two-

phase system, and as this parameter equated to the molar fraction of metal (lithium), its evolution followed the electrochemical reaction rate theory. Based on this model, we use $\phi_1 = c_{Ag}/c_{Ag,0}$ (where $c_{Ag,0}$ is the alloy's initial Ag concentration) to establish a physical correspondence of ϕ_1 to the dimensionless alloy concentration. Thus, $c_{Ag} = c_{Ag,0}$ corresponds to the alloy phase ($\phi_1 = 1$) and $c_{Ag} = 0$ corresponds the Au or electrolyte phase ($\phi_1 = 0$). To ensure that our PF model is applicable to multi-element alloys, we also incorporate the effect of the MN element in the alloy during the electrochemical. This effect of the MN element is represented by the free energy of the porous cluster phase and a term for the enthalpy of mixing in the precursor that impinges significantly on the dissolution of the LN element. Therefore, f_{chem}, the chemical free-energy density, is evaluated as

$$f_{\text{chem}} = \sum_i W\phi_i^2\left(1-\phi_i\right)^2 + C_{\text{ref}}\sum_* c_*\left(\mu_*^{\ominus} + RT\ln c_*\right) + \sum_i h_i f_{\text{Au}}^i + \alpha c_{\text{Ag}}\left(1-c_{\text{Ag}}\right), \tag{4.3}$$

where the first term is the sum of the potential barriers of height W between the bulk phases used to distinguish local phases, where $W = \frac{\sqrt{2}a\sigma}{4l}$ [54]; the second term is the chemical free energy of species $*$($*$ = Ag^+ and e^-) as an ideal solution, where $\mu_*^{\ominus}$ is the standard chemical potential, R is the gas constant, and T is the temperature; and the third term represents the chemical free energy of the Au component, which is the driving force of Au diffusion. It is assumed that a fraction h_i of the free energy density of Au for each phase (f_{Au}^i) contributes to the free energy of the interfacial region, where ($h_i = \phi_i^2 \big/ \sum_j \phi_j^{\ 2}$). f_{Au}^i is approximated by a parabolic function, expressed as $f_{\text{Au}}^i = A\left(c_{\text{Au}}^i - c_{\text{Au,e}}^i\right)^2$, where A is the free energy curvature and $c_{\text{Au,e}}^i$ is the dimensionless equilibrium concentration of Au in the three phases listed in Table 3.1. In this model, we assume that local Au concentration (c_{Au}) is defined as it is in Eq.

(4.4), which corresponds to the assumption in the KKS model [88]. The third term in (4.3) thus represents the negative enthalpy of mixing for a binary alloy, where α is the interaction energy coefficient between Ag and Au. Thus, in this model, the dissolution of Ag corresponds to the consumption of the alloy phase and acts as a non-equilibrium stimulus to promote the evolution of the system toward the equilibrium state. That is, where $\phi_1 = 1$, $\phi_2 = \phi_3 = 0$, $c_{\mathrm{Ag,e}} = c_{\mathrm{Ag,0}}$, and $c_{\mathrm{Au,e}} = c_{\mathrm{Au,0}}$ in the alloy phase; $\phi_2 = 1$, $\phi_1 = \phi_3 = 0$, $c_{\mathrm{Ag,e}} = 0$, and $c_{\mathrm{Au,e}} = 1$ in the Au phase, and $\phi_3 = 1$, $\phi_1 = \phi_2 = 0$, and $c_{\mathrm{Ag,e}} = c_{\mathrm{Au,e}} = 0$ in the electrolyte phase (where $c_{\mathrm{Ag,e}}$ and $c_{\mathrm{Au,e}}$ are the equilibrium concentrations of Ag and Au).

$$c_{\mathrm{Au}} = \sum_{i=1}^{3} h_i c_{\mathrm{Au}}^{i}, \frac{\partial f_{\mathrm{Au}}^{1}}{\partial c_{\mathrm{Au}}^{1}} = \frac{\partial f_{\mathrm{Au}}^{2}}{\partial c_{\mathrm{Au}}^{2}} = \frac{\partial f_{\mathrm{Au}}^{3}}{\partial c_{\mathrm{Au}}^{3}} = \mu_{\mathrm{Au}} \tag{4.4}$$

Interfacial movement

Based on Butler–Volmer reaction kinetics [89], the dissolution rate of Ag in the alloy has the variational form of

$$r_{\mathrm{Ag}\rightarrow\mathrm{Ag}^{+}} = L \times \mu_{\mathrm{int}} + \kappa \left[\exp\left(\frac{\mu_{\mathrm{ini}} + (1-\rho)\Lambda}{RT} \right) - c_{\mathrm{Ag}^{+}} \exp\left(\frac{-\rho\Lambda}{RT} \right) \right], \tag{4.5a}$$

with

$$L = \frac{\kappa}{RT} \exp\left(\frac{\mu_{\mathrm{ini}} + (1-\rho)\Lambda}{RT} \right), \tag{4.5b}$$

$$\Lambda = F(\varphi_{\mathrm{M}} - \varphi) - \mu_{\mathrm{Ag}^{+}}^{\Theta}, \tag{4.5c}$$

$$\mu_{\mathrm{int}} = \frac{W\phi_1(1-\phi_1)(1-2\phi_1) - \varepsilon\nabla^2\phi_1}{C_{\mathrm{ref}} c_{\mathrm{Ag,0}}} - \mu_{\mathrm{Ag}}^{\Theta}, \tag{4.5d}$$

and

$$\mu_{\mathrm{ini}}=\frac{\alpha}{C_{\mathrm{ref}}}\left(1-2c_{\mathrm{Ag},0}\right) \tag{4.5e}$$

In Eqs. (4.5a)–(4.5e), L is the kinetic parameter of the corrosion interface, κ is the kinetic parameter of the electrochemical reaction, Λ is the driving potential of the applied electric field, μ_{int} is the driving potential of the interfacial energy, μ_{ini} is the driving potential of the initial alloy composition, and ρ is a symmetry factor. In Eq. (4.5c), φ_{M} is the electropotential applied to the alloy, and φ is the electrolyte potential. Because μ_{int} is much smaller than RT, μ_{ini} and $\varphi_{\mathrm{M}} - \varphi$ are the main factors driving the dissolution of Ag. A detailed derivation of the dissolution rate is given in Appendix B. Based on the abovementioned relationship between c_{Ag} and ϕ_1, the phase interface (ϕ_1/ϕ_3) migration corresponds to the dissolution of Ag, and the governing equation for ϕ_1 can be expressed as,

$$\frac{\partial\phi_1}{\partial t}=-\frac{r_{\mathrm{Ag}\to\mathrm{Ag}^+}}{C_{\mathrm{ref}}c_{\mathrm{Ag},0}}=-\frac{L\times\left(\mu_{\mathrm{int}}^{12}+\mu_{\mathrm{int}}^{13}\right)}{C_{\mathrm{ref}}c_{\mathrm{Ag},0}}-\lambda_{13}S\frac{\kappa}{C_{\mathrm{ref}}c_{\mathrm{Ag},0}}\left[\exp\left(\frac{\mu_{\mathrm{ini}}+\left(1-\rho\right)\Lambda}{RT}\right)-c_{\mathrm{Ag}^+}\exp\left(\frac{-\rho\Lambda}{RT}\right)\right] \tag{4.6a}$$

where

$$\mu_{\mathrm{int}}^{12}=\frac{W\phi_1\left(1-\phi_1\right)\left(1-2\phi_1\right)-\varepsilon\nabla^2\phi_1-\left(W\phi_2\left(1-\phi_2\right)\left(1-2\phi_2\right)-\varepsilon\nabla^2\phi_2\right)}{C_{\mathrm{ref}}c_{\mathrm{Ag},0}}-\mu_{\mathrm{Ag}}^{\Theta}, \tag{4.6b}$$

$$\mu_{\mathrm{int}}^{13}=\frac{W\phi_1\left(1-\phi_1\right)\left(1-2\phi_1\right)-\varepsilon\nabla^2\phi_1-\left(W\phi_3\left(1-\phi_3\right)\left(1-2\phi_3\right)-\varepsilon\nabla^2\phi_3\right)}{C_{\mathrm{ref}}c_{\mathrm{Ag},0}}-\mu_{\mathrm{Ag}}^{\Theta}, \tag{4.6c}$$

and

$$\lambda_{13} = 4h_1h_3. \tag{4.6d}$$

$$S = 1 - C_{Ag^+} \Big/ C^{sat}_{Ag^+} . \tag{4.6e}$$

Compared to the sharp interfacial form of the electrochemical rate being obtained in Eq. (4.5), μ^{12}_{int} and μ^{13}_{int} are used in Eq. (4.6a) to ensure that all binary interfaces are diffusive in the multi-phase system, and λ_{13} is used to maintain the discontinuity of the interfacial reaction. Moreover, based on the treatment method in [90], Eq. (4.6d) is introduced to confine the corrosion of Ag to the alloy–electrolyte interface. *S* in Eq. (4.6e) is a saturation factor used to express the hindering effect of saturation concentration of silver ion ($C^{sat}_{Ag^+}$) on the corrosion rate [90], where $C^{sat}_{Ag^+}$ = 11.67 mol/L [91].

Thus, the governing equation for ϕ_2 can be derived from the Allen–Cahn equation, that is:

$$\frac{\partial \phi_2}{\partial t} = -\frac{1}{3}\left(L_{12}\left(\frac{\delta G}{\delta \phi_2} - \frac{\delta G}{\delta \phi_1} \right) + L_{32}\left(\frac{\delta G}{\delta \phi_2} - \frac{\delta G}{\delta \phi_3} \right) \right) + \zeta_{\phi_2} , \tag{4.7a}$$

with

$$\zeta_{\phi_2} = r\zeta_0 16\phi_1^2 \left(1-\phi_1\right)^2 I_0 k_B T \, \Delta\Omega_{23}^2 \Big/ \sigma^3 . \tag{4.7b}$$

In Eq. (4.7a), L_{12} and L_{32} are the interfacial mobilities that scale the transition rate from the alloy and electrolyte phase to the Au phase, and following our previous work [87], ζ_{ϕ_2} is a noise term that represents the thermal instability caused by the rapid release of Au onto the surface of the alloy after the Ag is dissolved into the electrolyte, which allows for a unified

treatment of the nucleation of Au clusters. Eq. (4.7b) accounts for the thermal fluctuation at the alloy–electrolyte interface, which is proportional to the chemical free-energy difference between ϕ_2 and ϕ_3, which is expressed as $\Omega_{23}=2A\left(c_{\mathrm{Au}}^{i}-c_{\mathrm{Au,e}}^{i}\right)$ and is inversely proportional to the interfacial energy. In Eq. (4.7b), r is a random number (−1,1), ζ_0 is the fluctuation intensity, and I_0 is the nucleation prefactor. Therefore, Eq. (4.7a) shows that the nucleation and growth of the Au phase of a given system evolve toward the equilibrium state.

Mass diffusion

The Cahn–Hilliard equation for Au has the following form:

$$\frac{\partial c_{\mathrm{Au}}}{\partial t}=\nabla M_{\mathrm{Au}}\nabla\frac{\delta F}{\delta c_{\mathrm{Au}}}=\nabla D_{\mathrm{Au}}\sum_{i}h_i\nabla c_{\mathrm{Au}}^{i}, \tag{4.8a}$$

where

$$M_{\mathrm{Au}}=D_{\mathrm{Au}}\Big/\left(\delta^2 G/\delta {c_{\mathrm{Au}}}^2\right), \tag{4.8b}$$

and

$$D_{\mathrm{Au}}=\sum_{i=1}^{3}h_i D_{\mathrm{Au}}^{i}+\lambda_{13}D_{\mathrm{Au}}^{13}+\lambda_{23}D_{\mathrm{Au}}^{23}, \tag{4.8c}$$

where M_{Au} is the diffusion mobility of Au; D_{Au} is the diffusion coefficient of Au and is dependent on the phase fields, which include bulk and surface diffusion terms; D_{Au}^{i} is the bulk diffusion coefficient in ϕ_i; and $\lambda_{13}=4h_1h_3$ and $\lambda_{23}=4h_2h_3$ are multiplied by the second and third

terms on the right side of the equation to correlate the surface diffusion of Au in the alloy–electrolyte and Au–electrolyte interfaces with D_{Au}^{13} and D_{Au}^{23}, respectively.

Most measurements of the surface diffusion coefficient of Au are based on the evaluation of nanopore size during the coarsening of porous Au ligaments. The surface diffusivity of Au at the Au cluster–electrolyte interface is estimated to be 10^{-20}–10^{-17} m^2/s, depending on the applied electropotential and the nature of the electrolyte solution. As the relaxation rate of roughened Au clusters is related to the grain size and surface curvature of Au, the mobility of Au atoms freshly released from the surface is greater than that of Au atoms located at the Au cluster–electrolyte interface. Some researchers have used the percolation model and in situ scanning tunneling microscopy measurements to determine the surface diffusivity of Au at the alloy–electrolyte interface, which is 4–5 times greater than that at the Au cluster–electrolyte interface. Therefore, we assign the values calculated in [12], [32] and [74], [75] to D_{Au}^{13} and D_{Au}^{23}, respectively, to describe the different mobilities of Au at the ϕ_1/ϕ_3 and ϕ_2/ϕ_3 interfaces.

We assume that the diffusion of Ag in the solid and interface is much slower than the corrosion rate of Ag, and therefore, there is no need to solve another Cahn–Hilliard equation for Ag. The transport of Ag^+ in the electrolyte follows the Nernst–Planck equation, that is:

$$\frac{\partial c_{\mathrm{Ag}^+}}{\partial t} = \nabla\left(h_3 D_{\mathrm{Ag}^+} \nabla c_{\mathrm{Ag}^+} + \frac{h_3 D_{\mathrm{Ag}^+} c_{\mathrm{Ag}^+} F}{RT} \nabla \varphi \right) - c_{\mathrm{Ag},0} \frac{\partial \phi_1}{\partial t} \tag{4.9}$$

where h_3 is used to ensure that the movement of ions only occurs in the electrolyte, and the final term describes the production of Ag^+ by electrochemical corrosion.

Conservation of charge

As the timescale of the dealloying front movement is much larger than that required to achieve steady-state charge accumulation, the conservation of charge can be simplified as

$$\nabla \psi \nabla \varphi = FC_{\text{ref}} \frac{\partial \phi_1}{\partial t}, \tag{4.10}$$

where ψ is the electrolyte conductivity. Based on the assumption of electric neutrality in the electrolyte, variation in the charge as a consequence of variation in the ionic concentration in the electrolyte is ignored. Moreover, based on [92], Eq. (4.10) is used to determine the distribution of electrolyte potential, and a constant electropotential is applied at the metal electrode.

4.3 NUMERICAL IMPLEMENTATION

For the first case, the system is initialized as a metal electrode domain with dimensions of 80 nm × 80 nm and an electrolyte domain with dimensions of 80 nm × 2 μm (shown in Fig. 4.2). The initial values of the order parameters are set as $\phi_1 = 1$ and $\phi_2 = \phi_3 = 0$ in the electrode domain, and as $\phi_3 = 1$ and $\phi_1 = \phi_2 = 0$ in the electrolyte domain, and zero-flux boundary conditions are set on all sides of the domains. The initial concentrations of Au are taken as the equilibrium concentrations in each phase, and zero-flux boundary conditions are also applied to all sides.

To approximate the system, we assign an impurity value ($C_{Ag^+} = 1 \times 10^{-6}$ mol/L) to the initial concentration and boundary concentration of Ag^+ on the top side of the electrolyte domain, as the metal domain is much smaller than the electrolyte domain. Other sides are set with zero-flux boundary conditions, and $\varphi = 0$ V is assigned as the initial value of the electropotential in all domains and as the Dirichlet boundary condition on the top side of the electrolyte domain. All simulations are carried out using COMSOL Multiphysics [93]. To guarantee that the numerical calculations are stable, we use a free quadrilateral mesh method and a uniform grid spacing Δx ($\Delta x = l/5$ in the metal domain and electrolyte domain near the interface, and $\Delta x = 5l$ in the electrolyte domain far from the interface). The time step is automatically refined using a backward differentiation method. The model parameters used in the simulations are listed in Table 4.1.

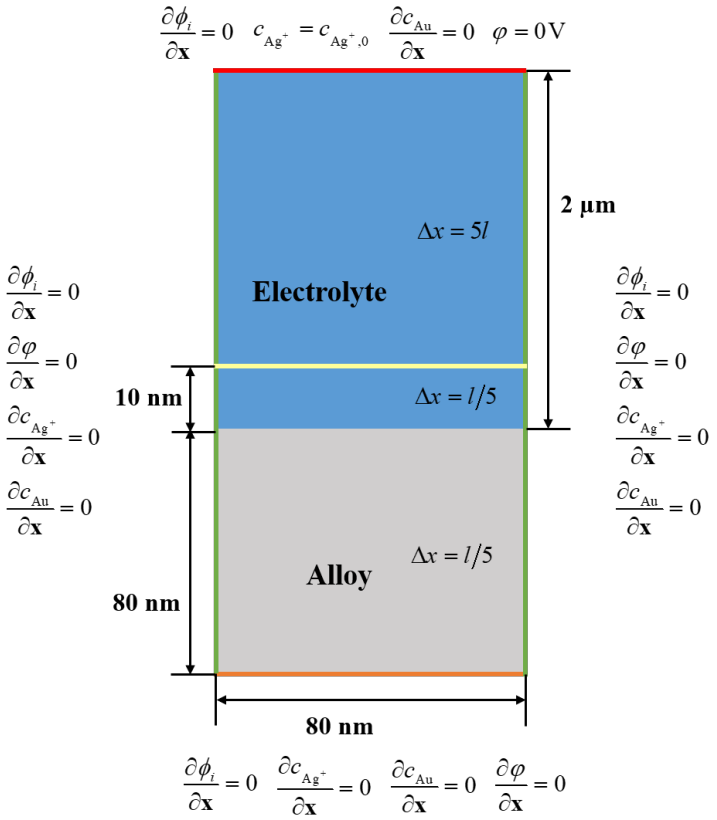

Figure 4.2 Schematic representation of simulation geometry and boundary conditions.

Table 4-1 Parameters used in chapter 4

	Parameter	Value
Interfacial energy density	σ (J/m^2)	1
Interfacial thickness	l (nm)	2
Thermodynamic constant	α (J/m^3)	-6.56×10^9

Free-energy density curvature	A (J/m^3)	10×10^9
Numerical constant	a	2.94 [54]
Normalized equilibrium concentration of Au in ϕ_1	$c^1_{\mathrm{Au,e}}$	$c_{\mathrm{Au,0}}$
Normalized equilibrium concentration of Au in ϕ_2	$c^2_{\mathrm{Au,e}}$	1
Normalized equilibrium concentration of Au in ϕ_3	$c^3_{\mathrm{Au,e}}$	0
Saturation concentration of Ag^+ in ϕ_3	$C^{\mathrm{sat}}_{\mathrm{Ag^+}}$ (mol/L)	11.67 [91]
Electrochemical reaction kinetic parameter	κ (mol/m^3/s)	2×10^{-5}
Fluctuation intensity	ζ_0	1 [87]
Nucleation prefactor	I_0	1×10^5
Interfacial mobility	L_{12} (m^3·s/kg)	1×10^{-7}

Interfacial mobility	L_{32} ($m^3 \cdot s/kg$)	1×10^{-7}
Bulk diffusion coefficient of Au in ϕ_1	D_{Au}^{1} (m^2/s)	10^{-25}
Bulk diffusion coefficient of Au in ϕ_2	D_{Au}^{2} (m^2/s)	10^{-25}
Bulk diffusion coefficient of Au in ϕ_3	D_{Au}^{3} (m^2/s)	0
Surface diffusion coefficient of Au at the ϕ_1/ϕ_3 interface	D_{Au}^{13} (m^2/s)	10^{-14} [12], [32]
Surface diffusion coefficient of Au at the ϕ_2/ϕ_3 interface	D_{Au}^{23} (m^2/s)	10^{-18} [74], [75]
Diffusion coefficient of Ag^+ in ϕ_3	D_{Ag+} (m^2/s)	10^{-9}
Electric conductivities of ϕ_3	ψ (S/m)	1
Charge-transfer coefficient	ρ	0.7
Ideal gas constant	R (J/mol/K)	8.314
Absolute temperature	T (K)	298

4.4 RESULTS AND DISCUSSION

4.4.1 Microstructure evolution

Our first focus is to investigate the evolution of typical porous structures and the rate-limiting step during the electrochemical dealloying of Ag–Au alloy in 0.1 M $HClO_4$ solution at 25°C. Fig. 4.3 shows the distributions and evolutions of the phase-field variables for $Ag_{0.7}Au_{0.3}$ dealloyed at φ_M = 1.3 V. In Fig. 4.3(a), $\phi_1 + 2\phi_2 + 3\phi_3$ represents two-dimensional (2-D) snapshots of three phases, where the advance of the dealloying front that distinguishes the dealloyed structure from the starting alloy phase (ϕ_1, red) is discernible, and homogeneous and interpenetrating solid ligament–liquid channels (ϕ_3, blue) nanoporous structures are generated. It is readily seen from Fig. 4.3(a) that Au phase nuclei (ϕ_2, green) originate inside the ϕ_1/ϕ_3 interface and form the initial surface of rod-like ligaments. Then, the perimeters of these ligaments are increased by the continuous release of Au atoms as the Ag atoms of the next layer are stripped. Therefore, some ligaments exhibit core-shell structures, in which the unattacked alloy phase is encapsulated by an Au phase; this results from synergy between the interfacial dissolution of Ag and the interfacial diffusion of Au. The length scale of pores is ~10 nm, which is consistent with the experimental observations. Moreover, it has been observed in many experiments that due to the advancement of the dealloying front into the bulk alloy, Ag exposure and consequent dissolution occurs if the Au surface layer is not dense enough to completely cover the alloy, and thus, some ligaments undergo secondary dealloying [70]. The coarsening

of ligaments also occurs spontaneously, driven by capillary forces, as these decrease the interfacial energy. Ultimately, if insufficient Au atoms remain to passivate the alloy, some ligaments are undercut from the alloy.

Fig. 4.3(b) shows that c_{Au} is a good indicator of phase distributions during the dealloying process, as it maintains the initial concentration in ϕ_1, approaches 1 in ϕ_2, and is equal to 0 in ϕ_3. Because the ligament walls block the access of ions, the concentration of Ag^+ is higher near the dealloying front, but much lower than the saturation concentration of Ag^+ in the electrolyte. It has been experimentally determined that pitting corrosion of stainless steel is controlled by the diffusion of dissolved species in the electrolyte at a high applied potential [54]. It has also been shown that during the liquid-metal thermal dealloying of Ta-Ti in a Cu melt, the evolution of dealloying depth follows $t^{1/2}$ behavior [20]. However, during electrochemical dealloying, the interface process is slower than the diffusion of dissolved metal cations in the electrolyte, and no accumulation of ions is observed. This indicates that electrochemical dealloying up to this depth is dominated by interfacial processes, such as Ag dissolution and Au diffusion, rather than long-range diffusive processes. As we assume that the evolution of topological patterns is controlled by interface process, rather than by ionic transport, the evolution of ions in the electrolyte is ignored in the following sections.

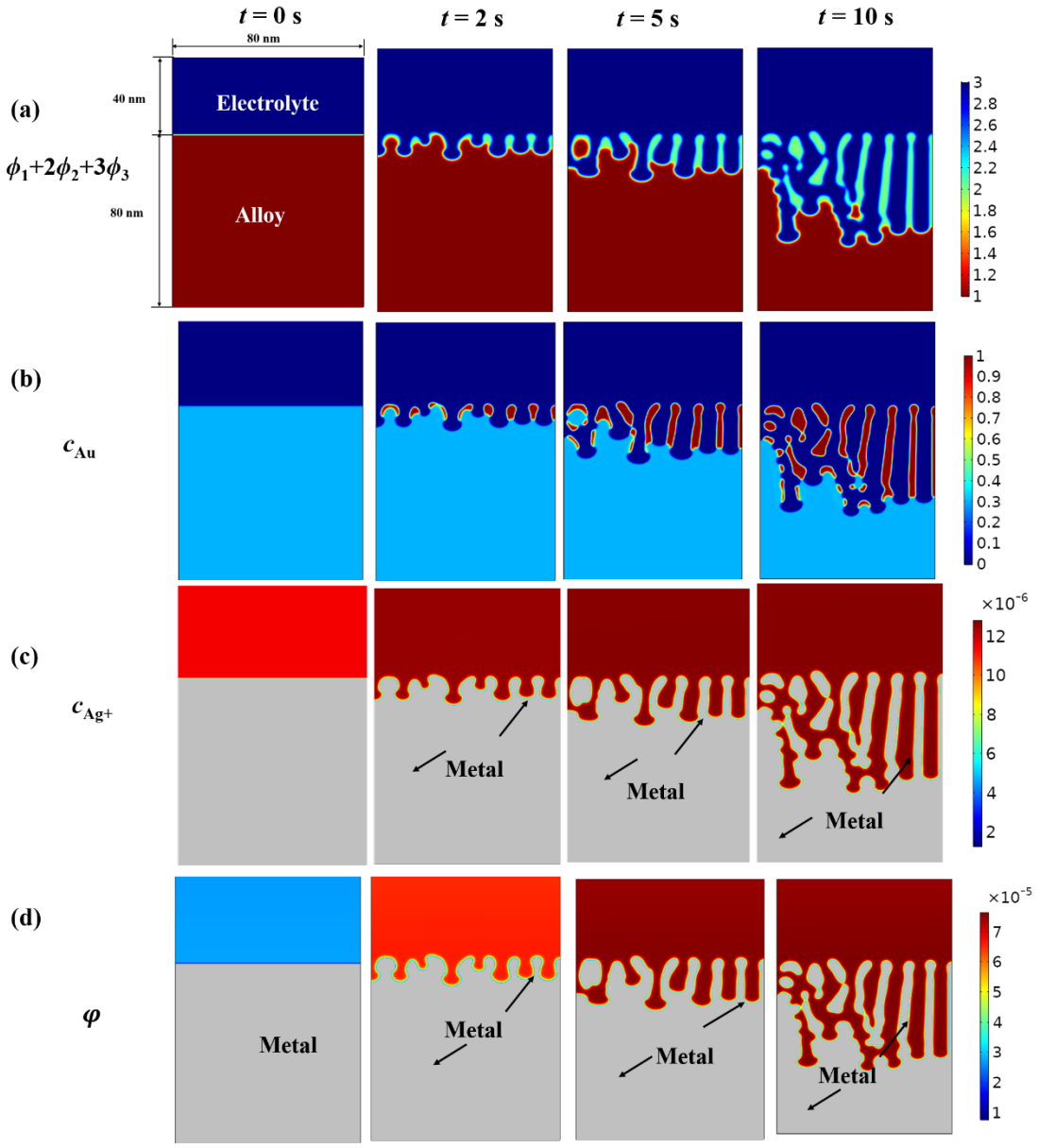

Figure 4.3 Phase-field variable distributions and evolution during the electrochemical dealloying of $Ag_{0.7}Au_{0.3}$ in 0.1 M $HClO_4$ solution with φ_M = 1.3V: (a): $\phi_1 + 2\phi_2 + 3\phi_3$; (b): cAu; (c): cAg$^+$/(mol/L); (d): φ/V.

4.4.2 Effect of electropotential

It is widely recognized that applied potential (φ_M) and precursor composition ($c_{Ag,0}$) are the main controllable factors that can be used to tune the morphology and microstructure of nanoporous gold (NPG). Fig. 4.4(a)–(d) shows simulated microstructures of as-dealloyed samples obtained from the electrochemical dealloying of $Ag_{0.7}Au_{0.3}$ subjected to various φ_M. As φ_M increases, there is a considerable decrease in the dealloying duration, as shown in Fig. 4.4. Moreover, the lower the value of φ_M, the larger are the ligaments, the lower is the porosity, and the more the parent alloy is encapsulated in ϕ_2, which is attributable to the decrease in the dissolution rate of Ag. Fig. 4.5(a) shows the evolution of the dealloying fronts of these as-dealloyed samples, which indicates that the dealloying velocity is effectively constant with time and increases with electropotential. The ability of this model to predict 2-D dealloying kinetics can be validated by comparing the simulated dealloying front propagation velocity (v) with the experimental current density (i), where Faraday's law states that

$$i = nFJ/M \,, \tag{11}$$

where M is the molar mass of Ag, and J is the corrosion flux of Ag into the electrolyte per unit time and per unit area, which is expressed as [62]:

$$J = \rho_{Ag} v\left(V_{Ag\text{-}Alloy} - V_{Ag\text{-}NPG}\right) \tag{12}$$

where ρ_{Ag} is the density of Ag, and $V_{Ag\text{-}Alloy}$ and $V_{Ag\text{-}NPG}$ are the volume fractions of Ag in the alloy and the residual Ag in the dealloyed nanoporous structure, respectively. $V_{Ag\text{-}NPG}$ can be determined by evaluating the integral of ϕ_1 over the dealloyed region. It can be seen from Fig.

5(b) that the simulation yields current densities that are in good agreement with experimental measurements [94].

There is an electropotential threshold (E_c) for electrochemical dealloying that corresponds to the corrosion potential of pure metal, and below this threshold, sustained porous structure evolution (rapid dealloying) develops into surface dealloying (passive dealloying). Given the difference between the potential sweep rate in electrochemical experiments and the blurry slope-transition zone of polarization data, it has been determined by extrapolating the polarization curve, fixed current, and steady-state current method that E_c ranges from 0.99 to 1.22 V for $Ag_{0.7}Au_{0.3}$ [94], [95]. The slow corrosion of Ag at φ_M = 1.05 V means that released Au adatoms rapidly aggregate to form initial nuclei, and the perimeter of these passivated surfaces gradually expands. Eventually (see Fig. 4.4(a)), the surface diffusion of Au outweighs the dissolution of Ag, leading to shallow surface dealloying and the formation of a dense Au surface layer. Therefore, PF model could be a convenient tool for defining the threshold E_c, by determining the dealloying velocity and observing the morphological change of the surface of the starting alloy during the dealloying process [96].

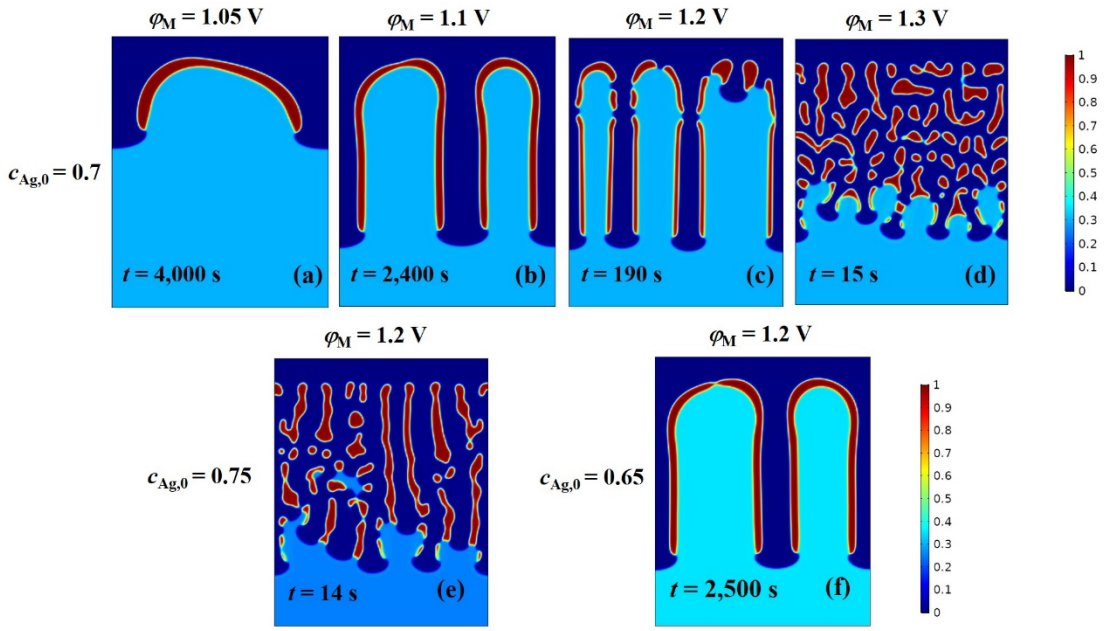

Figure 4.4 The microstructures of NPG obtained through the electrochemical dealloying of (a)–(d) $Ag_{0.7}Au_{0.3}$, with φ_M = 1.05, 1.1, 1.2, or 1.3 V; (e) $Ag_{0.75}Au_{0.25}$, with φ_M = 1.2 V; and (f) $Ag_{0.65}Au_{0.35}$, with φ_M = 1.2 V.

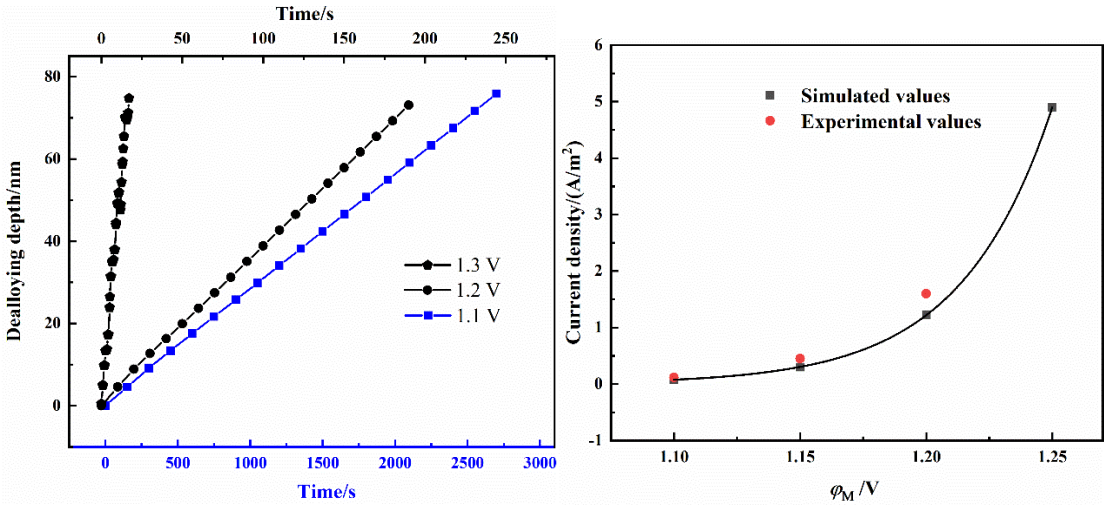

(a) (b)

Figure 4.5 (a) Evolution of the dealloying front of $Ag_{0.7}Au_{0.3}$, with φ_M = 1.1, 1.2, or 1.3 V; (b) relationship between corrosion current density and electropotential during the electrochemical dealloying of $Ag_{0.7}Au_{0.3}$ [94].

4.4.3 Effect of alloy composition

φ_M = 1.2 V is chosen to investigate the effect of the relative content of components in the parent alloy on the microstructure of the obtained NPG, as shown in Fig. 4.4. The decrease of $c_{Ag,0}$ in the precursor should have a similar effect as the decrease of φ_M. Indeed, it is found that the duration required for the same dealloying depth increases with decreasing $c_{Ag,0}$. The size of the ligaments and encapsulated parent alloy also increase with decreasing $c_{Ag,0}$.

To illuminate the internal structure of NPG, the model is used to simulate the most intricate and random 3-D porous morphology during dealloying process. Fig. 4.6 shows an example of 3-D microstructure evolution through etching $Ag_{0.7}Au_{0.3}$ in a 0.1 M $HClO_4$ at an applied potential of 1.3V. The precursor, porous clusters, and electrolyte are represented in transparent red, gray, and blue, respectively. To better visualize the complex porous morphology, the electrolyte phase is hidden in the second column, and the iso-surfaces of $c_{Au} = 0.5$ and $\phi_1 = 0.5$ are extracted in the third column. After t = 0.6 s, the dealloying interface undergoes a shallow retreat, resulting in the formation of some pits linked by self-assembled metallic clusters. As the continuous interface dissolution of Ag and diffusion of Au contribute to the growth of highly bifurcated pores and metallic ligaments, the bicontinuous porous morphology with an irregular

shape extends in 3-D. The length scales of nanopore channels/ligaments are in the range of 10 nm, which is similar to the characteristic length in 2-D morphology. Accordingly, this study proves the reliability of our MPF model in revealing complex 3-D geometry.

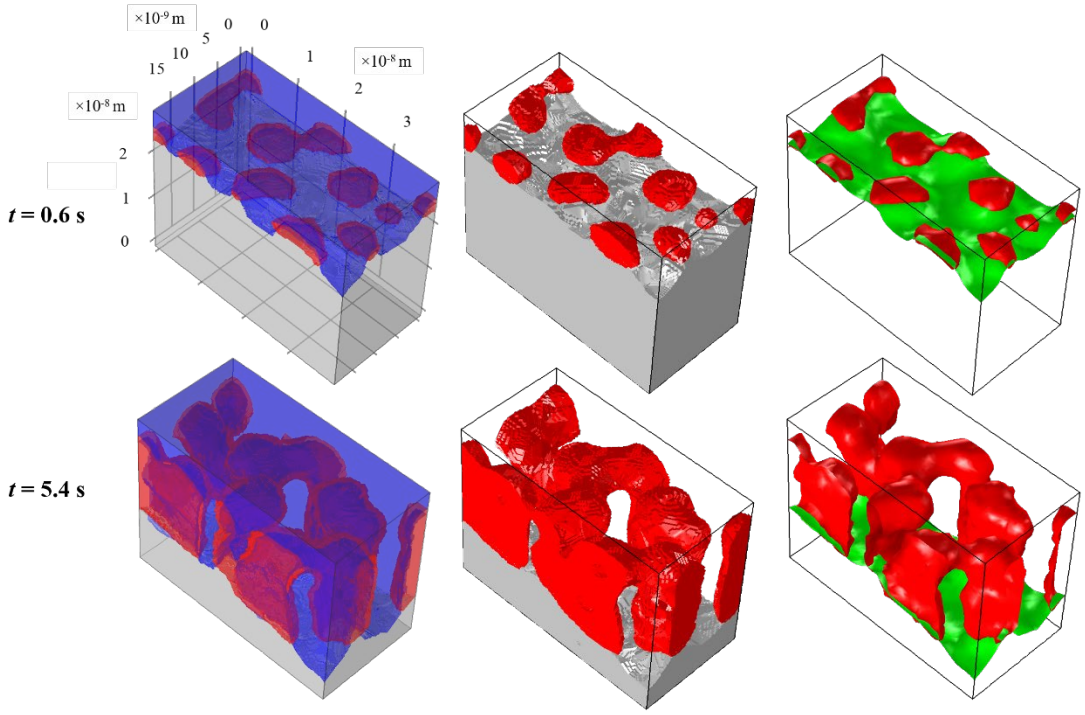

Figure 4.6 3-D morphology evolution of NPG during the dealloying of $Ag_{0.7}Au_{0.3}$ in 0.1 M $HClO_4$ with φ_M = 1.3 V: alloy, porous ligament, and electrolyte phases are represented in grey, red, and blue respectively in the first column; the electrolyte phase is hidden in the second column; in the third column, iso-value surfaces of ϕ_1 = 0.5 and c_{Au} = 0.5 are shown in green and red surface to demarcate the dealloying front and porous ligament, respectively.

Chapter 5 MPF MODEL FOR THE DEALLOYING OF ALLOYS WITH COMPLEX STRUCTURES

5.1 INTRODUCTION

Typically, most dealloying-produced porous metals were fabricated from a homogenous binary solid solution with a simple structure, such as Au-Ag, Cu-Au, or Cu-Pt. Numerous attempts have been made to tailor the pore sizes of these porous products featuring a single characteristic length scale. The coarse pore channels can facilitate rapid transport pathways for mass accessibility, while fine pores can offer large specific surface areas for functionalization. Motivated by the specific applications of porous metals, researchers have recently focused on developing porous architecture with multimodal pore distributions. Hence, a structural hierarchy emerged to address this issue, imparting low mass density, multifunctionalization, optimized activity, and enhanced mechanical properties to porous metals. For instance, in microfluidic sensor applications, a nested porous network material with two characteristic length scales is desirable to achieve a fast-response performance and high sensitivity. In catalysis, the exceptional catalytic performances of hierarchical porous metals benefit from at least two levels of pore sizes, especially small channels for high surface area and large channels for reactant accessibility. The hierarchical NPM structures are also promising in actuating, motoring, and energy conversion and storage, displaying improved performances compared to common single porous structures.

Various strategies have been reported to synthesize monometallic or multimetallic porous structures with multiscale pore distributions. A primary technical route is the precursor design. Based on the chemical property differences of different phases, multi-phase alloys comprising one solid solution phase and one or two intermetallic phases allow the creation of micro-nano hierarchical porous structures. Researchers also developed an elevated temperature dealloying method to fabricate hierarchical nanoporous copper structures, which exhibited submicron-scale pores at the outer layer coupled with nanoscale pores at the inner layer. A multi-step strategy including dealloying, annealing, and post-dealloying has been demonstrated to be an effective method of transforming monoporous into multiporous structures.

Dealloying not only allows the creation of mono and multi-element metals with hierarchical network structures in flexible product forms but also offers tunability of the characteristic length scale of pores and structure compositions. Along with the expansion of new applications of porous materials and further scientific research, it is expected that dealloying will potentially become a generic method in enabling the design and development of more sophisticated hierarchical porous metals. Recent progress using the PF model to simulate the dealloying process will help provide a comprehensive roadmap for developing specific hierarchical porous metal structures and optimizing the dealloying route and subsequent nanoporous morphology and composition for specific applications.

5.2 METHOD

5.2.1 Investigated system

This section describes the design of a precursor A-B comprising multiple phases with different compositions to achieve diverse porous structures with different morphologies and compositions. When the precursor is immersed in the electrolyte with or without applied electropotential, due to the different chemical nature, the LN metal element A in the corrosive phases (A_mB_n) firstly dissolves into the solution, while the MN metal element B undergoes a self-organization process to obtain nanoporous B structures with randomly distributed pores. Other phases in the precursor may remain passive and non-reactive with the electrolyte. Thus, a different morphology is generated depending on the constituents and distribution of phases in the precursor. The electrochemical reaction involved is given by Eq. (5.1):

$$\mathrm{A} \rightarrow \mathrm{A}^{n+} + n\mathrm{e}^{-} \tag{5.1}$$

5.2.2 Multi-phase-field model

The order parameter field ϕ_i (i = pre, por, or ele) is introduced to describe the volume fractions of the three different local phases in the dealloying process (ϕ_{pre}: the precursor phase; ϕ_{por}: the porous phase; ϕ_{ele}: the electrolyte phase). The ϕ_i varies smoothly from 1 to 0 across the interfaces and satisfies the normalization condition $\sum \phi_i = 1$. C_N (N = A, B, or C^{k+}) is an independent conserved field variable representing metal components in the alloy phase or dissolved ions in the electrolyte phase. The morphology evolution during dealloying is driven by minimizing the total system's Gibbs free energy, formulated by Eq. (5.2).

$$G = \int_V f_{\text{chem}}(\phi_i, c_N) + f_{\text{grad}}\left(\nabla\phi_i\right) + f_{\text{elec}}(\varphi) dV \,, \tag{5.2}$$

where $c_N = C_N/C_{\text{ref}}$ is the dimensionless concentration field (C_{ref} is the reference concentration), φ describes the electropotential field, and f_{chem}, f_{grad}, and f_{elec} are the chemical, interfacial, and electrostatic potential parts of the free energy, respectively. Here, $f_{\text{grad}} = \varepsilon/2 \sum_i \left(\nabla\phi_i\right)^2$, where ε is the gradient energy coefficient and is expressed as $\varepsilon = \frac{\sigma l}{4\sqrt{2}a}$, where a, l, and σ are the numerical constant, interface thickness, and surface energy; $f_{\text{elec}} = \sum_k C_k n_k F \varphi$, where n_k is the charge number of ion species in the electrolyte, and F is the Faraday constant.

Applying the free energy functional derived in Chapter 4, the bulk chemical free energy is expressed by Eq. (5.3):

$$f_{\text{chem}} = \sum_i W \phi_i^2 \left(1-\phi_i\right)^2 + C_{\text{ref}} \sum c_k \left(\mu_k^{\Theta} + RT \ln c_k\right) + \sum_i h_i f_{\text{B}}^i + \alpha c_{\text{A}} \left(1 - c_{\text{A}}\right), \tag{5.3}$$

where the first term is the obstacle potential between phases. Furthermore, W determines the potential height, expressed as $W = \frac{\sqrt{2}a\sigma}{4l}$. The second term in Eq. (5.3) describes the free energy of the electrolyte phase, where μ_k^{Θ}, R, and T are the standard chemical potential of the ion species, gas constant, and absolute temperature. The third term corresponds to the free energy of noble element B, which is expressed as the weighted sum of the free energy in the individual phases, where h_i is an interpolation function ($h_i = \phi_i^2 \Big/ \sum_j \phi_j^{\,2}$) and f_{B}^i is the free energy of element B in phase i; $f_{\text{B}}^i = f^{'}\left(c_{\text{B}}^i - c_{\text{B,e}}^i\right)^2$, where $f^{'}$ is the free energy curvature,

and c_{B}^{i} and $c_{\mathrm{B,e}}^{i}$ are the concentration and equilibrium concentration of B in phase *i*. The relationship between c_{B}^{i} at the interfaces is determined by assuming equal diffusion potentials, as proposed in the KKS model shown in Eq. (5.4). The last term in Eq. (5.3) describes the enthalpy of mixing of solid solution phases in the precursor, where α is a thermodynamic constant.

$$c_{\mathrm{B}}=\sum_{i} h_i c_{\mathrm{B}}^{i}, \frac{\partial f_{\mathrm{B}}^{i}}{\partial c_{\mathrm{B}}^{i}}=\frac{\partial f_{\mathrm{B}}^{j}}{\partial c_{\mathrm{B}}^{j}}=\mu_{\mathrm{B}} \tag{5.4}$$

A nonlinear PF model was first proposed by Chen et al. [56], where the phase transformation from the electrolyte phase to the metal phase follows the electrochemical reaction kinetics. In this work, the interface evolution between the precursor and electrolyte phase is driven by the dissolution of the LN metal element in the precursor. Thus, the corrosion reaction kinetics accounts for the morphology evolution of the $\phi_{\mathrm{pre}}/\phi_{\mathrm{ele}}$ interface. The metal corrosion reaction follows the Butler-Volmer electrochemical reaction kinetics:

$$r=k_0\left[\exp\left(\ln a_1+\frac{(1-\rho)\Delta\mu}{RT}\right)-\exp\left(\ln a_2+\frac{-\rho\Delta\mu}{RT}\right)\right], \tag{5.5}$$

where k_0 is the reaction constant, ρ is the charge transfer coefficient, a_1 and a_2 are the activities of the reactants and products, and $\Delta\mu$ is the activation overpotential. According to the definition in ref [89], $a_{*}=\mathrm{e}\exp\left(\frac{1}{RT}\frac{\partial(f_{\mathrm{chem}}+f_{\mathrm{grad}}-c_{*}\mu_{*}^{\Theta})}{\partial C_{*}}\right)$, where $*$ describes the reactants and products.

As the evolution of phase variable ϕ_{pre} corresponds to the transformation between the precursor

and electrolyte phase, following the derivation process detailed in Appendix A, the governing evolution of ϕ_{pre} is expressed by Eq. 5.6 (a–e).

$$\frac{\partial \phi_{\text{pre}}}{\partial t} = -L_M \times \mu_{\text{int}}^{M} - \lambda_M \kappa_M \left[\exp\left(\frac{\mu_M + (1-\rho)\Lambda}{RT} \right) - c_{\text{A}^{n+}} \exp\left(\frac{-\rho\Lambda}{RT} \right) \right], \tag{5.6a}$$

$$\mu_{\text{int}}^{M} = \sum_{i, i \neq M} \left(\frac{\delta G}{\partial \phi_M} - \frac{\delta G}{\partial \phi_i} \right), \tag{5.6b}$$

$$\lambda_M = 4 h_M h_{\text{ele}}, \tag{5.6c}$$

$$\mu_M = \alpha_M \left(1 - 2c_{\text{A},0}\right), \tag{5.6d}$$

and

$$\Lambda = nF(\varphi_{\text{ap}} - \varphi) - \mu_{\text{A}^{n+}}^{\Theta} \tag{5.6e}$$

In Eq. (5.6a), the superscript and subscript M represent phase M in the precursor phase, L_M and κ_M are PF mobility parameters for phase M, and μ_{int}^{M} is the driving force from the interface energy. Here, λ_M is multiplied by the second term on the right side in Eq. (5.6a) to indicate that the corrosion reaction only occurs at the precursor/electrolyte interface, and μ_M describes the effect of the phase composition of phase M, where $c_{\text{A},0}$ is the concentration of A in the solid solution phase. In Eq. (5.6e), Λ represents the driving force from the applied electropotential, where φ_{ap} is the applied electropotential.

The evolution of the porous phase is then governed by the Allen-Cahn equation:

$$\frac{\partial \phi_{\mathrm{por}}}{\partial t}=-\frac{1}{3}\sum_{i\neq \mathrm{por}}\left(L\left(\frac{\delta G}{\delta \phi_{\mathrm{por}}}-\frac{\delta G}{\delta \phi_i}\right)\right)+\zeta_{\phi_{\mathrm{por}}}, \tag{5.7a}$$

with

$$\zeta_{\phi_{\mathrm{por}}}=r\zeta_0 16\phi_1^2\left(1-\phi_1\right)^2 I_0 k_B T\,\Delta\Omega^2/\sigma^3 \tag{5.7b}$$

In Eq. (5.7a), L is the PF mobility parameter. A noise term $\zeta_{\phi_{\mathrm{por}}}$ is constructed to represent the thermal instability of the system and heterogenous nucleation when the LN element is dissolved, followed by the release of the MN element from the solid-liquid phase interface. Eq. (5.7b) follows the classical nucleation theory, which indicates that the formation rate of clusters varies directly with the variation of the chemical free energy ($\Delta\Omega$) and inversely with surface energy, where r is a random number, ζ_0 is the fluctuation intensity, and I_0 is the nucleation prefactor.

The porous pattern transformation is governed by mass transport. The evolution of B is given by the Cahn-Hilliard equation, which incorporates the bulk and surface diffusion of MN element B, the diffusion coefficient of which varies from one phase to another, expressed as

$$\frac{\partial c_{\mathrm{B}}}{\partial t}=\nabla M_{\mathrm{B}}\nabla\frac{\delta F}{\delta c_{\mathrm{B}}}=\nabla D_{\mathrm{B}}\sum_i h_i\nabla c_{\mathrm{B}}^i, \tag{5.8a}$$

with

$$M_{\mathrm{B}}=D_{\mathrm{B}}\Big/\left(\delta^2 G/\delta {c_{\mathrm{B}}}^2\right), \tag{5.8b}$$

and

$$D_{\mathrm{B}} = \sum_i h_i D_{\mathrm{B}}^i + \lambda_M D_{\mathrm{B}}^M + \lambda_{\mathrm{por}} D_{\mathrm{B}}^{\mathrm{por}}, \tag{5.8c}$$

In Eqs 5.8 (a–c), M_{B} is the diffusion mobility, and D_{B}^i, D_{B}^M, and $D_{\mathrm{B}}^{\mathrm{por}}$ are the diffusion coefficients in bulk phases, the diffusion coefficient at the $\phi_M/\phi_{\mathrm{ele}}$ and $\phi_{\mathrm{por}}/\phi_{\mathrm{ele}}$ interface. In Eq. (5.8c), h_i, λ_M, and λ_{por} are used to locate the diffusion of B.

Then, the evolution of ion species in the electrolyte follows the Nernst-Planck diffusion equation:

$$\frac{\partial c_k}{\partial t} = \nabla\left(h_{\mathrm{ele}} D_k \nabla c_k + \frac{h_{\mathrm{ele}} D_k c_k F}{RT} \nabla \varphi \right) - c_{\mathrm{A},0} \frac{\partial \phi_{\mathrm{pre}}}{\partial t}, \tag{5.9}$$

where D_k is the diffusion coefficient of ion species in the electrolyte, and the final term is the source term corresponding to the production from the corrosion reaction. In addition to phase-fields and concentration field evolution, the distribution of the electropotential is given by Eq. (5.10):

$$\nabla\left(\sum_i h_i \psi_i \nabla \varphi \right) = F C_{\mathrm{ref}} \frac{\partial \phi_{\mathrm{pre}}}{\partial t}, \tag{5.10}$$

where the electrical conductivity at the interfaces is treated as a mixture of the electrical conductivity for each phase ($\psi = \sum_i \psi_i h_i$), and the right-hand side of Eq. (5.10) refers to the current originating from the electrochemical reaction.

5.3 NUMERICAL IMPLEMENTATION

All calculations in this work were performed on COMSOL Multiphysics 5.4 using a finite element approach. The simulations were performed on a two-dimensional domain with constant grid spacing, $\Delta x = \Delta y = l/5$, and the time step was automatically refined. The geometry and initial and boundary conditions are given in Fig. 5.1. As part of the optimization procedure, we used $\phi_{ele} = 1 - \phi_{pre} - \phi_{por}$ to identify and calculate the electrolyte phase.

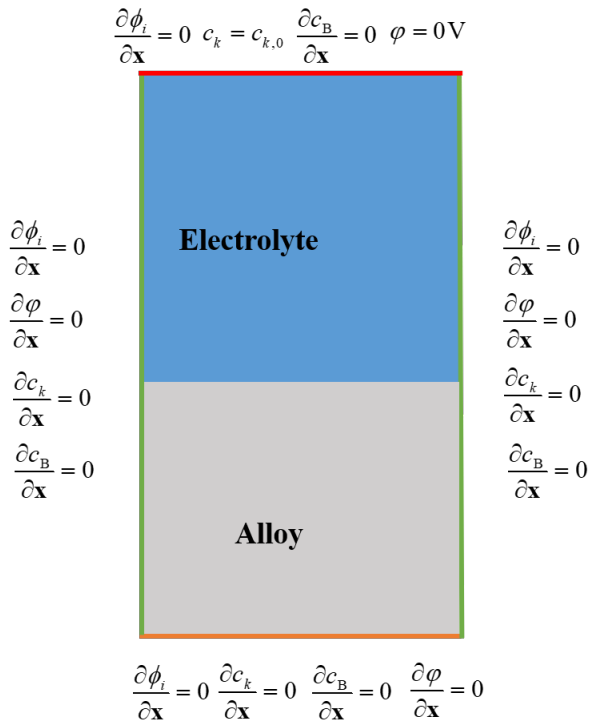

Figure 5.1 The geometry and boundary values of the investigated system for the numerical implementation.

5.4 RESULTS AND DISCUSSION

5.4.1 NPMs with unimodal pore size

5.4.1.1 Effect of inert phase pre-existing in precursor

Researchers initially focused on fabricating homogenous porous metal structures with unimodal pore sizes by dealloying single-phase precursors. By combining mechanical tests and atomic simulations, it was reported that dealloying-produced monoporous metals exhibited high mechanical performances, and the decrease in pore size could improve the strength of dealloyed materials [97]–[99]. In addition to tailoring the pore size, surface modifications of ligaments (such as the surface coating on the ligaments) were also effective for improving the strength and tensile performance of NPMs while the specific pore size remained unchanged [97]. It was also found that the dealloying of a two-phase system resulted in a porous composite structure rather than a homogeneous structure, where the inert second phase acted as the strengthening phase. Wang et al. [100] fabricated nanoporous Pd composites through the chemical dealloying of an Al-Pd alloy comprising two phases (Al_3Pd and Al_3Pd_2). The resultant nanoporous Pd composites comprised a nanoporous Pd matrix dealloyed from the Al_3Pd phase and undealloyed Al_3Pd_2 embeddings, and they possessed high electrocatalytic activities.

Here, we modeled the chemical dealloying process of a binary alloy with a second phase. We added an inert phase with random shapes into the $Ag_{0.7}Au_{0.3}$ matrix for simplicity. To ensure the stability of the inert phase during dealloying, we applied the Dirichlet boundary condition ($\phi_{pre} = 1$) to the inert phase. Fig. 5.2 shows that the dealloyed structure comprises a porous matrix and intact embeddings, which inherit the same distributions in the precursor. During the dealloying process, the second phase is stable against the chemical attack of the electrolyte

solution and can be conserved completely, while the porous structure results from the dealloying of the matrix. Ultimately, these two dealloying and undealloying processes result in porous metal composites with unimodal pore sizes. Although the inert phase in the precursor leads to a decrease in the surface area and porosity compared to the homogenous porous structure, the catalytic performance and other functional performances can be improved by adjusting the length scale of the porous matrix. The ligament/pore size of metal composites can be further modulated by controlling the dealloying conditions, as described in Chapters 3 and 4. Moreover, the compact embeddings in the porous composites are a promising reinforcement phase if the second phase possesses high strength and the connectivity between the second phase and the matrix is strong. Thus, these novel monoporous composites can serve as model materials to optimize the physical, mechanical, and other properties of porous materials, which will find potential applications in fields that benefit from excellent mechanical properties and high surface area. Since our model is a multi-phase model, it is easily extended to study composites with more than two phases.

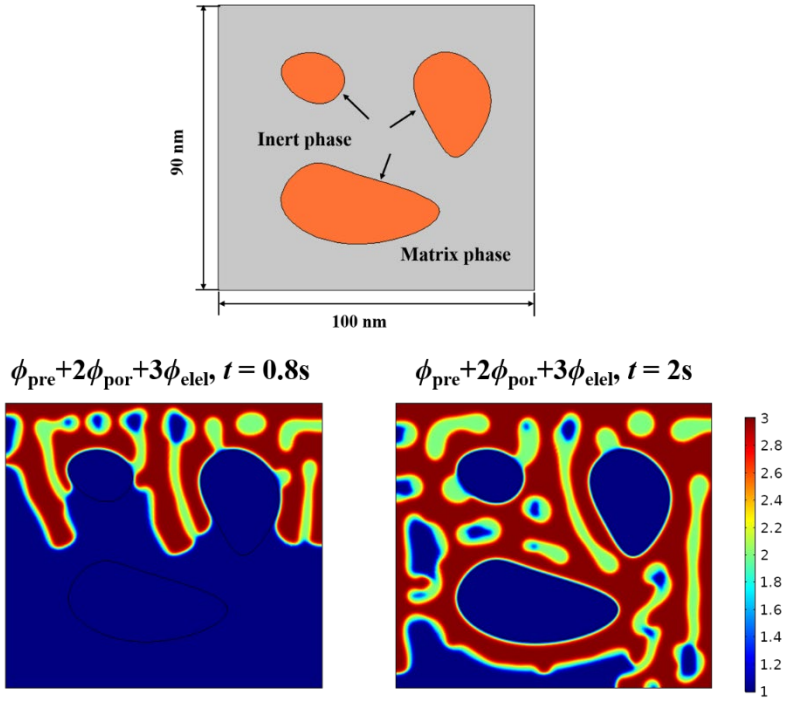

Figure 5.2 The microstructure evolution of NPM composites with unimodal pore

Experiments also showed that pre-existing defects in the precursors, such as voids, grain boundaries, and segregations, affect the rate of dealloying. The active element located at those defective sites with disordered atom arrangements may corrode faster than that at the matrix [44]. To ensure the electrochemical difference between the matrix and defective sites, we assigned a higher activation energy that was four times the reaction activation energy of the matrix to defective sites. Fig. 5.3 shows that the dealloying front is no longer planar, and the etching near defective sites is faster than that in the matrix. Moreover, the size of ligaments close to defective sites is smaller due to the increase in dealloying velocity, as illustrated in the previous section.

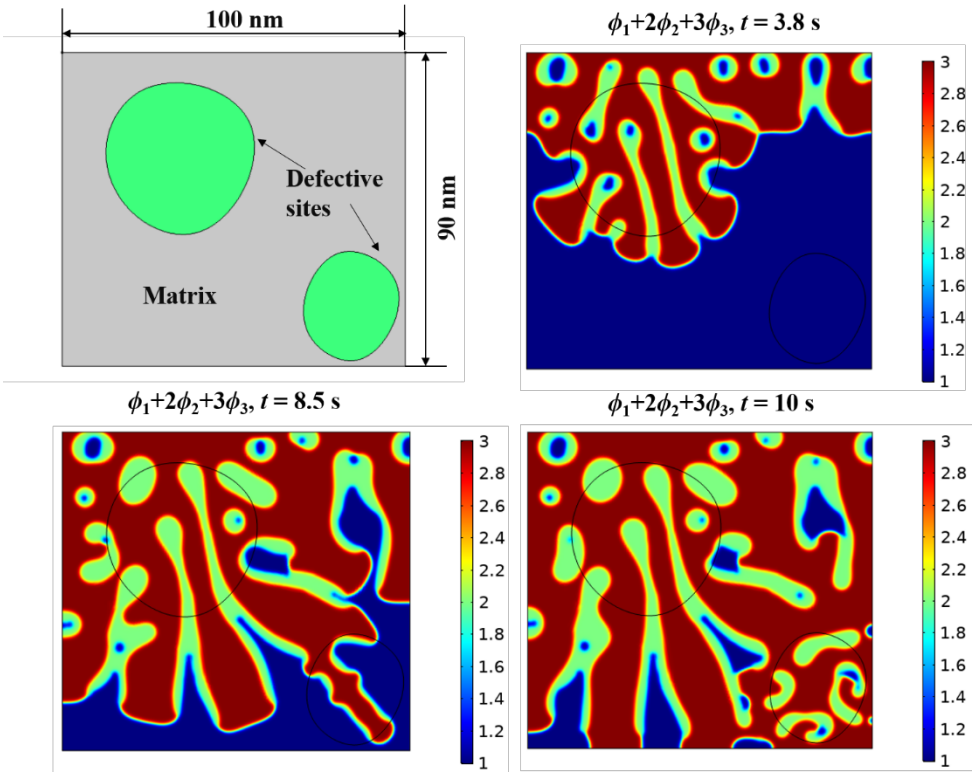

Figure 5.3 Effect of defective sites pre-existing in the precursor on the microstructure evolution during the chemical dealloying process

5.4.2 NPMs with bimodal pore sizes

5.4.2.1 Dealloying of precursor comprising a solid solution and intermetallics

Previously, much attention has focused on fabricating NPMs with unimodal pore size distributions, as ideal nanoporous structures are obtained from single-phase solid solutions or intermetallic compound systems, such as Ag-Au, Al-Au, and Ni-Cu. However, most recent investigations have focused on fabricating hierarchical nanoscale porous metal structures with multiple length scale channel distributions [8]. Particularly, ligament-channel metal structures with large pores (hundreds of nanometers) can facilitate the mass transport or diffusion to

achieve a fast response, whereas NPMs with small pores (tens of nanometers) offer a high specific surface area with numerous active sites to achieve effective adsorption and reactions. Hence, a need exists for nanoscale structures with bimodal channel size distributions to meet the dual demands for sensing, catalysis, and actuating [8], [101].

In addition to allowing precise control of the length scale of porosity, dealloying enables the fabrication of hierarchical porous structures with multimodal pore sizes. Additionally, a precursor alloy design has been more commonly used to develop bimodal nanoscale porous metals. For example, Zhang et al. [102] synthesized nanoporous NPG ribbons with bimodal pore sizes via the rapid solidification and chemical dealloying of Al-Au systems. NPG ribbons comprise large pores (~100 nm) with porous metal walls (the pores of which are ~10 nm) obtained from the dealloying of α-Al and Al_2Au phases, respectively, in a precursor. Liu et al. [78] presented a facile strategy to synthesize asymmetrically patterned nanoporous Cu ribbons by chemical dealloying of $Al_{0.68}Cu_{0.32}$ alloy comprising α-Al and Al_2Cu phases. This section extends our proposed PF model to the fabrication of NPMs with bimodal channel distributions from a binary alloy system comprising solid solution and intermetallic compound phases.

Fig. 5.3 shows that the starting alloy comprises α-Al and Al_2Au phases. In this case, the dealloying of α-Al is simplified as purely Al corrosion, given that the solubility of Au in α-Al is low. Therefore, Eq. (5.3) contains no mixing enthalpy term for the Al-Au system, as the Au concentration in α-Al is low, and Al_2Au is an intermetallic compound. The third term on the right side of Eq. (5.3), which describes the free energy of the MN element (Au), is ignored when

considering α-Al. We used a MPF model to simulate the chemical dealloying of $Al_{0.8}Au_{0.2}$ in a 5 wt% aqueous solution of hydrochloric acid. In the PF model of electrochemical dealloying of Ag-Au alloy, the applied electropotential acts as a driving force of alloy corrosion and follows electrochemical reaction kinetics. We modified the model to capture the chemical dealloying of the dual-phase binary alloy and thereby obtained the following governing kinetic equation of the precursor:

$$\frac{\partial \phi_{\text{pre}}}{\partial t} = -L_M \mu_{\text{int}}^M - \lambda_M \kappa_M \left[\exp\left(\frac{-G_{\text{a}}}{RT} \right) \right] \tag{5.11}$$

Here, G_{a} is the activation energy for the dissolution of the precursor, which is analogous to the driving force Λ in the electrochemical dealloying shown in Eq. (5.6) and varies with the starting phases. Many studies have suggested that the internal stress produced by the quenching process of the precursor, the disparity between the crystal structures of the starting alloy and the NPMs, and the capillary force of NPMs strongly affect the mechanical properties of porous structures, such as their crack formation and strength [44], [84], [103], [104]. We focused on general pattern formation in the homogenous porous structure and ignored the strain energy and volume change for simplicity. As no relevant experimental studies exist on G_{a} or the dissolution rate of Al_2Au, we assumed that the value of G_{a} for α-Al was 5% lower than that for Al_2Au to represent the chemical activity difference between the two phases. The evolution of the porous Au phase during the dealloying of the Al_2Au phase is governed by Eq. (5.7), and the dealloying process is shown in Fig. 6. The dissolution of all α-Al leaves large channels that retain their original

size; thus, this dissolution process is equivalent to excavating α-Al from the precursor. The dealloying of Al_2Au lags far behind the etching of α-Al and generates a monolithic ligament-channel structure with length scales of ~10 nm. The length scale of channel walls in this structure is less than that observed in experiments [102] due to the short coarsening time in this simulation. Ultimately, the dealloyed structure displays a bimodal pore distribution comprising large channels encircling island-shaped porous walls, consistent with the experimental observations [102]. For simplicity, we only considered two Al_2Au grains in this case, leading to the formation of isolated porous walls. However, Al_2Au phases are intertwined in the precursor. This model could predict various bimodal (or multimodal) NPG structures that could be obtained from a different starting alloy or dealloying solution.

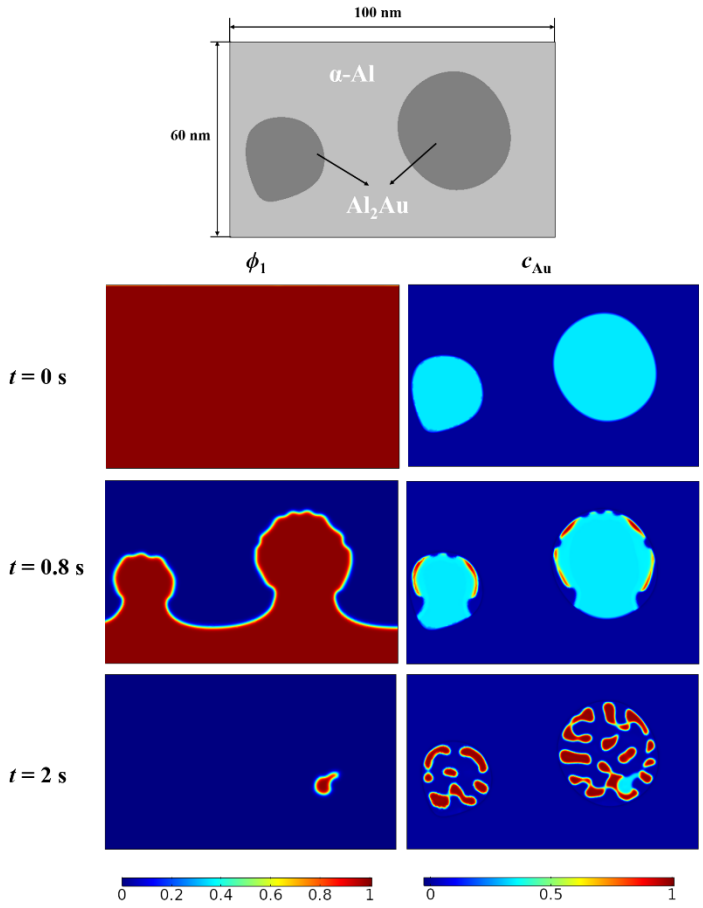

Figure 5.4 Simulated hierarchical evolution of microstructures during the chemical dealloying of $Al_{0.8}Au_{0.2}$ in a 5 wt% aqueous solution of HCl.

5.4.2.2 Dealloying of dual-phase Al–Au alloy comprising intermetallics

Given the high cost of noble metals and the scarcity of alloys comprising solid solution and intermetallic phases, the dealloyable alloy stockpile must be expanded. Much effort has been devoted to exploring suitable precursors. It has been demonstrated that dealloying some multiple-phase binary alloys can yield hierarchical nanoporous composites with different porosities and compositions, which have wide applications in functional materials. For example, it was shown that the chemical dealloying of rapidly solidified $Al_{0.6}Au_{0.4}$ alloy comprising Al_2Au

and AlAu in acid or alkali solution generated NPG composites comprising two types of porous structures with different pore sizes [105]. In other work, Liu et al. [106] investigated the dealloying behavior of a two-phase $Al_{0.6}Cu_{0.4}$ alloy in sodium hydroxide (NaOH) solution, which led to the formation of a unique nanoporous Cu/Al-Cu composite.

Here, we simulated the development of hierarchical NPG from the chemical dealloying of $Al_{0.6}Au_{0.4}$ comprising Al_2Au and AlAu phases in 20 wt% aqueous NaOH solution. In our simulation domain, two Al_2Au grains are isolated by the AlAu phase. As no experimental data exists on the dealloying velocity of single-phase Al_2Au or AlAu, we assumed an activation energy difference (ΔG_a) of 4 kJ/mol between the two phases to represent their different chemical potentials. The relevant parameters can be calibrated for different alloy families. Fig. 5.5 shows that the dealloying of Al_2Au and AlAu proceeds separately and that the dealloying of the former is faster than that of the latter. Ultimately, both phases are fully dealloyed, generating a bicontinuous ligament-pore structure containing large pores (NPG1) surrounding a similar structure containing small pores (NPG2). The proportion of ligament-pore structures in the NPG composite and the length scale of channels can be modulated by controlling the compositions of the starting alloy and dealloying solutions. Based on simulation results, we are confident that this model can reveal the dealloying mechanisms of multi-phase alloys. This is a potential design tool for tailoring the morphologies of hierarchical nanoporous structures.

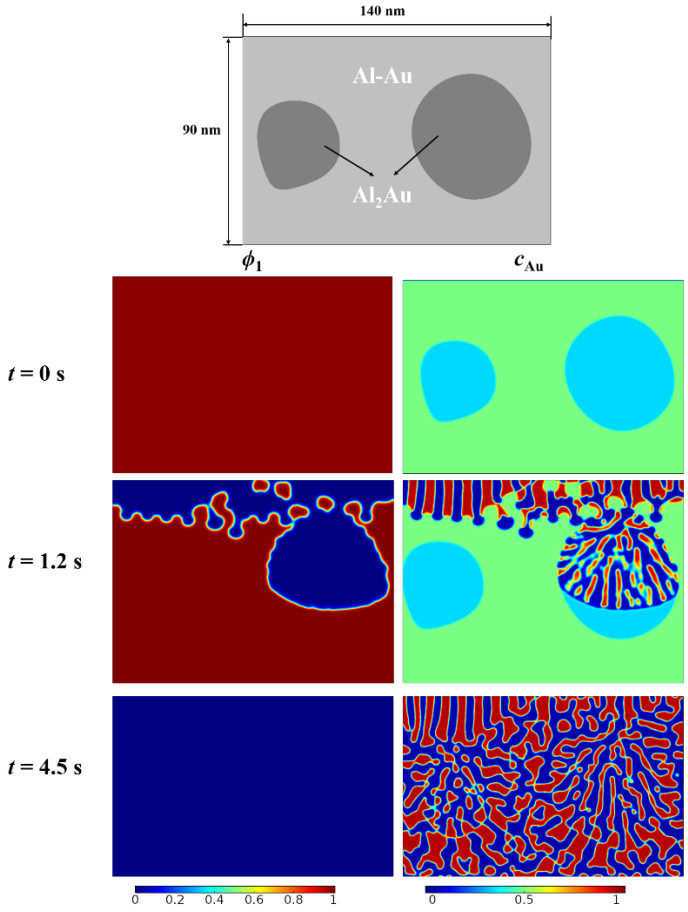

Figure 5.5 Simulated evolution of microstructures during the chemical dealloying of dual-phase Al–Au alloy in a 20 wt.% aqueous solution of NaOH.

5.4.3 NPMs with with a structured hierarchy

Decreasing the solid volume fraction of porous networks has been recognized as beneficial to creating lighter structures. However, it could lead to the deterioration of network connectivity and degradation of stiffness and strength. Researchers reported a two-step dealloying route toward fabricating lightweight and stable porous structures that afford reduced solid fractions and enhanced strength. The dealloying-produced architecture features a hierarchical network where two similar porosities are nested with different length scales, which was realized by the

dealloying of the precursor, deposition of the LN element, annealing to form an alloy, and re-dealloying steps. For example, Zhen et al. [107] reported a strategy for the electrochemical dealloying of Ag-Au involving dealloying, annealing, and re-dealloying steps to generate NPG architectures containing two distinct channel sizes. This section describes how we simulate the re-dealloying of the coarsened nanoporous structures to demonstrate the capability of the model to predict the creation of porous structures with a structural hierarchy. Firstly, we use spinodal decomposition to obtain a bulk compositionally modulated model system with a similar structure to the nested network at the upper hierarchy level. In the spinodal decomposition model, the total free energy was formulated based on a solid ligament-liquid pore binary system:

$$F^{\mathrm{sd}} = \int \left(f(u) + \frac{k_u}{2} (\nabla u)^2 \right) dV \tag{5.12}$$

where u is the volume fraction of the solid phase, $f(u)$ is the local chemical free energy, and k_u is the gradient term coefficient. $f(u)$ is approximated by a double obstacle potential, that is $f(u) = W_u u^2(1-u)^2$, where W_u is the height of the potential barrier. Then the creation of porous model structure is governed by the Cahn-Hilliard equation:

$$\frac{\partial u}{\partial t} = \nabla M_u \nabla \frac{\delta F^{\mathrm{sd}}}{\delta u} \tag{5.13}$$

The gradient energy coefficient and initial composition can be adjusted to generate the model system with different solid ligament fractions and sizes. Take Ag-Au as the model system, we considered $u_0 = 0.5$ to obtain a porous structure with a well-defined pore size of L_1~100 nm

shown in Fig. 5.6(a). The initial composition for the as-dealloyed alloy was set as c_0 = 0.3. Because the nested structures combine porosity on distinctly different length scales, the interface thickness was assumed to be 10 nm to decrease computation cost. Fig. 5.6(b)–(c) shows that the initial pore structure remained intact; while a smaller porous structure with a pore size of L_2 ~10 nm penetrating the porous structure at the upper level after the re-dealloying process in a 0.1 M $HClO_4$. Thus, the hierarchical porous structure is reflected in a nested network with two geometrically similar ligament/pore structures featuring two separated length scales. The length scales of the pores at lower levels can be independently adjusted by controlling the dealloying parameters. The model parameters used in the simulations are listed in Table 5.1.

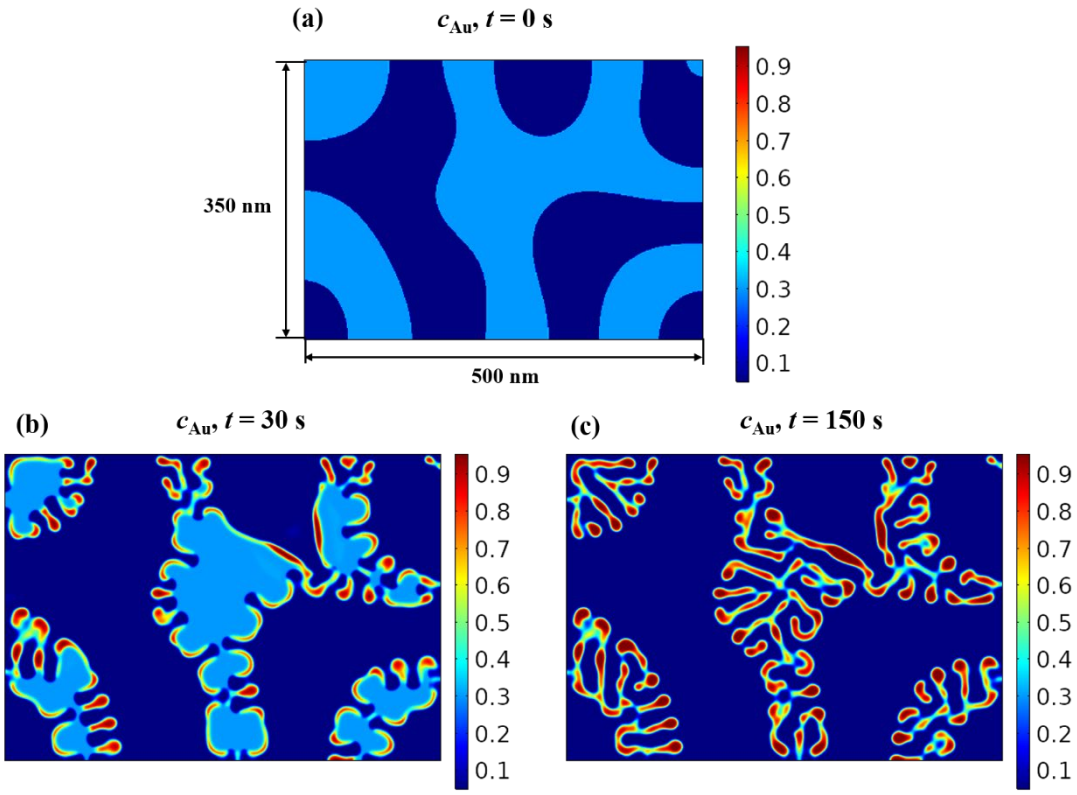

Figure 5.6 Simulated structure evolution of nested porous microstructures: (a) porous structure at the upper level via a spinodal decomposition; (b)–(c) structure evolution during the re-dealloying in a 0.1 M $HClO_4$ with φ_M = 1.2 V.

Table 5-1 Parameters used in chapter 5

	Parameter	Value
Interfacial energy density	σ (J/m^2)	1
Interfacial thickness	l (nm)	2
Free-energy density curvature	A (J/m^3)	10×10^9
Numerical constant	a	2.94 [54]
Normalized equilibrium concentration of Au in ϕ_{pre}	$c_{Au,e}^{pre}$	$c_{Au,0}$
Normalized equilibrium concentration of Au in ϕ_{por}	$c_{Au,e}^{por}$	1

Normalized equilibrium concentration of Au in ϕ_{elec}	$c_{Au,e}^{elec}$	0
Bulk diffusion coefficient of Au in ϕ_{pre}	D_{Au}^{pre} (m^2/s)	10^{-25}
Bulk diffusion coefficient of Au in ϕ_{por}	D_{Au}^{por} (m^2/s)	10^{-25}
Bulk diffusion coefficient of Au in ϕ_{elec}	D_{Au}^{elec} (m^2/s)	0
Surface diffusion coefficient of Au at the ϕ_M/ϕ_{ele} interface	D_{Au}^{M} (m^2/s)	10^{-14} [12], [32]
Surface diffusion coefficient of Au at the ϕ_{por}/ϕ_{ele} interface	D_{Au}^{por} (m^2/s)	10^{-18} [74], [75]
Height of the potential barrier of spinodal decomposition system	W_u (J/m^3)	1.04×10^8
Phase-field mobility	L ($m^3/J/s$)	1×10^7
Gradient term coefficient	k_u (J/m)	6.01×10^{-10}

Mobility in spinodal decomposition system	M_u (m·s/kg)	4.1×10^{-24}
Phase-field mobilitiy parameter	L_M (m·s/kg)	2.2×10^{-9}
Reaction kinetic constant	κ_M (/s)	2.08×10^{-8}
Electric conductivities of ϕ_{elec}	ψ_{elec} (S/m)	1
Charge-transfer coefficient	ρ	0.7
Ideal gas constant	R (J/mol/K)	8.314
Absolute temperature	T (K)	298

Chapter 6 CONCLUSIONS AND SUGGESTIONS FOR FUTURE WORK

6.1 CONCLUSIONS

Dealloying is well-known as a material failure phenomenon in corrosion protection. It has recently attracted growing interest because it has proven highly efficient and controllable in producing interesting NPMs. This necessitates further study of the process to achieve a deeper understanding of the underlying mechanisms. Although tremendous efforts have been devoted to synthesizing various nanostructured materials and characterizing properties, many important fundamental problems are associated with the evolution of topological porosity. Accordingly, the purpose of this research was to explore the corrosion dealloying process. This work aimed to develop and implement computational models based on the PF formulation to approximate the surface morphology, study the details of surface chemistry, and determine the important underlying factors during the dealloying process. Firstly, we presented a formulation of the MPF model for approximating the chemical dealloying process. Secondly, a MPF was developed that could explicitly incorporate the effect of the applied electropotential. Thirdly, we demonstrated the applications of the PF model for simulating hierarchical porous structures.

The important contributions of this work are summarized below:

Firstly, a MPF model was developed to study the evolution mechanisms and kinetics of porous structures during the chemical dealloying of binary alloys. This work developed a MPF model

to demonstrate that a nucleation-growth mechanism can explain the formation of nanoporous structures under chemical attack. The nucleation of the porous phase is controlled by a noise term, scaled by the phase transformation driving force to account for the heterogeneous nucleation. At the growth stage of the porous structure, the model focuses on two major interface-related processes: corrosion of the LN element and surface diffusion of the MN element. The simulation results demonstrate that the interplay between the LN dissolution and MN diffusion determines the dealloying kinetics and morphology of the porous structure. The parameters affecting the interface processes, such as the chemical acid concentration, initial alloy composition, and surface diffusion coefficient, are demonstrated as the key factors controlling the morphology evolution of the dealloyed structure, which mirrors the experimentally observed behaviors. We also demonstrated the capability of this model to determine the content thresholds (parting limits) for porous structure formation.

Secondly, a MPF model was developed to simulate the morphological evolution of porous surfaces during the electrochemical dealloying of binary alloys. The governing equations for the alloy-porous cluster-electrolyte system account for the Butler-Volmer electrochemical reaction and are consistent with the classical nucleation theory. The simulation results imply that the electrochemical dealloying of Ag-Au alloy is dominated by the coupling of the electrochemical reaction of Ag with the surface diffusion of Au. The governing equations naturally reveal the fundamental mechanisms by which the electropotential and precursor composition affect the structure of a dealloyed material.

Thirdly, a MPF model was proposed for alloys with complex structures during dealloying. The simulation results showed that the dealloying of a precursor with an inert phase can generate a dealloyed structure comprising a porous matrix and compact embeddings. The model also predicted that the etching near defective sites is faster than that in the matrix. The results are in good agreement with those obtained in experiments. The formation of the bimodal porous structure was also presented via the dealloying of a dual-phase binary alloy composed of a solid solution and intermetallics, or two types of intermetallics. This model also enables the prediction of porous structures with hierarchical nested networks, featuring several relevant length scales and enhanced strength and stiffness.

6.2 IMPLICATIONS FOR FUTURE WORK

This research developed a MPF model to probe corrosion-controlled dealloying kinetics in metallic materials. Significant progress was made in understanding and predicting porous structure evolution during the dealloying process in this work. Quantitative agreements with experiments were also obtained using the proposed MPF models, which is extremely encouraging. Further refinement of the proposed models to include the effect of the passive film and study some complex dealloyable systems and other porous evolution processes is possible. As increasing numbers of studies have been conducted on novel porous metals and composites, we expect to extend our proposed model to the following issues meriting further studies.

1. While the PF models proposed here represent an improvement in understanding corrosion-controlled dealloying kinetics and predicting microstructure evolution, they are insufficient to include the effects of some complicating factors such as mechanical stress. Two important features accompany the dealloying process (chemical or electrochemical): the volume shrinkage and crack formation occurring in the dealloyed NPMs, affecting the mechanical properties of NPMs and their practical applications. It is suggested that the residual stress in the precursor, capillary force, and coherency stresses between the precursor and the dealloyed structure may be responsible for the crack formation.
2. Besides conventional aqueous acid or alkali solutions, researchers considered neutral solutions as electrolytes to obtain porous structures with small pore sizes and larger surface areas to avoid difficulties in handling and disposing of corrosive solutions. The dealloying process in a neutral solution is a complex process involving the formation of surface oxide (passive film), which may affect the mobility of MN elements. Due to the possible presence of surface oxides, the proposed models may require an additional order parameter to consider the formation and growth of surface oxides.
3. Perhaps the most promising application of the multi-phase models is simulating the electrochemical anodization of metals in solutions, which can produce anodic metal oxides with self-organized nanopores or nanotubes, such as the highly ordered porous anodic aluminum oxide (AAO) and titanium oxide nanotubes. The high regularity of

these nanostructures and the ability to tune the pore/tube dimensions based on physical, electrical, and chemical parameters have stimulated much interest in applying them to a wide range of materials technologies, such as photocatalysts and solar cells, and as templates for nanostructures. Although experimental and theoretical studies have identified many aspects of the chemical reactions and transport processes during anodization, the mechanism for pore initiation on AAO remains unclear. None of the models can predict realistic and quantitative 3-D morphological evolution of AAO nanopore structures from nucleation to steady-state growth against experimental observations.

APPENDICES

APPENDIX A: ELECTROCHEMICAL CORROSION KINETICS

According to the electrochemical reaction rate theory [89], for a general half-cell reaction

$$\mathrm{R} \rightleftharpoons \mathrm{O} + n\mathrm{e}^{-}, \tag{A1}$$

where R(O) represents the chemical formula of the reduction state (or oxidation state), n is the transferred charge number, and r (the reaction rate) is given by

$$r = k_0 \left[\exp\left(\frac{-\left(\mu_{\mathrm{t}}^{\mathrm{ex}} - \mu_1\right)}{RT}\right) - \exp\left(\frac{-\left(\mu_{\mathrm{t}}^{\mathrm{ex}} - \mu_2\right)}{RT}\right) \right], \tag{A2}$$

where k_0 is the reaction constant, and μ_1, μ_2, and $\mu_{\mathrm{t}}^{\mathrm{ex}}$ are the chemical potential of the reduction state, the chemical potential of the oxidation state, and the excess chemical potential of the transient state, respectively, and are expressed as:

$$\mu_1 = RT \ln a_1 + \mu_1^{\Theta}, \tag{A3a}$$

$$\mu_2 = RT \ln a_2 + \mu_2^{\Theta} + nF\left(\varphi - \varphi_{\mathrm{M}}\right), \tag{A3b}$$

and

$$\mu_{\mathrm{t}}^{\mathrm{ex}} = RT \ln r_{\mathrm{t}} + \rho\mu_1^{\Theta} + (1-\rho)\left(\mu_2^{\Theta} + nF\left(\varphi - \varphi_{\mathrm{M}}\right)\right) \tag{A3c}$$

where μ_1^{Θ} and μ_2^{Θ} are the standard chemical potential of the reduction state and the oxidation state, respectively; a_1 and a_2 are the activity of the reduction state and the oxidation

state, respectively; φ and φ_{M} are the electrolyte and electrode potential, respectively; r_{t} is the activity coefficient of the transient state; and ρ is the symmetry factor. Substituting Eq. (A3) into Eq. (A2) gives

$$r = \frac{k_0}{r_t}\left[\exp\left(\ln a_1 + \frac{(1-\rho)\left(\mu_1^{\ominus} - \mu_2^{\ominus} - F\left(\varphi_{\mathrm{M}} - \varphi\right)\right)}{RT}\right) - \exp\left(\ln a_2 + \frac{-\rho\left(\mu_1^{\ominus} - \mu_2^{\ominus} - F\left(\varphi_{\mathrm{M}} - \varphi\right)\right)}{RT}\right)\right] \tag{A4}$$

Thus, for the dissolution of Ag shown in Eq. (1), a dilute solution is assumed ($a_* = c_*$), and the reaction rate can be expressed as follows:

$$r_{\mathrm{Ag}\to\mathrm{Ag}^+} = \kappa\left[\exp\left(\frac{RT\ln a_{\mathrm{Ag}} + (1-\rho)\Lambda}{RT}\right) - c_{\mathrm{Ag}^+}\exp\left(\frac{-\rho\Lambda}{RT}\right)\right] \tag{A5}$$

In Eq. (A5), $\kappa = k_0/r_{\mathrm{t}}$ is the reaction coefficient, and $RT\ln a_{\mathrm{Ag}}$ and $\Lambda = F\left(\varphi_{\mathrm{M}} - \varphi\right) - \mu_{\mathrm{Ag}^+}^{\ominus}$ are the concentration and activation driving force, respectively. Based on the definition of activity in [89] and $\phi_1 = c_{\mathrm{Ag}}/c_{\mathrm{Ag},0}$, the activity of Ag has the form of

$$RT\ln a_{\mathrm{Ag}} = \frac{\delta\int_V \left(f_{\mathrm{int}} + f_{\mathrm{chem}}\right)dV}{\delta C_{\mathrm{Ag}}} - \mu_{\mathrm{Ag}}^{\ominus} = \mu_{\mathrm{int}} + \mu_{\mathrm{ini}}, \tag{A6a}$$

with

$$\mu_{\mathrm{int}} = \frac{W\phi_1(1-\phi_1)(1-2\phi_1) - \varepsilon\nabla^2\phi_1}{C_{\mathrm{ref}}c_{\mathrm{Ag},0}} - \mu_{\mathrm{Ag}}^{\ominus}, \tag{A6b}$$

and

$$\mu_{\mathrm{ini}} = \frac{\alpha}{C_{\mathrm{ref}}}\left(1-2c_{\mathrm{Ag}}\right) \approx \frac{\alpha}{C_{\mathrm{ref}}}\left(1-2c_{\mathrm{Ag},0}\right) \tag{A6c}$$

By substituting Eq. (2) into Eq. (A6a), the concentration driving force can be divided into two parts, $\mu_{\text{int,}}$ and μ_{ini}, which correspond to the effects of the interfacial energy and the alloy composition, respectively. Due to the homogeneity of the precursor, we use the initial average alloy composition ($c_{\text{Ag,0}}$) to describe the effect of the alloy composition, as shown in Eq. (A6c). As $\mu^{\text{int}} \ll RT$, a first-order approximation of the Taylor expansion can be used to rewrite the dissolution rate in Eq. (A5) as

$$\begin{aligned} r_{\text{Ag}\to\text{Ag}^+} &\approx r_{\text{Ag}\to\text{Ag}^+}\Big|_{(\mu_{\text{int}}/RT)=0} + \frac{\partial r_{\text{Ag}\to\text{Ag}^+}}{\partial\left(\mu_{\text{int}}/RT\right)}\Big|_{(\mu_{\text{int}}/RT)=0}\frac{\mu_{\text{int}}}{RT} \\ &= L\times\mu_{\text{int}} + \kappa\left[\exp\left(\frac{\mu_{\text{ini}}+(1-\rho)\Lambda}{RT}\right) - c_{\text{Ag}^+}\exp\left(\frac{-\rho\Lambda}{RT}\right)\right], \end{aligned} \tag{A7a}$$

with

$$L = \frac{\kappa}{RT}\left[\exp\left(\frac{\mu_{\text{ini}}+(1-\rho)\Lambda}{RT}\right)\right] \tag{A7b}$$

APPENDIX B: PARAMETERS USED IN CHAPTER 4

The standard chemical potential

According to the Nernst equation, the equilibrium potential for reaction (B1) can be expressed as follows:

$$\varphi_{\text{eq}} = \frac{\mu_2^{\ominus} - \mu_1^{\ominus}}{nF} + \frac{RT}{nF}\ln\left(\frac{a_2}{a_1}\right) \tag{B1}$$

For the dissolution of Ag, the equilibrium potential is 0.8 V, thus $\mu_{\text{Ag}^+}^{\ominus}$ = 77.2 kJ/mol, assuming that $\mu_{\text{Ag}}^{\ominus}$ = $\mu_{\text{e}^-}^{\ominus}$ = 0 kJ/mol and ignoring the effect of concentration.

The charge transfer coefficient

The charge transfer coefficient (ρ) characterizes the symmetry of electrochemical reactions of precursors with the same initial composition, and can be calibrated by rearranging the classical Butler–Volmer equation and ignoring the cathode reaction in a half-cell reaction. This is expressed as

$$\rho=1-\frac{RT}{\left(\varphi_{\mathrm{M}}^{1}-\varphi_{\mathrm{M}}^{2}\right)}\ln\left(\frac{i_1}{i_2}\right), \tag{B2}$$

where i_1 and i_2 are the current densities corresponding to the applied potential φ_{M}^{1} and φ_{M}^{2}, respectively. By using the experimentally measured current density versus potential curve [94], ρ is evaluated as 0.7.

The thermodynamic constant

For an Ag–Au alloy, it has been experimentally observed that the required potential to reach the same dissolution current nearly increases by an average of 0.1 V for each 0.05 increase in $c_{\mathrm{Ag},0}$ [94]. Thus $\alpha = 0.5C_{\mathrm{ref}}\left(1-\rho\right)F\left(E_2-E_1\right)\big/\left(c_{\mathrm{Ag},0}^{2}-c_{\mathrm{Ag},0}^{1}\right) = -6.56\times10^{9}\ \mathrm{J/m^3}$.

The electrochemical reaction constant

By assuming that the species concentrations and electropotential are constant, the following expression for the migration velocity of the alloy–electrolyte interface or the dealloying front in a one-dimensional steady-state situation can be derived:

$$v=\frac{\kappa l}{C_{\mathrm{ref}}c_{\mathrm{Ag},0}}\left[\exp\left(\frac{\alpha\left(1-2c_{\mathrm{Ag},0}\right)\big/C_{\mathrm{ref}}+\left(1-\rho\right)\Lambda}{RT}\right)-c_{\mathrm{Ag^+}}\exp\left(\frac{-\rho\Lambda}{RT}\right)\right] \tag{B3}$$

Hence, $\kappa = 1.4 \times 10^{-5}$ mol/(m^3 s), where $c_{Ag,0} = 0.7$, $\varphi_M = 1.2$ V, and $v = 4 \times 10^{-10}$ m/s.

NOMENCLATURE

The nomenclature for this thesis is provided in separate tables for each chapter. Some symbols represent different parameters in different chapters.

NOMENCLATURE IN CHAPTER 3

c_{Ag}	Molar fraction of silver	k_0	Reaction constant
R	Ideal gas constant energy	T	Absolute temperature
F	Faraday constant	G	Reaction activation energy
c_0	Initial Au compositions	c_{a}	Nitric acid solutions
ϕ_i	Order parameters	c_{Au}	Molar fraction of gold
ε	Gradient energy coefficient	W	Potential well height
σ	Interfacial energy density	l	Interface thickness
f_{chem}^{i}	Chemical free-energy density of phase	c_{Ag}^{i}	compositions of Ag in ϕ_i

f_{chem}	Chemical free-energy density	h_i	Interpolation function
c^i_{Au}	compositions of Au in ϕ_i	L	Kinetic interface parameter
$c^i_{\text{Au,e}}$	Normalized equilibrium concentrations of Au in ϕ_i	$c^i_{\text{Ag,e}}$	Normalized equilibrium concentrations of Ag in ϕ_i
D^i_{Ag}	Bulk diffusion coefficient of Ag in ϕ_i	D^i_{Au}	Bulk diffusion coefficient of Au in ϕ_i
D^{s}_{Ag}	Surface diffusion coefficient of Ag	D^{s}_{Au}	Surface diffusion coefficient of Au
I_0	Numerical constant	a	Nucleation prefactor
A	Free-energy density curvature	B	Freedensity curvature
Ω_i	Grand potential of phase ϕ_i	ξ_{ϕ_2}	Thermal fluctuations in the interfacial layer
ξ_0	Strength of the fluctuations.	$\Delta\Omega_{23}$	Chemical driving force

c_{Au}^{p}	Peak concentration of the Au element	v	Dealloying velocity
G_0	Activation energy parameter	k_1	Activation energy parameter
λ	Ligament spacing		

NOMENCLATURE IN CHAPTER 4

R	Ideal gas constant energy	T	Absolute temperature
F	Faraday constant	c_k	Dimensionless concentration of component k
ϕ_i	Order parameters	C_{ref}	Reference concentration
C_k	Molar concentration of component k	σ	Interfacial energy
φ	Electrostatic potential;	l	Interfacial thickness
ε	Gradient energy coefficient	f_{elec}	Electrostatic energy density
n_k	Charge number of component k	f_{chem}	Chemical free-energy density
a	Numerical constant.	$\mu_*^{\ominus}$	Standard chemical potential
$c_{\text{Ag},0}$	Alloy's initial Ag concentration	f_{Au}^{i}	Free energy density of Au in ϕ_i

A	Free energy curvature	$c^{i}_{\mathrm{Au,e}}$	Dimensionless equilibrium concentration of Au in ϕ_i
v	Simulated dealloying front propagation	i	Experimental current density
M	Molar mass of Ag	J	Corrosion flux of Ag into the electrolyte per unit time and per unit area
ρ_{Ag}	Density of Ag	$V_{\mathrm{Ag\text{-}Alloy}}$	Volume fractions of Ag in the alloy
$V_{\mathrm{Ag\text{-}NPG}}$	Residual Ag in the dealloyed nanoporous structure	φ_{M}	Applied potential
E_{c}	Electropotential threshold	$c_{\mathrm{Ag,0}}$	Precursor composition

NOMENCLATURE IN CHAPTER 5

ϕ_i	Order parameters	C_N	Concentration of component k
C_N	Molar concentration of component N	C_{ref}	Reference concentration
c_N	Dimensionless concentration of component N	f_{gra}	Gradient free-energy density
f_{chem}	Chemical free-energy density	f_{elec}	Electrostatic energy density
n_k	Charge number of component k	ε	Gradient energy coefficient
l	Interfacial thickness	σ	Interfacial energy
φ	Electrostatic potential	a	Numerical constant
R	Ideal gas constant energy	T	Absolute temperature
$\mu_k^{\ominus}$	Standard chemical potential of ion species k	f_{B}^{i}	Free energy density of B in ϕ_i

$f^{'}$	Free energy curvature	c_{B}^{i}	Dimensionless concentration of B in ϕ_i
$c_{\mathrm{B,e}}^{i}$	Dimensionless equilibrium concentration of B in ϕ_i	$c_{\mathrm{A,0}}$	Initial A concentration in the alloy
k_0	Reaction constant	ρ	Charge transfer coefficient
$\Delta\mu$	Activation overpotential	F	Faraday constant
μ_M	Effect of phase composition of phase M	a_*	Activities of reactants and products
L_M	Phase-field mobilitiy parameter	κ_M	Reaction kinetic constant
μ_{int}^{M}	Driving force from the interface energy	Λ	Driving force from the applied electropotential
φ_{ap}	Applied potential	r	Random number
I_0	Nucleation prefactor.	ζ_0	Fluctuation intensity

M_{B}	Diffusion mobility	D_{B}^{i}	Diffusion coefficients of B in bulk phases coefficient at the $\phi_M/\phi_{\mathrm{ele}}$ and $\phi_{\mathrm{por}}/\phi_{\mathrm{ele}}$ interface
D_{B}^{M}	Diffusion coefficient of B at the $\phi_M/\phi_{\mathrm{ele}}$ interface	$D_{\mathrm{B}}^{\mathrm{por}}$	Diffusion coefficient of B at the $\phi_{\mathrm{por}}/\phi_{\mathrm{ele}}$ interface
ψ_i	Electric conductivity for each phase	F^{sd}	Total free energy of spinodal decomposition system
u	Volume fraction of the solid phase	W_u	Height of the potential barrier of spinodal decomposition system
k_u	Gradient term coefficient	M_u	Mobility in spinodal decomposition system

REFERENCES

[1] R. Xia, R. N. Wu, Y. L. Liu, and X. Y. Sun, "The role of computer simulation in nanoporous metals-a review," *Materials (Basel).*, vol. 8, no. 8, pp. 5060–5083, 2015, doi: 10.3390/ma8085060.

[2] J. Zhang and C. M. Li, "Nanoporous metals: fabrication strategies and advanced electrochemical applications in catalysis, sensing and energy systems," *Chem. Soc. Rev*, vol. 41, pp. 7016–7031, 2012, doi: 10.1039/c2cs35210a.

[3] Y. Ding and Z. Zhang, *Nanoporous metals for advanced energy technologies*. Springer, 2016.

[4] I. Mccue, E. Benn, B. Gaskey, and J. Erlebacher, "Dealloying and dealloyed materials," 2016, doi: 10.1146/annurev-matsci-070115-031739.

[5] Y. Ding and M. Chen, "Nanoporous metals for catalytic and optical applications," *MRS Bull.*, vol. 34, pp. 569–576, 2009.

[6] Erkin Seker, W.-C. Shih, and K. J. Stine, "Nanoporous metals by alloy corrosion: Bioanalytical and biomedical applications," *MRS Bull.*, vol. 43, pp. 49–55, 2018, doi: 10.1557/mrs.2017.298.

[7] Y. Gaoand and Y. Ding, "Nanoporous metals for heterogeneous catalysis:following the success of raney nickel," *Chem. Eur.J*, vol. 2020, pp. 8845–8856, 2012, doi: 10.1002/chem.202000471.

[8] T. Song, M. Yan, and M. Qian, "The enabling role of dealloying in the creation of specific hierarchical porous metal structures—A review," *Corrosion Science*, vol. 134. Elsevier Ltd, pp. 78–98, 15-Apr-2018, doi: 10.1016/j.corsci.2018.02.013.

[9] T. Juarez, J. Biener, J. Weissmüller, and A. M. Hodge, "Nanoporous Metals with Structural Hierarchy: A Review," 2017, doi: 10.1002/adem.201700389.

[10] T. Fujita, "Hierarchical nanoporous metals as a path toward the ultimate three-dimensional functionality," *Sci. Technol. Adv. Mater.*, vol. 18, no. 1, pp. 724–740, 2017, doi: 10.1080/14686996.2017.1377047.

[11] R. B. Abrams, "The dezincification of brass," *Trans. Am. Electrochem. Soc.*, vol. 42, pp. 39–54, 1922.

[12] R. C. Newman, S. G. Corcoran, J. Erlebacher, M. J. Aziz, and K. Sieradzki, "Alloy corrosion," *MRS Bull.*, vol. 24, no. 7, pp. 24–28, 1999, doi: 10.1557/S0883769400052660.

[13] Y. Ding, Y. J. Kim, and J. Erlebacher, "Nanoporous gold leaf: 'ancient technology'/advanced material," *Adv. Mater.*, vol. 16, no. 21, pp. 1897–1900, 2004, doi: 10.1002/adma.200400792.

[14] H. Galinski *et al.*, "Dealloying of platinum-aluminum thin Films: Dynamics of pattern formation," *Phys. Rev. Lett.*, vol. 107, no. 22, pp. 6–9, 2011, doi: 10.1103/PhysRevLett.107.225503.

[15] W. Liu, L. Chen, J. Yan, N. Li, S. Shi, and S. Zhang, "Nanoporous copper from dual-phase alloy families and its technology application in lithium ion batteries," *Corros. Rev.*, vol. 33, no. 5, pp. 203–231, 2015, doi: 10.1515/corrrev-2014-0066.

[16] Z. Lu *et al.*, "Three-dimensional bicontinuous nanoporous materials by vapor phase dealloying," *Nat. Commun.*, vol. 9, no. 1, pp. 1–7, 2018, doi: 10.1038/s41467-017-02167-y.

[17] Y. An *et al.*, "Dealloying: An effective method for scalable fabrication of 0D, 1D, 2D, 3D materials and its application in energy storage," *Nano Today*, vol. 37, p. 101094, 2021, doi: 10.1016/j.nantod.2021.101094.

[18] I. McCue, B. Gaskey, P. A. Geslin, A. Karma, and J. Erlebacher, "Kinetics and morphological evolution of liquid metal dealloying," *Acta Mater.*, vol. 115, pp. 10–23, 2016, doi: 10.1016/j.actamat.2016.05.032.

[19] I. McCue, A. Karma, and J. Erlebacher, "Pattern formation during electrochemical and liquid metal dealloying," *MRS Bull.*, vol. 43, no. 1, pp. 27–34, 2018, doi: 10.1557/mrs.2017.301.

[20] P. A. Geslin, I. McCue, B. Gaskey, J. Erlebacher, and A. Karma, "Topology-generating interfacial pattern formation during liquid metal dealloying," *Nat. Commun.*, vol. 6, pp. 1–8, 2015, doi: 10.1038/ncomms9887.

[21] N. A. Senior and R. C. Newman, "Synthesis of tough nanoporous metals by controlled electrolytic dealloying," *Nanotechnology*, vol. 17, no. 9, pp. 2311–2316, 2006, doi: 10.1088/0957-4484/17/9/040.

[22] X. Lu, E. Bischoff, R. Spolenak, and T. J. Balk, "Investigation of dealloying in Au-Ag thin films by quantitative electron probe microanalysis," *Scr. Mater.*, vol. 56, no. 7, pp. 557–560, 2007, doi: 10.1016/j.scriptamat.2006.12.022.

[23] K. Kolluri and M. J. Demkowicz, "Coarsening by network restructuring in model nanoporous gold," *Acta Mater.*, vol. 59, no. 20, pp. 7645–7653, 2011, doi: 10.1016/j.actamat.2011.08.037.

[24] H. J. Qiu, L. Peng, X. Li, H. T. Xu, and Y. Wang, "Using corrosion to fabricate various

nanoporous metal structures," *Corros. Sci.*, vol. 92, pp. 16–31, 2015, doi: 10.1016/j.corsci.2014.12.017.

[25] J. Erlebacher, M. J. Aziz, A. Karma, N. Dimitrov, and K. Sieradzki, "Evolution of nanoporosity in dealloying," *Nature*, vol. 410, no. 6827, pp. 450–453, 2001, doi: 10.1038/35068529.

[26] Z. Zhang, Y. Wang, Z. Qi, W. Zhang, J. Qin, and J. Frenzel, "Generalized fabrication of nanoporous metals (Au, Pd, Pt, Ag, and Cu) through chemical dealloying," *J. Phys. Chem. C*, vol. 113, pp. 12629–12636, 2009, doi: 10.1021/jp811445a.

[27] X. Wang, Z. Zhang, H. Ji, J. Xu, X. Huang, and Y. Ma, "Dealloying of single-phase Al2Au to nanoporous gold ribbon/film with tunable morphology in inorganic and organic acidic media," *Appl. Surf. Sci.*, vol. 258, no. 22, pp. 9073–9079, 2012, doi: 10.1016/j.apsusc.2012.05.165.

[28] A. Dursun, "Nanoposity formation in Ag-Au alloys," The Virginia Polytechnic Institute and State University, 2003.

[29] H. Xu and T. Zhang, "Formation of ultrafine spongy nanoporous metals (Ni, Cu, Pd, Ag and Au) by dealloying metallic glasses in acids with capping effect," *Corros. Sci.*, vol. 153, no. January, pp. 1–11, 2019, doi: 10.1016/j.corsci.2019.03.029.

[30] H. W. Pickering, "Volume diffusion during anodic dissolution of a binary alloy," *J. Electrochem. Soc.*, vol. 115, no. 2, pp. 143–147, 1968.

[31] A. J. Forty, "Corrosion micromorphology of noble metal alloys and depletion gilding," *Nature*, vol. 282, no. 5739, pp. 597–598, 1979, doi: 10.1038/282597a0.

[32] K. Sieradzki, "Curvature effects in alloy dissolution," *J. Electrochem. Soc.*, vol. 140, no. 10, pp. 2868–2872, 1993, doi: 10.1149/1.2220924.

[33] R. C. Newman, R. R. Corderman, and K. Sieradzki, "Evidence for dealloying of austenitic stainless steels in simulated stress corrosion crack environments," *Br. Corros. J.*, 1989, doi: 10.1179/000705989798270261.

[34] K. Sieradzki, R. R. Corderman, K. Shukla, R. C. Newman, and K. Sieradzki, "Computer simulations of corrosion: Selective dissolution of binary alloys," *Philos. Mag. A Phys. Condens. Matter, Struct. Defects Mech. Prop.*, vol. 59, no. 4, pp. 713–746, 1989, doi: 10.1080/01418618908209817.

[35] J. Erlebacher and R. Seshadri, "Hard materials with tunable porosity," *MRS Bull.*, vol. 34, pp. 561–568, 2009.

[36] J. Erlebacher, "An atomistic description of dealloying porosity evolution, the critical

potential, and rate-limiting behavior," *J. Electrochem. Soc.*, vol. 151, no. 10, pp. 614–626, 2004, doi: 10.1149/1.1784820.

[37] S. A. Policastro *et al.*, "Surface diffusion and dissolution kinetics in the electrolyte–metal interface," *J. Electrochem. Soc.*, vol. 157, no. 10, pp. 328–337, 2010, doi: 10.1149/1.3478572.

[38] J. Erlebacher and I. McCue, "Geometric characterization of nanoporous metals," *Acta Mater.*, vol. 60, no. 17, pp. 6164–6174, 2012, doi: 10.1016/j.actamat.2012.07.059.

[39] T. Krekeler *et al.*, "Silver-rich clusters in nanoporous gold," *Mater. Res. Lett.*, vol. 5, no. 5, pp. 314–321, 2017, doi: 10.1080/21663831.2016.1276485.

[40] S. S. R. Saane, K. R. Mangipudi, K. U. Loos, J. T. M. De Hosson, and P. R. Onck, "Multiscale modeling of charge-induced deformation of nanoporous gold structures," *J. Mech. Phys. Solids*, vol. 66, no. 1, pp. 1–15, May 2014, doi: 10.1016/j.jmps.2014.01.007.

[41] X. Y. Sun, G. K. Xu, X. Li, X. Q. Feng, and H. Gao, "Mechanical properties and scaling laws of nanoporous gold," *J. Appl. Phys.*, vol. 113, no. 2, p. 023505, 2013, doi: 10.1063/1.4774246.

[42] J. R. Lukes and C. L. Tien, "Molecular dynamics simulation of thermal conduction in nanoporous thin films," *Microscale Thermophys. Eng.*, vol. 8, no. 4, pp. 341–359, 2004, doi: 10.1080/10893950490516893.

[43] M. Hakamada, F. Hirashima, M. Takahashi, T. Nakazawa, and M. Mabuchi, "Large-strain-induced magnetic properties of Co electrodeposited on nanoporous Au," *J. Appl. Phys.*, vol. 109, no. 8, p. 84315, 2011.

[44] Y. C. K. Chen-Wiegart, S. Wang, I. McNulty, and D. C. Dunand, "Effect of Ag-Au composition and acid concentration on dealloying front velocity and cracking during nanoporous gold formation," *Acta Mater.*, vol. 61, no. 15, pp. 5561–5570, 2013, doi: 10.1016/j.actamat.2013.05.039.

[45] H. X. Zhu *et al.*, "The elastic and geometrical properties of micro-and nano-structured hierarchical random irregular honeycombs," doi: 10.1007/s10853-014-8288-y.

[46] D. Wheeler, D. Josell, and T. P. Moffat, "Modeling superconformal electrodeposition using the level set method," *J. Electrochem. Soc.*, vol. 150, no. 5, p. C302, 2003.

[47] S. Osher and J. A. Sethian, "Fronts propagating with curvature-dependent speed: Algorithms based on Hamilton-Jacobi formulations," *J. Comput. Phys.*, vol. 79, no. 1, pp. 12–49, 1988.

[48] S. B. Biner, *Programming Phase-Field Modeling*. Springer, 2017.

[49] I. Singer-Loginova and H. M. Singer, “The phase field technique for modeling multiphase materials,” *Reports Prog. Phys.*, vol. 71, no. 10, 2008, doi: 10.1088/0034-4885/71/10/106501.

[50] I. Steinbach, “Phase-field models in materials science,” *Model. Simul. Mater. Sci. Eng.*, vol. 17, no. 7, 2009, doi: 10.1088/0965-0393/17/7/073001.

[51] L. Liang and L. Q. Chen, “Nonlinear phase field model for electrodeposition in electrochemical systems,” *Appl. Phys. Lett.*, vol. 105, no. 26, 2014, doi: 10.1063/1.4905341.

[52] D. A. Crowson, D. Farkas, and S. G. Corcoran, “Geometric relaxation of nanoporous metals The role of surface relaxation,” *Scr. Mater.*, vol. 56, no. 11, pp. 919–922, 2007.

[53] X.-Y. Sun, G.-K. Xu, X. Li, X.-Q. Feng, and H. Gao, “Mechanical properties and scaling laws of nanoporous gold,” *J. Appl. Phys.*, vol. 113, no. 2, p. 23505, 2013.

[54] W. Mai, S. Soghrati, and R. G. Buchheit, “A phase field model for simulating the pitting corrosion,” *Corros. Sci.*, vol. 110, pp. 157–166, 2016, doi: 10.1016/j.corsci.2016.04.001.

[55] T. Q. Ansari, Z. Xiao, S. Hu, Y. Li, J. L. Luo, and S. Q. Shi, “Phase-field model of pitting corrosion kinetics in metallic materials,” *NPJ Comput. Mater.*, vol. 4, no. 1, pp. 1–9, 2018, doi: 10.1038/s41524-018-0089-4.

[56] L. Chen *et al.*, “Modulation of dendritic patterns during electrodeposition: A nonlinear phase-field model,” *J. Power Sources*, vol. 300, pp. 376–385, 2015, doi: 10.1016/j.jpowsour.2015.09.055.

[57] C. Lin, H. Ruan, and S. Q. Shi, “Phase field study of mechanico-electrochemical corrosion,” *Electrochim. Acta*, vol. 310, pp. 240–255, 2019, doi: 10.1016/j.electacta.2019.04.076.

[58] C. Lin and H. Ruan, “Multi-phase-field modeling of localized corrosion involving galvanic pitting and mechano-electrochemical coupling,” *Corros. Sci.*, vol. 177, no. August, p. 108900, 2020, doi: 10.1016/j.corsci.2020.108900.

[59] T. Q. Ansari, J.-L. Luo, and S.-Q. Shi, “Multi-phase-field model of intergranular corrosion kinetics in sensitized metallic materials,” *J. Electrochem. Soc.*, vol. 167, no. 6, p. 061508, 2020, doi: 10.1149/1945-7111/ab856d.

[60] T. Q. Ansari, J.-L. Luo, and S.-Q. Shi, “Modeling the effect of insoluble corrosion products on pitting corrosion kinetics of metals,” *npj Mater. Degrad.*, vol. 3, no. 1, pp. 1–11, 2019, doi: 10.1038/s41529-019-0090-5.

[61] C. Özmetin, M. Çopur, A. Yartasi, and M. M. Kocakerim, “Kinetic investigation of

reaction between metallic silver and nitric acid solutions," *Chem. Eng. Technol.*, vol. 23, no. 8, pp. 707–711, 2000, doi: 10.1002/1521-4125(200008)23:8<707::AID-CEAT707>3.0.CO;2-L.

[62] Y. C. K. Chen-Wiegart, S. Wang, W. K. Lee, I. McNulty, P. W. Voorhees, and D. C. Dunand, "In situ imaging of dealloying during nanoporous gold formation by transmission X-ray microscopy," *Acta Mater.*, vol. 61, no. 4, pp. 1118–1125, 2013, doi: 10.1016/j.actamat.2012.10.017.

[63] J. Snyder and J. Erlebacher, "Kinetics of crystal etching limited by terrace dissolution," *J. Electrochem. Soc.*, vol. 157, no. 3, pp. 125–130, 2010, doi: 10.1149/1.3280299.

[64] J. Kundin, E. Pogorelov, and H. Emmerich, "Phase-field modeling of the microstructure evolution and heterogeneous nucleation in solidifying ternary Al–Cu–Ni alloys," *Acta Mater.*, vol. 83, pp. 448–459, 2015, doi: 10.1016/j.actamat.2014.09.057.

[65] G. Fairweather, *Finite element Galerkin methods for differential equations*. New York, NY : Dekker: Dekker, 1978.

[66] U. M. Ascher and L. R. Petzold, *Computer methods for ordinary differential equations and differential-algebraic equations*, vol. 61. Siam, 1998.

[67] T. W. Heo and L. Q. Chen, "Phase-field modeling of nucleation in solid-state phase transformations," *JOM*, vol. 66, no. 8, pp. 1520–1528, 2014, doi: 10.1007/s11837-014-1033-9.

[68] E. Detsi, M. Van De Schootbrugge, S. Punzhin, P. R. Onck, and J. T. M. De Hosson, "On tuning the morphology of nanoporous gold," *Scr. Mater.*, vol. 64, no. 4, pp. 319–322, 2011, doi: 10.1016/j.scriptamat.2010.10.023.

[69] M. C. Dixon, T. A. Daniel, M. Hieda, D. M. Smilgies, M. H. W. Chan, and D. L. Allara, "Preparation, structure, and optical properties of nanoporous gold thin films," *Langmuir*, vol. 23, no. 5, pp. 2414–2422, 2007, doi: 10.1021/la062313z.

[70] X. L. Ye, N. Lu, X. J. Li, K. Du, J. Tan, and H. J. Jin, "Primary and secondary dealloying of Au(Pt)-Ag: Structural and compositional evolutions, and volume shrinkage," *J. Electrochem. Soc.*, vol. 161, no. 12, pp. C517–C526, 2014, doi: 10.1149/2.0131412jes.

[71] J. X. Wang *et al.*, "Kirkendall effect and lattice contraction in nanocatalysts: a new strategy to enhance sustainable activity," *J. Am. Chem. Soc*, vol. 133, pp. 13551–13557, 2011, doi: 10.1021/ja204518x.

[72] L. Dubau *et al.*, "Further insights into the durability of Pt3Co/C electrocatalysts: Formation of 'hollow' Pt nanoparticles induced by the Kirkendall effect," *Electrochim. Acta*, vol. 56, no. 28, pp. 10658–10667, 2011, doi: 10.1016/j.electacta.2011.03.073.

[73] D. M. Artymowicz, J. Erlebacher, and R. C. Newman, “Relationship between the parting limit for dealloying and a particular geometric high-density site percolation threshold,” *Philos. Mag.*, vol. 89, no. 21, pp. 1663–1693, 2009, doi: 10.1080/14786430903025708.

[74] A. Dursun, D. V. Pugh, and S. G. Corcoran, “Dealloying of Ag-Au alloys in halide-containing electrolytes. Affect on critical potential and pore size,” *J. Electrochem. Soc.*, vol. 150, no. 7, pp. 0–5, 2003, doi: 10.1149/1.1580824.

[75] L. H. Qian and M. W. Chen, “Ultrafine nanoporous gold by low-temperature dealloying and kinetics of nanopore formation,” *Appl. Phys. Lett.*, vol. 91, no. 8, pp. 2005–2008, 2007, doi: 10.1063/1.2773757.

[76] C. Alonso, R. C. Salvarezza, J. M. Vara, and A. J. Arvia, “The surface diffusion of gold atoms on gold electrodes in acid solution and its dependence on the presence of foreign adsorbates,” *Electrochim. Acta*, vol. 35, no. 9, pp. 1331–1336, 1990, doi: 10.1016/0013-4686(90)85003-6.

[77] M. Hakamada, K. Tajima, K. Yoshimura, Y. Chino, and M. Mabuchi, “Solid/electrolyte interface phenomena during anodic polarization of Pd0.2M0.8 (M= Fe, Co, Ni) alloys in H2SO4,” *J. Alloys Compd.*, vol. 494, no. 1–2, pp. 309–314, 2010, doi: 10.1016/j.jallcom.2010.01.019.

[78] W. Liu *et al.*, “A facile one-pot dealloying strategy to synthesize monolithic asymmetry-patterned nanoporous copper ribbons with tunable microstructure and nanoporosity,” *RSC Adv.*, vol. 6, no. 4, pp. 2662–2670, 2016, doi: 10.1039/c5ra22978b.

[79] W. Liu, X. Chen, J. Zhang, S. Zhang, and S. Shi, “In-situ synthesis of freestanding porous SnOx-decorated Ni3Sn2 composites with enhanced Li storage properties,” *Chem. Eng. J.*, vol. 412, no. October 2020, p. 128591, 2021, doi: 10.1016/j.cej.2021.128591.

[80] J. Xu, Y. Wang, and Z. Zhang, “Potential and Concentration Dependent Electrochemical Dealloying of Al 2 Au in Sodium Chloride Solutions,” *J. Phys. Chem. C*, vol. 116, 2012, doi: 10.1021/jp210488t.

[81] J. C. Thorp *et al.*, “(No Title),” *Appl. Phys. Lett*, vol. 88, p. 33110, 2006, doi: 10.1063/1.2161939.

[82] Y. Zhan *et al.*, “Bestow metal foams with nanostructured surfaces via a convenient electrochemical method for improved device performance,” doi: 10.1007/s12274-016-1123-9.

[83] H. W. Pickering and C. Wagner, “Electrolytic Dissolution of Binary Alloys Containing a Noble Metal,” 1967.

[84] Q. Zhang, X. Wang, Z. Qi, Y. Wang, and Z. Zhang, “A benign route to fabricate

nanoporous gold through electrochemical dealloying of Al-Au alloys in a neutral solution," *Electrochim. Acta*, vol. 54, no. 26, pp. 6190–6198, 2009, doi: 10.1016/j.electacta.2009.05.089.

[85] J. Snyder, K. Livi, and J. Erlebacher, "Dealloying Silver/Gold Alloys in Neutral Silver Nitrate Solution: Porosity Evolution, Surface Composition, and Surface Oxides," *J. Electrochem. Soc.*, vol. 155, no. 8, p. C464, 2008, doi: 10.1149/1.2940319.

[86] J. Fu *et al.*, "PH-Controlled Dealloying Route to Hierarchical Bulk Nanoporous Zn Derived from Metastable Alloy for Hydrogen Generation by Hydrolysis of Zn in Neutral Water," *ACS Appl. Energy Mater.*, vol. 1, no. 7, pp. 3198–3205, 2018, doi: 10.1021/acsaem.8b00419.

[87] J. Li, S. Hu, Y. Li, and S. Q. Shi, "Evolution mechanisms and kinetics of porous structures during chemical dealloying of binary alloys," *Microporous Mesoporous Mater.*, doi: 10.1016/j.micromeso.2021.111092.In press.

[88] S. G. Kim, W. T. Kim, and T. Suzuki, "Phase-field model for binary alloys," *Phys. Rev. E - Stat. Physics, Plasmas, Fluids, Relat. Interdiscip. Top.*, vol. 60, no. 6, pp. 7186–7197, 1999, doi: 10.1103/PhysRevE.60.7186.

[89] M. Z. Bazant, "Theory of chemical kinetics and charge transfer based on nonequilibrium thermodynamics," *Acc. Chem. Res.*, vol. 46, no. 5, pp. 1144–1160, 2013, doi: 10.1021/ar300145c.

[90] T. Q. Ansari, J.-L. Luo, and S.-Q. Shi, "Modeling the effect of insoluble corrosion products on pitting corrosion kinetics of metals," *NPJ Mater. Degrad.*, vol. 3, no. 1, pp. 1–12, 2019, doi: 10.1038/s41529-019-0090-5.

[91] G. F. Smith and F. Ring, "The preparation, aqueous and perchloric acid solubilities, solution densities and transition temperature of silver perchlorate," *J. Am. Chem. Soc.*, vol. 59, no. 10, pp. 1889–1890, 1937, doi: 10.1021/ja01289a027.

[92] W. Mai and S. Soghrati, "New phase field model for simulating galvanic and pitting corrosion processes," *Electrochim. Acta*, vol. 260, pp. 290–304, 2018, doi: 10.1016/j.electacta.2017.12.086.

[93] "http://www.comsol.com." .

[94] A. Dursun, D. V. Pugh, and S. G. Corcoran, "Probing the dealloying critical potential morphological characterization and steady-state current behavior," *J. Electrochem. Soc.*, vol. 152, no. 2, pp. 65–72, 2005, doi: 10.1149/1.1848351.

[95] A. Dursun, D. V. Pugh, and S. G. Corcoran, "A steady-state method for determining the dealloying critical potential," *Electrochem. Solid-State Lett.*, vol. 6, no. 8, pp. 34–36,

2003, doi: 10.1149/1.1588111.

[96] K. Sieradzki, N. Dimitrov, D. Movrin, C. McCall, N. Vasiljevic, and J. Erlebacher, "The dealloying critical potential," *J. Electrochem. Soc.*, vol. 149, no. 8, pp. B370–B377, 2002, doi: 10.1149/1.1492288.

[97] M. M. Biener *et al.*, "ALD functionalized nanoporous gold: Thermal stability, mechanical properties, and catalytic activity," *Nano Lett.*, vol. 11, no. 8, pp. 3085–3090, 2011, doi: 10.1021/nl200993g.

[98] A. Mathur and J. Erlebacher, "Size dependence of effective Young's modulus of nanoporous gold," *Appl. Phys. Lett.*, vol. 90, no. 6, 2007, doi: 10.1063/1.2436718.

[99] J. Weissmüller, R. C. Newman, H. J. Jin, A. M. Hodge, and J. W. Kysar, "Nanoporous metals by alloy corrosion: Formation and mechanical properties," *MRS Bull.*, vol. 34, no. 8, pp. 577–586, 2009, doi: 10.1557/mrs2009.157.

[100] X. Wang, W. Wang, Z. Qi, C. Zhao, H. Ji, and Z. Zhang, "Fabrication, microstructure and electrocatalytic property of novel nanoporous palladium composites," *J. Alloys Compd.*, vol. 508, no. 2, pp. 463–470, 2010, doi: 10.1016/j.jallcom.2010.08.094.

[101] Y. Ding and J. Erlebacher, "Nanoporous metals with controlled multimodal pore size distribution," *J. AM. CHEM. SOC*, vol. 125, pp. 7772–7773, 2003, doi: 10.1021/ja035318g.

[102] Z. Zhonghua, W. Yan, Q. Zhen, L. Jikui, and B. Xiufang, "Nanoporous gold ribbons with bimodal channel size distributions by chemical dealloying of al-au alloys," *J. Phys. Chem. C*, vol. 113, no. 4, pp. 1308–1314, 2009, doi: 10.1021/jp808569g.

[103] G. S. Duffó and J. R. Galvele, "Stress corrosion cracking of Ag-20Au in HClO4, AgClO4, and KCl solutions by surface mobility," *Metall. Trans. A*, vol. 24, no. 2, pp. 425–433, 1993, doi: 10.1007/BF02657330.

[104] Y. Z. Lee, W. Y. Zeng, and I. C. Cheng, "Synthesis and characterization of nanoporous copper thin films by magnetron sputtering and subsequent dealloying," *Thin Solid Films*, vol. 699, no. February, p. 137913, 2020, doi: 10.1016/j.tsf.2020.137913.

[105] Z. Zhang, Y. Wang, Z. Qi, C. Somsen, X. Wang, and C. Zhao, "Fabrication and characterization of nanoporous gold composites through chemical dealloying of two phase Al-Au alloys," vol. 19, pp. 6042–6050, 2009, doi: 10.1039/b904052h.

[106] W. B. Liu, S. C. Zhang, N. Li, J. Zheng, and Y. Xing, "Dealloying behavior of dual-phase Al 40 atom % Cu alloy in an alkaline solution," *J. Electrochem. Soc.*, vol. 158, no. 2, pp. D91–D94, 2011, doi: 10.1149/1.3511771.

[107] Z. Qi and J. Rg Weissmü Ller †, “Hierarchical nested-network nanostructure by dealloying,” vol. 7, no. 7, pp. 5948–5954, 2013, doi: 10.1021/nn4021345.